

Reduced-order modelling of time-periodic flows

Lotz, J.E.

DOI

[10.4233/uuid:42000270-f0d1-4a6b-9be1-560741ca8d6d](https://doi.org/10.4233/uuid:42000270-f0d1-4a6b-9be1-560741ca8d6d)

Publication date

2025

Document Version

Final published version

Citation (APA)

Lotz, J. E. (2025). *Reduced-order modelling of time-periodic flows*. [Dissertation (TU Delft), Delft University of Technology]. <https://doi.org/10.4233/uuid:42000270-f0d1-4a6b-9be1-560741ca8d6d>

Important note

To cite this publication, please use the final published version (if applicable).
Please check the document version above.

Copyright

Other than for strictly personal use, it is not permitted to download, forward or distribute the text or part of it, without the consent of the author(s) and/or copyright holder(s), unless the work is under an open content license such as Creative Commons.

Takedown policy

Please contact us and provide details if you believe this document breaches copyrights.
We will remove access to the work immediately and investigate your claim.



REDUCED-ORDER MODELLING
OF TIME-PERIODIC FLOWS

JACOB EVERT LOTZ

Reduced-order modelling of time-periodic flows

Reduced-order modelling of time-periodic flows

Proefschrift

ter verkrijging van de graad van doctor aan de Technische Universiteit Delft,
op gezag van de Rector Magnificus prof. dr. ir. T.H.J.J. van der Hagen,
voorzitter van het College voor Promoties,
in het openbaar te verdedigen op woensdag 9 april 2025 om 17:30 uur

door

Jacob Evert LOTZ

Master of Science in Maritieme Techniek,
Technische Universiteit Delft, Nederland,

Dit proefschrift is goedgekeurd door de

promotor: Prof. dr. G.D. Weymouth

copromotor: Dr. ir. I. Akkerman

Samenstelling promotiecommissie:

Rector Magnificus,

Prof. dr. G.D. Weymouth,

Dr. ir. I. Akkerman,

voorzitter

Technische Universiteit Delft, Nederland

Technische Universiteit Delft, Nederland

Onafhankelijke leden:

Prof. dr. ir. C. Vuik

Prof. dr. ir. E. H. van Brummelen

Prof. dr. G. Rozza

Prof. dr. S. Elgeti

Dr. D. Korobenko

Prof. dr. ir. B. J. Boersma

Technische Universiteit Delft, Nederland

Technische Universiteit Eindhoven, Nederland

Scuola Internat. Superiore di Studi Avanzati, Italië

Technische Universität Wien, Oostenrijk

University of Calgary, Canada

Technische Universiteit Delft, Nederland, *reservelid*

This publication is part of the project Lift Control for Hydrofoil Craft (with NWO reference number TWM.BL.019.009) of the research program Top Sector Water & Maritime: The Blue Route. The project is funded by:



Keywords: Reduced-order Modelling, Time-periodic Flows, Isogeometric Analysis, Residual-based Variational Multi-scale Turbulence Modelling, Galerkin Proper Orthogonal Decomposition, Weak Boundary Conditions, Hydrofoil, Vertical-axis wind turbine

Printed by: Ridderprint | www.ridderprint.nl

Cover: An artist impression of time-periodic flow by Savanne van Harrewijen

Copyright © 2025 by J.E. Lotz

ISBN 978-94-6384-748-3

An electronic version of this dissertation is available at repository.tudelft.nl

Preface

Dear reader,

This work is not only about the time-periodicity of flows and its reduced-order modeling; it also marks the end of a much larger journey. This journey began on the first of March 2020, which happened to align almost perfectly with the start of the COVID-19 crisis. While the lockdowns had some clear advantages—such as reducing hospitalizations and giving me plenty of time to work on this thesis—they also taught me something important. Meeting interesting and inspiring people, which I was lucky to do much more often after the crisis, is essential for creativity and motivation. I believe that every PhD journey is, in the end, a team effort.

This journey with my team brought many highlights along the way: fixing a major bug in the code, obtaining the first time-periodic results, building a high-accuracy reduced-order model, meeting many wonderful people, and publishing that first paper. Each of these moments felt like a small victory and more than made up for the more challenging times during this journey. I can only hope that these kinds of events are time-periodic and will happen again and again.

I now realize that time-periodicity can be placed in a much broader context. The occurrence of time-periodicity is not limited to flow problems—or even to physics. It can be found in cultural trends (such as the revival of art, music, or fashion), stock market cycles, and likely many other areas. While the work presented here may not directly apply to these topics, it certainly inspires me to think about its potential applications in other contexts.

It feels like more than a coincidence that completing this dissertation aligns perfectly with the release of a new album by one of my favorite bands, Linkin Park [85]. The album is exactly time-periodic and symbolizes that every ending can mark the beginning of something new, which is in the end very similar. But I won't keep you any longer—let's dive into the dissertation!

Jacob Evert Lotz
Delft, Januari 2025

Contents

| | |
|--|-----------|
| Preface | v |
| 1 Introduction | 1 |
| 2 Space-time computations of exactly time-periodic flows past hydrofoils | 9 |
| 2.1 Introduction | 10 |
| 2.2 Periodic space-time formulation of the incompressible flow equations | 12 |
| 2.2.1 Governing equations | 12 |
| 2.2.2 Space-time formulation | 13 |
| 2.2.3 Weak formulation of the continuous space-time problem. | 15 |
| 2.2.4 Weak formulation of the discrete problem | 16 |
| 2.3 Conservation properties | 19 |
| 2.3.1 Conservation of mass | 19 |
| 2.3.2 Conservation of linear momentum | 20 |
| 2.3.3 Conservative traction evaluation | 21 |
| 2.4 Numerical experiments. | 22 |
| 2.4.1 Computational setup | 22 |
| 2.4.2 Mesh-constraint boundary velocity. | 24 |
| 2.4.3 Stationary hydrofoil | 25 |
| 2.4.4 Heaving hydrofoil at a low reduced frequency | 27 |
| 2.4.5 Hydrofoil with large angle pitch motion | 28 |
| 2.5 Conclusions | 33 |
| 3 Projection-based reduced-order modelling of time-periodic problems | 35 |
| 3.1 Introduction | 36 |
| 3.2 Full-order and reduced-order model for the time-periodic incompressible flow | 38 |
| 3.2.1 Strong formulation of time-periodic incompressible flow. | 38 |
| 3.2.2 Discrete weak formulation of time-periodic incompressible flow | 40 |
| 3.2.3 System of nonlinear ordinary differential equations | 42 |
| 3.2.4 Reduced basis using Proper-Orthogonal Decomposition | 44 |
| 3.2.5 Projection-based reduced-order model | 45 |
| 3.3 Numerical experiments. | 47 |
| 3.3.1 Problem setup | 47 |
| 3.3.2 Parameter studies | 52 |
| 3.4 Conclusions | 63 |
| 3.A Temporal and spatial discretization. | 64 |
| 3.B Visualization of the basis | 66 |

| | | |
|----------|--|------------|
| 4 | Considerations on a hyper-reduced model of time-periodic flows | 69 |
| 4.1 | Introduction | 70 |
| 4.2 | Hyper-reduction using empirical interpolation methods | 72 |
| 4.3 | Finite element hyper-reduction with isogeometric solutions | 76 |
| 4.4 | Numerical experiments. | 78 |
| 4.4.1 | Verification using the Navier-Stokes equations for steady flow | 78 |
| 4.4.2 | Towards hyper-reduction for time-periodic problems | 83 |
| 4.5 | Conclusions | 87 |
| 4.A | Numerical parameters | 88 |
| 5 | Study of flow past a vertical-axis wind turbine | 89 |
| 5.1 | Introduction | 90 |
| 5.2 | The reduced-order model of vertical axis wind turbine | 92 |
| 5.2.1 | Model problem | 92 |
| 5.2.2 | The non-inertial frame of reference. | 93 |
| 5.2.3 | Evaluation of the full-order model | 95 |
| 5.2.4 | Model reduction | 96 |
| 5.3 | Validation using the full-order model. | 98 |
| 5.4 | Data collected in the offline stage | 100 |
| 5.5 | Tip-speed ratio study. | 103 |
| 5.6 | Optimisation of tip-speed-ratio for energy production | 107 |
| 5.7 | Conclusions | 108 |
| 6 | Conclusions | 111 |
| 6.1 | Conclusions | 111 |
| 6.2 | Outlook | 113 |
| | Result reproduction | 115 |
| | Curriculum Vitæ | 117 |
| | List of Publications | 119 |
| | Open source contributions | 121 |
| | Acknowledgements | 123 |
| | Summary | 125 |
| | Samenvatting | 127 |
| | Bibliography | 129 |

1

Introduction

Time-periodic flows are omnipresent in both natural and engineered systems. This class of flows is driven by periodic behavior such that flow features repeat at regular intervals. The velocity and pressure fields oscillate in a predictable, cyclic manner, and return to the same state after a fixed period of time, or closely resembles it. Figure 1.1 gives examples of time-periodic flows, such as flow past wind turbines, flow in the heart and arteries, and the flow past a propeller. We are interested in how these flows behave and interact with their environment.

The nature of time-periodic flow inherently leads to long transients. When studying time-periodic flow problems, we first consider the initial state of the flow, at for instance a stand still. From there, the flow develops naturally over time and eventually reaches a time-periodic state. This occurs only after enough time has passed for the influence of the initial flow conditions to become negligible. However, if dealing with turbulence – a chaotic fluid flow characterized by irregular, seemingly random motion – this time-periodic state does not necessarily exist.



Figure 1.1: Examples of time-periodic flow problems. From left to right: flow past a wind turbine, flow in the heart and arteries, and the flow past a ship propeller. Generated using Copilot - Designer.

1 To obtain a meaningful answer from physical experiments or numerical analysis, researchers and engineers phase-average their results over multiple periods requiring even longer transients. These difficulties make time-periodic flow problems challenging to study through either physical experiments or simulations.

We focus on studying time-periodic flows using computational fluid dynamics (CFD). CFD is vital for advancing our understanding and prediction of fluid behavior, as it enables engineers to optimize designs (using e.g. derivatives found with adjoint solutions) and enhance performance before physical testing or prototype development. By numerically solving the governing equations of fluid mechanics, such as the Navier-Stokes equations, CFD offers detailed simulations of fluid interactions across diverse boundary conditions and geometries. This is particularly valuable for analyzing systems where experimental measurements are challenging or impractical.

Many engineering tasks require numerous model evaluations of CFD across a wide range of inputs, like optimization and control [108]. To enable reactive design, in which applications maintain continuous interaction with their environment at the pace of the environment, we need these model evaluations to be fast and preferably real-time [6, 16]. Unfortunately, CFD is associated with high computational costs and extended computation time, not allowing real-time interaction with the program. When dealing with the long transients associated with time-periodic flows, the computational demands increase even further, rendering such simulations impractical for many engineering applications. These computational costs limit the optimisation of designs, results in less efficient control of complex systems and have to be reduced.

The relation between between computational costs and model error is depicted in Figure 1.2. Detailed simulations that solve the Navier-Stokes equations directly (DNS), without the approximation of any turbulence, require extremely fine spatial and temporal resolution, leading to prohibitively high computational costs. This type of simulation can be found in the bottom right corner. It is typically feasible only for small-scale problems and requires some of the world's most powerful supercomputers. Advancements in quantum computing may significantly reduce the time and resources required for these calculations. By harnessing the principles of quantum mechanics, it has the potential to enable a new class of algorithms. These algorithms, at least in theory, can perform the most computationally intensive tasks at exponentially faster speeds compared to traditional methods. However, the time-line and feasibility of applying quantum computing to engineering problems remain uncertain [7, 79, 107].

We can reduce computational requirements by lowering the system's fidelity and modelling a part of the flow using turbulence models. These models are distilled from data but do not use this data directly. We find Large Eddy Simulation (LES) in Figure 1.2, by introducing a model error, left of DNS. LES splits the flow into two scales, the large and the small scales [126]. Only the large-scale turbulent flows are computed while the smaller scales, subgrid-scale turbulence, are modelled. Its computational costs are lower. Introducing other model assumptions with a larger modelling error, we find the Reynolds Averaged Navier-Stokes equations (RANS) with lower computational costs in Figure 1.2. The RANS equations involve decomposing the flow variables into mean and fluctuating components. The mean flow is averaged over time and requires models to close the system of equations [116]. We denote this class of models as high-fidelity models, despite some of these methods having their fidelity reduced.

The success of these methods is highly problem-specific. When selecting an algorithm, it is crucial to consider the nature of the problem and the required answer. No algorithm can achieve optimal performance for every possible problem [144]. A closer examination of Figure 1.2 reveals a dashed line illustrating the cost-error trade-off. Optimization inherently involves a trade-off between minimizing computational costs and model error. Reducing computational costs is only feasible by accepting a model error that aligns with the simulation's objectives.

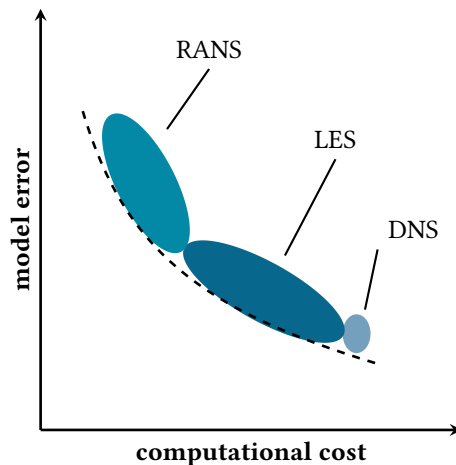


Figure 1.2: Schematic representation of the relation between computational costs and the associated model error for high-fidelity models employing the Reynolds Averaged Navier-Stokes equations (RANS), Large Eddy Simulation (LES) and Direct Numerical Simulation (DNS).

1 These methods share a common limitation: they are not specifically tailored for time-periodic flows and often utilize unnecessarily costly transients. Consequently, they may fail to achieve the optimal performance for time-periodic simulations. We address this issue in the first goal of this thesis:

(i) Develop an efficient and accurate model for analysis of time-periodic flows that effectively handles the costly transients inherent in these flows.

We introduce a high-fidelity model that avoids long transients by enforcing the solution to be time-periodic. We employ a space-time domain in which space and time are treated analogously and apply a periodic boundary condition in time. Space and time are discretized using the same method, and the entire space-time domain is solved at once. Consequently, this eliminates the need for time integration and we only have to solve one period. The solution is exactly periodic and the problem is converted from an initial value problem to a boundary value problem. This assumption is accurate for low Reynolds numbers where the flow is not turbulent. We cannot solve the randomness of turbulence in high Reynolds number flows. Instead, here we find the time-periodic large-scale flow structures, which are of interest for most engineering applications. The new high-fidelity model employs an LES-like model and is introduced in Chapter 2

While this approach mitigates some computational challenges, it is still constrained by the trade-off between cost and error, requiring significant computational resources. To enable faster simulations that users can interact with in real-time, without compromising model accuracy, we must overcome this limitation. We aim to address this challenge specifically for time-periodic flows.

In this thesis, we introduce a computationally economical approach to compute periodic solutions. This involves adding an ingredient to the problem: the integration of data. By incorporating data into the simulation process, we aim to reduce the computational time required to achieve accurate results, making simulations faster and more efficient.

We expand the set of models under consideration to add the new ingredient, data. We differentiate between models based on known physics and those without, as well as between models with and without data. This distinction is illustrated in Figure 1.3. High-fidelity models we considered earlier, such as DNS, LES, and RANS, are in the bottom-right quadrant. They heavily rely on physics and depend minimally on data. Conversely, in the upper quadrants, we find surrogate models. These automated data-driven methods are becoming increasingly important in com-

putational fluid mechanics due to their ability to reduce computational costs. Unlike traditional high-fidelity simulations, surrogate models offer rapid evaluations while maintaining reasonable accuracy.

We distinguish between two different groups of surrogate models: function-fitting models and hybrid models [74]. In the group of function-fitting models, the governing equations of the physical phenomenon are unknown and the goal is to discover them from data. This group consists of purely data-driven models. The hybrid models are not only data-driven, they also have a foundation in known physics. Governing equations or high-fidelity numerical models are available but expensive for the task at hand, and the goal is to use these to learn a computationally efficient surrogate model. From the second group, we discuss two subgroups: physics-informed neural networks and projection-based reduced-order models.

The idea behind the function-fitting group of surrogate models is that with sufficient data any underlying pattern can be uncovered by an observer [80]. With advances in machine learning and data science, we have improved our understanding of extracting these patterns from big data sets that surpass human cognitive capabilities [68, 92]. The produced models are simple, yet still capture the essential dynamics of the system. Also, the employment of neural networks gives the ability to approximate solutions to partial differential equations at a much faster rate than

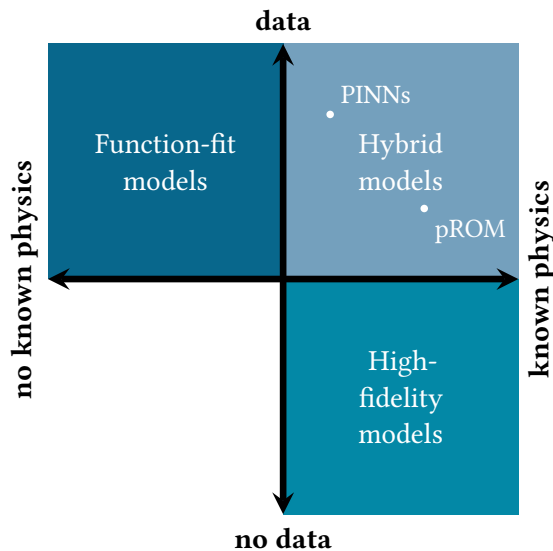


Figure 1.3: Overview of model groups and classification of Physics-Informed Neural Networks (PINNs) and Projection-Based Reduced-Order Models (pROM).

1 traditional numerical methods [36]. The field of purely data-driven models is vast and for an elaborate review, we refer to [18, 112]. While the training of these data-driven models can be computationally expensive, their evaluation phase is typically fast. Additionally, these models have the advantage of being non-intrusive to high-fidelity models [147].

The quality of results from function-fit models can be limited, as they may fail to accurately capture the underlying physics, particularly in the presence of noise in the data [95]. Therefore, our focus shifts to the hybrid models. We explore two promising physics-based surrogate models: projection-based reduced-order models and physics-informed neural networks. For a comprehensive review of other physics-based surrogate models, we refer to [108].

A projection-based reduced-order model (pROM) is a method deeply rooted in the underlying physics. These models are built upon a well-established full-order model. Here, full-order models are high-fidelity models, such as we have described earlier, of which computational costs can be reduced by utilizing pre-existing data from the specific problem under study [15, 48, 111]. More specifically, a pROM approximates the full-order model by projecting it onto a much lower-dimensional space. With this, the pROM inherits the most important features of the full-order model, enabling faster simulations with minimal loss of accuracy. In Figure 1.3, we find it in the bottom-right corner of the hybrid model group.

Physics-informed neural networks (PINNs) represent a special class of machine learning models that embed physical laws directly into the training process [113]. In Figure 1.3, by integrating these embedded physical principles in a data-driven model, we find it in the top-left corner of the hybrid model group in Figure 1.3. PINNs ensure that the resulting solutions not only fit the data but also comply with the known underlying physics. This makes PINNs particularly effective in scenarios where data is scarce or noisy. The approach has demonstrated success in fluid mechanics for easy parameter regimes by outperforming high-fidelity models [20]. However, despite rapid advancements in the field, it fails to correctly predict physics in more challenging problems [32, 75].

Given the deep integration of physics within projection-based reduced-order models and their ability to inherit the features of full-order models, we choose to work with this type of surrogate model. Projection-based reduced-order models have been successfully applied to flow problems in many studies [2, 21, 29, 87, 91, 115, 127, 134]. However, these studies primarily reduce the number of spatial variables and do not address the long transients associated with time-periodic flows. Addi-

tionally, in long time integrations, the solutions provided by reduced-order models may diverge from those of their full-order counterparts [115]. These methods are not specifically tailored for time-periodic flows. With this, we find the second goal of this thesis:

(ii) *Develop a cost-efficient and accurate reduced-order model for the analysis of time-periodic flows.*

We hypothesize that the time-periodic high-fidelity model introduced in the first goal of this thesis is well-suited for model order reduction due to its boundary value nature. Using this full-order model, we aim to develop a reduced-order model and achieve real-time evaluation of time-periodic flows while keeping model error to a minimum.

We use the time-periodic high-fidelity model as our full-order model to develop a projection-based reduced-order model. This process starts with constructing a time-periodic basis using Proper Orthogonal Decomposition (POD). The basis is generated using solutions of the full-order model for the specific problem under study as data. The solution of the full-order model is then restricted by a time-periodic basis. With this, and since we are using a space-time discretization, we get a reduction in the degrees of freedom in both space and time. Subsequently, a Galerkin projection is performed to derive the POD-Galerkin reduced-order model, which directly solves the time-periodic solution and greatly reduces the computational requirements. This procedure is illustrated in Figure 1.4 and discussed in detail in Chapter 3.

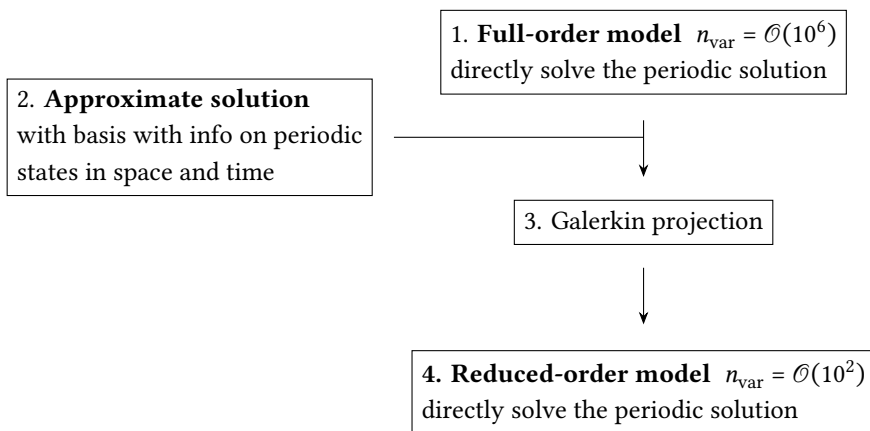


Figure 1.4: Schematic overview of the time-periodic Galerkin-POD reduced-order model

1 The time-periodic reduced-order model inherits the non-linearity of the full-order model using the non-linear Navier-Stokes equations. The linear operator can be pre-computed, but the non-linear operator requires a repeated evaluation in the reduced-order model. The evaluation time of this reduced non-linear operator scales with the size of the full-order model. This induces a major computational bottleneck in evaluating the reduced-order model and does not allow a real-time solution of the model [45]. To investigate the possibilities for real-time flow computations, we explore the application of non-linear reduction techniques in the time-periodic reduced-order model, allowing for much greater speed-ups in Chapter 4.

We use the reduced-order model to study the flow characteristics around a type Darrieus vertical-axis wind turbine at a Reynolds number of 1000. This device, featuring vertically rotating turbine blades, is similar to a Voith Schneider Propeller or a cross-flow water turbine operating under different conditions. Chapter 5 has two primary objectives: first, to demonstrate the applicability of the reduced-order model in industrial problems, and second, to analyze the flow past vertical-axis wind turbines. We showcase how the model can identify the optimal operating point under specific flow conditions. The flow is approximated as two-dimensional to capture the essential dynamics, focusing on the interaction between a single blade and its wake, while excluding the complexities of multiple blade interactions.

In Chapter 6 we conclude and reflect on the goals we have set for this thesis. Here we will also provide an outlook. We have aimed to make the chapters individually readable. However, to avoid redundant information, we will refer to the appropriate chapter for details.

2

Space-time computations of exactly time-periodic flows past hydrofoils

The computation of periodic flows is typically conducted over multiple periods. First, a number of periods is used to develop periodic characteristics, and afterwards statistics are collected from averages over multiple periods. As a consequence, it is uncertain whether the numerical results are exactly time-periodic, and additionally, the time domain might be needlessly long. In this article, we circumvent these concerns by using a time-periodic function space. Consequently, the boundary conditions and solutions are exactly periodic. We employ the isogeometric analysis framework to achieve higher-order smoothness in both space and time. The discretization is performed using residual-based variational multiscale modelling and weak boundary conditions are adopted to enhance the accuracy near the moving boundaries of the computational domain. We enforce the time-periodic boundary condition within the isogeometric discretization spaces, which converts the two-dimensional time-dependent problem into a three-dimensional boundary value problem. Furthermore, we determine the boundary velocities of moving hydrofoils directly from the computational mesh and use a conservation methodology for force extraction. Application of the computational setup to heaving and pitching hydrofoils displays very accurate and exactly periodic results for lift and drag.

This chapter is published as:

[88] **J. E. Lotz**, M. F. P. ten Eikelder, I. Akkerman, “Space–time computations of exactly time-periodic flows past hydrofoils”, *Computers & Fluids* 277, 106286 (2024)

2.1 Introduction

2 Periodic flows are ubiquitous in a large number of industrial applications and natural features. Prototypical examples include the flow around submerged propellers, wind turbines, or rotating flows in turbomachines and engines and the pulsatile flow of blood. Various challenges arise in the design of practical numerical simulations of these flows. On top of the well-known complications centered around the inertia-driven character and the imposition of boundary conditions, the periodic nature adds novel peculiar hurdles. The typical strategy of simulating a periodic flow problem is to perform an unsteady computation in which the flow develops periodic characteristics [67, 73, 96]. As such, the computations are usually not exactly periodic, and the temporal range may be excessively long. Moreover, a user-defined criterion of the characteristics of the flow is inevitable and the flow is never strictly periodic. In this work we exploit the periodic nature of the problem and use a space-time finite element method in the framework of residual-based variational multiscale (VMS) methods, isogeometric analysis and weak boundary conditions. Particular emphasis is on the application to heaving and pitching hydrofoils.

The concept of *space-time finite elements* may be traced back to the late sixties, with contributions by Fried [47] and Oden [104, 105] on the generation of finite element models in the time domain. In time-dependent problems, the standard is to separate the discretization of the time (e.g. finite difference schemes) and space (e.g. Galerkin methods). This is often referred to as the *semi-discrete* method. The idea of space-time finite element methods is to adopt the variational approach in the space-time setting such as in [98], where the space-time formulation is used in conjunction with the Galerkin/Least-squares stabilization. This allowed space-time computations for three-dimensional compressible and incompressible flows [136, 137]. Contributions to accuracy and stability, along with the use of Fourier-analysis, include the stabilized methods in the space-time framework for the advection-diffusion equation and Navier-Stokes equation [62, 93, 125]. This space-time framework was originally formulated for stationary problems and is extended to domains with moving boundaries by Tezduyar and collaborators [138, 139]. Space-time computations of 2D time-periodic flows around fixed, oscillating, and bobbing hydrofoils were extensively covered in [67, 97, 99]. These were the first space-time computations of their kind. A few years later, the *VMS framework* [57, 60], encompassing many existing stabilized methods, was proposed. The framework was originally introduced for stationary problems. In [63] it was argued that the most theoretically coherent framework for the extension to time-dependent problems is the space-time context. The most popular applications of the VMS methodology for time-dependent problems are however in the semi-discrete setting. A notable contribution in this regard is the work [12] that presented a varia-

tionally consistent VMS methodology for turbulent flows called *residual-based variational multiscale* (RBVMS). This method is often used in combination with weak boundary conditions [13]. Recently, the popular Nitsche's method for the imposition of weak boundary conditions has been identified as a variational multiscale formulation [129]. The RBVMS method opened the door for the development of a novel class of small-scale models for large-eddy simulations, including dynamic small-scales [28, 38, 42] and discontinuity capturing [39, 40]. The last important development with implications for the space-time framework that we succinctly discuss, is the introduction of isogeometric analysis [31, 58]. In contrast to classical space-finite element methods, isogeometric analysis offers the possibility of arbitrary smooth finite element basis functions. This technique was initially adopted for spatial discretizations, yet it offers rich opportunities in the space-time setting [76, 100, 106, 121]. On top of the more widely known advantages of isogeometric analysis, as pointed out as early as in 2012 [130, 131, 133], the adoption of it in the space-time context is particularly beneficial for an accurate representation of moving boundaries and a higher continuity in the temporal direction. A good overview of the history and the wide variety of applications of the space-time method can be found in [141], including simulations with isogeometric analysis [132] and a RBVMS discretization [131].

The existing space-time finite element methods form a versatile and fundamental class of methodologies for time-dependent problems in fluid mechanics. The space-time method can be adopted for the computation of periodic flows, for example in [67, 97, 99]. However, just as in the semi-discrete setting, such computations require a transient until a near-periodic state is reached. The numerical results are not strictly periodic. In this article, we circumvent these concerns by performing computations with exact time-periodicity. We compute the periodic state via enforcing the periodicity as a boundary condition in time, see also [53, 123]. This turns the two-dimensional time-dependent model into a three-dimensional boundary value problem. Our numerical results show the exact periodicity without losing the expected accuracy in the solutions. To this purpose we adopt a periodic space-time model of arbitrary continuity via isogeometric analysis. Furthermore, we combine this with the usage of the RBVMS methodology and weak boundary conditions, providing a robust periodic space-time method. We show conservation properties of the proposed method and present a conservative traction evaluation. Last, we introduce mesh constraint boundary velocities. We use our computational setup for the simulation of incompressible flow past a prescribed periodically moving hydrofoil.

The chapter is organized as follows. We describe the time-periodic continuous space-time setup in Section 2.2, which fits within the more general space-time frame-

work. Next, in Section 2.3 we discuss the conservation properties and the continuous force extraction method. In Section 2.4 we provide results of numerical experiments considering the mesh-constraint boundary velocity, force extraction, and periodic flow. The numerical experiments employ two spatial dimensions. We close with concluding remarks in Section 2.5.

2.2 Periodic space-time formulation of the incompressible flow equations

2.2.1 Governing equations

Consider a time-dependent spatial domain $\Omega = \Omega(t) \subset \mathbb{R}^d$ with boundary $\Gamma = \Gamma_{\text{int}} \cup \Gamma_{\text{ext}}$ composed of a time-dependent interior $\Gamma_{\text{int}} = \Gamma_{\text{int}}(t)$ and exterior part Γ_{ext} . The outward unit normal to the boundary Γ is defined as \mathbf{n} . Let us now consider a velocity field \mathbf{u} and introduce the normal velocity $u_n = \mathbf{u} \cdot \mathbf{n}$ with positive part and negative part $u_n^\pm = \frac{1}{2}(u_n \pm |u_n|)$. We partition the exterior boundary into an inflow and outflow part according to the definitions:

$$\Gamma_{\text{ext}}^D := \{\mathbf{x} \in \Gamma \mid u_n(\mathbf{x}) < 0\}, \quad (2.1a)$$

$$\Gamma_{\text{ext}}^N := \{\mathbf{x} \in \Gamma \mid u_n(\mathbf{x}) \geq 0\}. \quad (2.1b)$$

The domain is depicted in Figure 2.1.

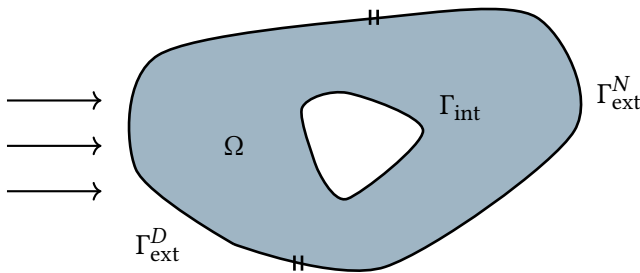


Figure 2.1: Sketch of the spatial domain with its boundaries, with inflow on the left.

We now consider the problem that reads in strong form:

$$\partial_t \mathbf{u} + \mathbf{u} \cdot \nabla \mathbf{u} + \nabla p - \nabla \cdot (2\nu \nabla^s \mathbf{u}) = \mathbf{f} \quad \text{in } \Omega, \quad (2.2a)$$

$$\nabla \cdot \mathbf{u} = 0 \quad \text{in } \Omega, \quad (2.2b)$$

$$\mathbf{u} = \mathbf{g}_{\text{int}} \quad \text{in } \Gamma_{\text{int}}, \quad (2.2c)$$

$$\mathbf{u} = \mathbf{g}_{\text{ext}} \quad \text{in } \Gamma_{\text{ext}}^D, \quad (2.2d)$$

$$-p\mathbf{n} + \nu \nabla \mathbf{u} \cdot \mathbf{n} + u_n^- \mathbf{u} = \mathbf{0} \quad \text{in } \Gamma_{\text{ext}}^N, \quad (2.2e)$$

$$\mathbf{u}(\cdot, 0) = \mathbf{u}_0 \quad \text{in } \Omega. \quad (2.2f)$$

Here the unknown fields are the velocity $\mathbf{u} = \mathbf{u}(\mathbf{x}, t)$ and the pressure $p = p(\mathbf{x}, t)$ with spatial coordinate \mathbf{x} and the time coordinate $t \in \mathcal{I} = (0, T)$ with final time $T > 0$. We employ the standard notation for the gradient (∇), the symmetric gradient (∇^s) and the divergence ($\nabla \cdot$). Furthermore, ν denotes the (constant) kinematic viscosity, $\mathbf{f} = \mathbf{f}(t)$ is a (time-dependent) external force, and $\mathbf{g}_{\text{int}} = \mathbf{g}_{\text{int}}(t)$ and \mathbf{g}_{ext} are prescribed (time-dependent) velocities on the interior boundary and inflow partition of the exterior boundary, respectively. We split the prescribed no-slip velocity into a normal (\mathbf{g}_n) and tangential component (\mathbf{g}_t):

$$\mathbf{g}_{\text{int}} = \mathbf{g}_n + \mathbf{g}_t, \quad (2.3a)$$

$$\mathbf{g}_n = (\mathbf{g}_{\text{int}} \cdot \mathbf{n})\mathbf{n}, \quad (2.3b)$$

$$\mathbf{g}_t \cdot \mathbf{n} = 0. \quad (2.3c)$$

Denoting the normal velocity of the domain boundary Γ_{int} by $v_n = \mathbf{g}_n \cdot \mathbf{n}$, the normal component \mathbf{g}_n is prescribed by the relation $\mathbf{g}_n = v_n \mathbf{n}$.

The equations (2.2) describe the incompressible Navier-Stokes equations, with the balance of linear momentum and the continuity equation in (2.2a) and (2.2b), the Dirichlet boundary conditions on the interior and the inflow boundary in (2.2c) and (2.2d), the outflow boundary condition in (2.2e) and the initial condition in (2.2f).

2.2.2 Space-time formulation

We introduce the (continuous) space-time domain $Q = \Omega \times \mathcal{I}$ as an extrusion of the spatial domain $\Omega = \Omega(t)$. The boundary of Q consists of an interior part $P_{\text{int}} = P_{\text{int}}(t) = \Gamma_{\text{int}}(t) \times \mathcal{I}$, and an exterior part made up of an inflow $P_{\text{ext}}^D = \Gamma_{\text{ext}}^D \times \mathcal{I}$ and an outflow $P_{\text{ext}}^N = \Gamma_{\text{ext}}^N \times \mathcal{I}$ contribution. We visualize the setup in Figure 2.2.

We introduce the space-time coordinate $\hat{\mathbf{x}} = [\mathbf{x}^T \ s]^T = [x_1 \ \dots \ x_d \ s x_{d+1}]$ and the extended velocity vector $\hat{\mathbf{u}} = [\mathbf{u}^T \ s]^T$, where s is a velocity relating the time and space dimensions. For simplicity, s can be chosen as 1.

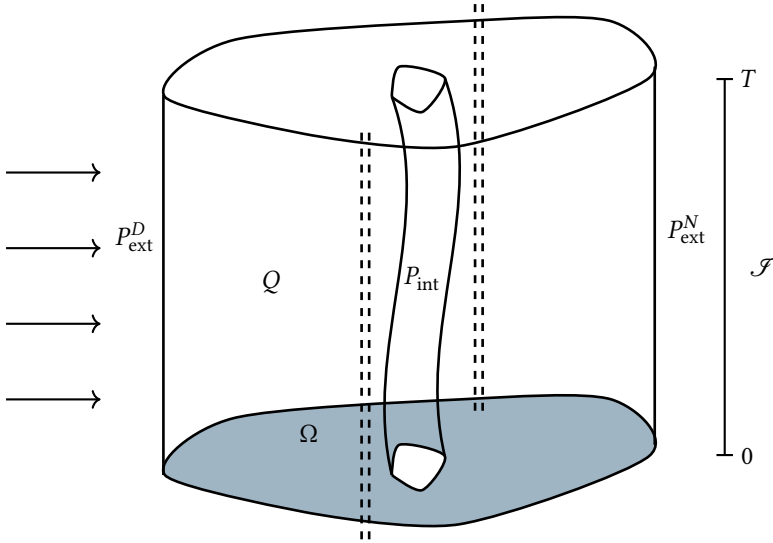


Figure 2.2: Sketch of the space-time domain Q with its boundaries P , with inflow on the left, as an extrusion of the spatial domain Ω in gray.

In this work we focus on periodic flows and as such, we consider a periodically changing domain Ω with period \mathcal{T} :

$$\Omega|_t = \Omega|_{t+\mathcal{T}}. \quad (2.4)$$

Additionally, we require the prescribed external force \mathbf{f} and boundary velocities to be periodic:

$$\mathbf{f}(\mathbf{x}, t) = \mathbf{f}(\mathbf{x}, t + \mathcal{T}), \quad (2.5a)$$

$$\mathbf{g}(\mathbf{x}, t) = \mathbf{g}(\mathbf{x}, t + \mathcal{T}). \quad (2.5b)$$

The initial condition in (2.2f) is represented in the space-time setting by the time-periodic condition:

$$\mathbf{u}(\cdot, 0) = \mathbf{u}(\cdot, \mathcal{T}) \quad \text{in } \Omega. \quad (2.6)$$

We take the final time as $T = \mathcal{T}$ to cover one period.

Using these definitions, problem (2.2) transforms in the space-time context into the steady state problem:

$$\hat{\mathbf{u}} \cdot \nabla_{\hat{\mathbf{x}}} \mathbf{u} + \nabla p - \nu \nabla^2 \mathbf{u} = \mathbf{f} \quad \text{in } Q, \quad (2.7a)$$

$$\nabla \cdot \mathbf{u} = 0 \quad \text{in } Q, \quad (2.7b)$$

$$\mathbf{u} = \mathbf{g}_{\text{int}} \quad \text{in } P_{\text{int}}, \quad (2.7c)$$

$$\mathbf{u} = \mathbf{g}_{\text{ext}} \quad \text{in } P_{\text{ext}}^D, \quad (2.7d)$$

$$-p \mathbf{n} + \nu \nabla \mathbf{u} \cdot \mathbf{n} + u_n^- \mathbf{u} = \mathbf{0} \quad \text{in } P_{\text{ext}}^N, \quad (2.7e)$$

$$\mathbf{u}(\cdot, 0) = \mathbf{u}(\cdot, T) \quad \text{in } \Omega. \quad (2.7f)$$

In (2.7a) we have combined the first two members of (2.2a) into a single term via the identity:

$$\partial_t \mathbf{u} + \mathbf{u} \cdot \nabla \mathbf{u} = \hat{\mathbf{u}} \cdot \nabla_{\hat{\mathbf{x}}} \mathbf{u}, \quad (2.8)$$

where $\nabla_{\hat{\mathbf{x}}}$ is the space-time gradient. The normal \mathbf{n} in Equation (2.7e) is the classical spatial normal and can be extracted from the space-time normal $\hat{\mathbf{n}} = [n_1 \dots n_d n_{d+1}]^T$ via,

$$\mathbf{n} = \frac{1}{\sqrt{n_1^2 + \dots + n_d^2}} \begin{bmatrix} n_1 \\ \vdots \\ n_d \end{bmatrix}. \quad (2.9)$$

The space-time outward normal $\hat{\mathbf{n}}$ has unit length in the norm $\|\cdot\|_{G_s}$ defined by

$$\|\hat{\mathbf{n}}\|_{G_s}^2 = \hat{\mathbf{n}} \cdot \mathbf{G}_s \hat{\mathbf{n}}, \quad (2.10)$$

where \mathbf{G}_s is the space-time metric

$$\mathbf{G}_s = \begin{pmatrix} \mathbf{I}_{d \times d} & 0_{1 \times d} \\ 0_{d \times 1} & s^2 \end{pmatrix}. \quad (2.11)$$

Furthermore, the normal velocity v_n is related to the space-time velocity s and the space-time normal $\hat{\mathbf{n}}$ via:

$$v_n = -s \frac{n_{d+1}}{\sqrt{n_1^2 + \dots + n_d^2}}. \quad (2.12)$$

2.2.3 Weak formulation of the continuous space-time problem

The weak formulation of the continuous space-time problem is stated using the trial and test function spaces \mathscr{W}_g and \mathscr{W}_0 respectively. Members of the trial function space \mathscr{W}_g satisfy the non-homogeneous Dirichlet boundary conditions for the velocity on P_{ext}^D whereas elements in the test function space \mathscr{W}_0 satisfy the homogeneous

Dirichlet boundary conditions on P_{ext}^D . Additionally, members of both spaces satisfy the periodic boundary condition $\mathbf{u}|_{\Omega_0} = \mathbf{u}|_{\Omega_T}$ where, $\Omega_0 = Q|_{t=0}$ and $\Omega_T = Q|_{t=T}$. To enforce the Dirichlet boundary conditions on P_{int} we introduce the subspaces $\mathcal{V}_g \subset \mathcal{W}_g$ and $\mathcal{V}_0 \subset \mathcal{W}_0$, that additionally satisfy non-homogeneous and homogeneous boundary conditions on P_{int} , respectively.

The variational formulation of Equation (2.7) now reads as:

find $U = \{\mathbf{u}, p\} \in \mathcal{V}_g$ such that for all $W = \{\mathbf{w}, q\} \in \mathcal{V}_0$:

$$B_{\text{GAL}}(U, W) = L(W), \quad (2.13a)$$

where

$$\begin{aligned} B_{\text{GAL}}(U, W) = & (\mathbf{w}, \hat{\mathbf{u}} \cdot \nabla_{\hat{\mathbf{x}}} \mathbf{u})_Q - (\nabla \cdot \mathbf{w}, p)_Q \\ & + (\nabla \mathbf{w}, \nu \nabla \mathbf{u})_Q + (q, \nabla \cdot \mathbf{u})_Q - (\mathbf{w}, u_{\text{n}}^- \mathbf{u})_{P_{\text{ext}}^N}, \end{aligned} \quad (2.13b)$$

$$L(W) = (\mathbf{w}, \mathbf{f})_Q. \quad (2.13c)$$

The L^2 inner product over D is defined as $(\cdot, \cdot)_D$.

2.2.4 Weak formulation of the discrete problem

To introduce the numerical discretization, we first subdivide our physical domain Q into elements Q_K . The domain of element interiors denotes:

$$\tilde{Q} = \bigcup_K Q_K. \quad (2.14)$$

We apply residual-based variational multiscale turbulence modeling [11, 12] in which the weighting function space and trial solution space are decomposed into subspaces that contain the coarse and fine scales:

$$\mathcal{W}_g = \mathcal{W}_g^h \oplus \mathcal{W}', \quad (2.15a)$$

$$\mathcal{W}_0 = \mathcal{W}_0^h \oplus \mathcal{W}', \quad (2.15b)$$

where \mathcal{W}_g^h and \mathcal{W}_0^h are coarse-scale spaces, and $\mathcal{W}' \subset \mathcal{W}_g \cup \mathcal{W}_0$ are the fine scales. The coarse-scale space is spanned by the finite-dimensional numerical discretization whereas the fine-scales are their infinite-dimensional complement. Uniqueness of

the multi-scale split (2.15) is ensured when the split is established via a projection operator. (2.15) implies that the members of \mathcal{W}_g and \mathcal{W}_0 split as:

$$\{\mathbf{u}, p\} = \{\mathbf{u}^h, p^h\} + \{\mathbf{u}', p'\}, \quad (2.16a)$$

$$\{\mathbf{w}, q\} = \{\mathbf{w}^h, q^h\} + \{\mathbf{w}', q'\}, \quad (2.16b)$$

where the components of the coarse-scale subspaces are denoted as $\mathbf{U}^h = \{\mathbf{u}^h, p^h\} \in \mathcal{W}_g^h$ and $\mathbf{W}^h = \{\mathbf{w}^h, q^h\} \in \mathcal{W}_0^h$, and the components of the small-scale subspace are denoted as $\mathbf{U}' = \{\mathbf{u}', p'\} \in \mathcal{W}'$ and $\mathbf{W}' = \{\mathbf{w}', q'\} \in \mathcal{W}'$.

To arrive at the fully-discrete formulation we make the following modeling choices. First, we apply a pseudo-transient continuation to march in pseudo-time to the space-time steady state solution. Next, we select a standard H_0^1 -multiscale projector that eliminates the fine-scale viscosity contribution. Next, we replace the small-scale space \mathcal{W}' with the velocity-pressure product $\mathcal{V}' \times \mathcal{P}'$. The fine-scales are modeled as:

$$\mathbf{u}' = -\tau_M \mathbf{r}_M, \quad (2.17a)$$

$$p' = -\tau_C r_C, \quad (2.17b)$$

with the strong residuals

$$\mathbf{r}_M = (\hat{\mathbf{u}}^h \cdot \nabla_{\hat{\mathbf{x}}}) \mathbf{u}^h - \nabla p - \nu \nabla^2 \mathbf{u}^h - \mathbf{f}, \quad (2.18a)$$

$$r_C = \nabla \cdot \mathbf{u}^h, \quad (2.18b)$$

and stability parameters

$$\tau_M = (\hat{\mathbf{u}}^h \cdot \hat{\mathbf{G}} \hat{\mathbf{u}}^h + C^I \nu^2 \mathbf{G} : \mathbf{G})^{-1/2}, \quad (2.19a)$$

$$\tau_C = \tau_M^{-1} \text{Tr}(\mathbf{G})^{-1}. \quad (2.19b)$$

In both the momentum residual and its corresponding stability parameter the time derivative is incorporated in the convection term, analogous to (2.8). As a consequence, the convective and diffusive contributions depend on two different metric tensors, the space-time metric tensor $\hat{\mathbf{G}}$ and spatial metric tensor \mathbf{G} , respectively. These metric tensors are given by

$$\hat{\mathbf{G}} = \left(\frac{\partial \xi}{\partial \hat{\mathbf{x}}} \right)^T \mathbf{G}_s \frac{\partial \xi}{\partial \hat{\mathbf{x}}}, \quad \mathbf{G} = \left(\frac{\partial \xi}{\partial \mathbf{x}} \right)^T \frac{\partial \xi}{\partial \mathbf{x}}. \quad (2.20)$$

Lastly, we enforce the Dirichlet boundary conditions weakly [13]. To this purpose we introduce the penalty parameter

$$\tau_b = \frac{1}{2} C_b^I \nu (\mathbf{n} \cdot \mathbf{G} \mathbf{n})^{\frac{1}{2}}. \quad (2.21)$$

We now define the fully-discrete time-periodic formulation. The formulation fits within the well-known space-time framework. In particular, as a consequence of the continuous spaces, the jump term across the space-time slabs that is common in the space-time method is absent. The method reads as:

find $\mathbf{U}^h = \{\mathbf{u}^h, p^h\} \in \mathcal{W}_g^h$ such that for all $\mathbf{W} = \{\mathbf{w}^h, q^h\} \in \mathcal{W}_0^h$:

$$B(\mathbf{U}^h, \mathbf{W}^h) = L(\mathbf{W}^h), \quad (2.22a)$$

where

$$\begin{aligned} B(\mathbf{U}^h, \mathbf{W}^h) &= B_{\text{GAL}}(\mathbf{U}^h, \mathbf{W}^h) + B_{\text{PT}}(\mathbf{U}^h, \mathbf{W}^h) \\ &\quad + B_{\text{STAB}}(\mathbf{U}^h, \mathbf{W}^h) + B_{\text{WBC}}(\mathbf{U}^h, \mathbf{W}^h), \end{aligned} \quad (2.22b)$$

$$B_{\text{PT}}(\mathbf{U}^h, \mathbf{W}^h) = (\mathbf{w}^h, \partial_\theta \mathbf{u}^h)_{\tilde{Q}} + \frac{1}{a^2} (q^h, \partial_\theta p^h)_{\tilde{Q}}, \quad (2.22c)$$

$$\begin{aligned} B_{\text{STAB}}(\mathbf{U}^h, \mathbf{W}^h) &= -(\nabla_{\mathbf{x}} \mathbf{w}^h, \mathbf{u}' \otimes \hat{\mathbf{u}}^h)_{\tilde{Q}} - (\nabla \mathbf{w}^h, \mathbf{u}^h \otimes \mathbf{u}')_{\tilde{Q}} \\ &\quad - (\nabla \mathbf{w}^h, \mathbf{u}' \otimes \mathbf{u}')_{\tilde{Q}} - (\nabla q^h, \mathbf{u}')_{\tilde{Q}} - (\nabla \cdot \mathbf{w}^h, p')_{\tilde{Q}}, \end{aligned} \quad (2.22d)$$

$$\begin{aligned} B_{\text{WBC}}(\mathbf{U}^h, \mathbf{W}^h) &= (\mathbf{w}^h, p^h \mathbf{n} - \nu \nabla \mathbf{u}^h \cdot \mathbf{n})_{P_{\text{int}}} + (\nu \nabla \mathbf{w}^h \cdot \mathbf{n} - q^h \mathbf{n}, \mathbf{u}^h - \mathbf{g})_{P_{\text{int}}} \\ &\quad + (\mathbf{w}^h \tau_b, \mathbf{u}^h - \mathbf{g})_{P_{\text{int}}}. \end{aligned} \quad (2.22e)$$

Equation (2.22c) represents the pseudo-transient continuation as a globalization technique [30, 70]. The pseudo-transient continuation technique is a widely applied methodology that obtains the steady state solution by adding a derivative to pseudo-time θ . The first term is classical, whereas the utilization of the second term is non-standard. This term introduces artificial compressibility [26, 27, 135], where a is an artificial speed of sound. This term overcomes some of the difficulties due to the saddle-point nature of the underlying problem (i.e. the absence of a pressure term in the continuity equation). Moreover, we note the introduction of this term permits more powerful preconditioning options such as algebraic multigrid (AMG). We remark that the numerical solution of the problem is fully incompressible and thus does not depend on the artificial speed of sound a .

Equation (2.22d) describes terms associated with variational multiscale stabilisation [12]. In LES terminology the first two terms represent the cross-stress, while

the third term represents the Reynolds stress. In the context of stabilized methods, the first term is the Streamline-upwind Petrov-Galerkin (SUPG) term [17], and the fourth and last terms are the Pressure-Stabilizing/Petrov-Galerkin (PSPG) [140] and Least-Squares on Incompressibility Constraint (LSIC) terms respectively. Note that the first and the second terms are not each other transposes. Namely, we incorporate the temporal derivative of the fine-scales in the SUPG term:

$$(\mathbf{w}, \partial_t \mathbf{u}')_{\tilde{Q}} + (\nabla \mathbf{w}^h, \mathbf{u}' \otimes \mathbf{u}^h)_{\tilde{Q}} = (\nabla_{\hat{\mathbf{x}}} \mathbf{w}^h, \mathbf{u}' \otimes \hat{\mathbf{u}}^h)_{\tilde{Q}}. \quad (2.23)$$

This relation is a direct consequence of the partial integration (in the temporal direction) of the fine-scale time-derivative term:

$$(\mathbf{w}, \partial_t \mathbf{u}')_{\tilde{Q}} = -(\partial_t \mathbf{w}, \mathbf{u}')_{\tilde{Q}}, \quad (2.24)$$

where we note the absence of boundary contributions due to the periodic boundary conditions.

Lastly, equation Equation (2.22e) enforces the weak boundary conditions on the interior boundary (2.7c). The first term is the consistency term. This term originates from integration by parts and as such guarantees variational consistency. The second term is the so-called the dual consistency term, and the last term is the penalty term that ensures the stability of the formulation. We recall that the Dirichlet boundary conditions in (2.7d) on P_{ext}^D are enforced strongly.

2.3 Conservation properties

In this section we establish the conservation properties of the discrete method. We show conservation of mass, conservation of linear momentum and provide an approach to conservatively evaluate the traction. We consider a converged solution where $\partial_\theta \mathbf{u}^h = \partial_\theta p^h = 0$.

2.3.1 Conservation of mass

The global conservation of mass directly follows by selecting the weighting function $\mathbf{W}^h = \{\mathbf{0}, 1\}$ in the discrete weak formulation (2.22):

$$\int_Q \nabla \cdot \mathbf{u}^h \, dx = 0. \quad (2.25)$$

We do not attain conservation of mass per time-slab since the weighting function with pressure component that equals 1 on a single time-slab and 0 on the others is not a member of \mathcal{W}_0^h . Remark that it is possible to work with a particular selection

of isogeometric velocity-pressure spaces that establishes pointwise satisfaction of the incompressibility constraint [38, 41].

2.3.2 Conservation of linear momentum

In order to study the conservation of linear momentum one might wish to substitute the weighting function $\mathbf{W}^h = \{\mathbf{w}^h, q^h\} = \{\mathbf{e}_i, 0\}$ with $\mathbf{e}_i \in \mathbb{R}^d$ the i -th Cartesian unit vector into the discrete weak formulation (2.22). This choice is not permitted: $\{\mathbf{e}_i, 0\} \notin \mathcal{W}_0^h$. One possible remedy is to work with unconstrained function spaces and weakly enforce the non-homogeneous boundary condition via a Lagrange multiplier construct [37, 38]. The Lagrange multiplier is also called *auxiliary flux* [59] and is used to show global and local conservation. The method yields conservative boundary fluxes which is a major advantage as compared to utilizing direct procedures that provide non-conservative boundary fluxes.

We denote the vector-valued Lagrange multiplier/auxiliary flux as λ . Recall that the discrete weak formulation (2.22) is defined for the test function space \mathcal{W}_0^h in which the velocity test functions vanish on P_{ext}^D . In order to present the augmented formulation, we require the introduction of other test function spaces. Denote the set of all velocity basis functions η and, furthermore, denote with η_g the set of velocity basis functions that do not vanish on P_{ext}^D . With the notation $\mathcal{W}_0^h = \mathcal{U}_0^h \times \mathcal{P}^h$ of the velocity and pressure components of the test function space, we have $\mathcal{U}_0^h = \text{span}\{N_A\}_{A \in \eta - \eta_g}$, where $N_A = N_A(x)$ are the velocity basis functions. Furthermore, we introduce the unrestricted velocity space $\mathcal{U}^h = \text{span}\{N_A\}_{A \in \eta}$ and unrestricted velocity-pressure space $\mathcal{W}^h = \mathcal{U}^h \times \mathcal{P}^h$. The augmented problem now reads:

find $U^h \in \mathcal{W}_g^h$ such that for all $\bar{\mathbf{W}}^h = \{\bar{\mathbf{w}}^h, q^h\} \in \mathcal{W}^h$:

$$(\lambda^h, \bar{\mathbf{w}}^h)_{P_{\text{ext}}^D} = B(U^h, \bar{\mathbf{W}}^h) - L(\bar{\mathbf{W}}^h). \quad (2.26)$$

This problem splits as:

find $U^h \in \mathcal{W}_g^h$ and $\lambda^h \in \mathcal{W}^h - \mathcal{W}_0^h$ such that

$$0 = B(U^h, \mathbf{W}^h) - L(\mathbf{W}^h) \quad \text{for all } \mathbf{W}^h \in \mathcal{W}_0^h \quad (2.27a)$$

$$(\lambda^h, \bar{\mathbf{w}}^h)_{P_{\text{ext}}^D} = B(U^h, \bar{\mathbf{W}}^h) - L(\bar{\mathbf{W}}^h) \quad \text{for all } \bar{\mathbf{W}}^h \in \mathcal{W}^h - \mathcal{W}_0^h. \quad (2.27b)$$

The first subproblem coincides with our original weak formulation and thus com-

pletely determines the numerical solution $\mathbf{U}^h \in \mathcal{W}_g^h$. This solution may be directly substituted into the second subproblem to evaluate the discrete auxiliary flux $\lambda^h \in \mathcal{W}^h - \mathcal{W}_0^h$.

We are now in the position to evaluate the linear momentum conservation and select $\bar{\mathbf{W}}^h = \{\mathbf{e}_i, 0\}$ in (2.26):

$$\begin{aligned} \int_{P_{\text{ext}}^D} \lambda_i^h \, ds &= \int_{P_{\text{int}}} p^h n_i - v(u_{i,j} + u_{j,i}) n_j \, ds - \int_Q f_i \, dx \, ds \\ &\quad - \int_{P_{\text{ext}}^N} u_n^- u_i^h \, ds + \int_{P_{\text{int}}} \tau_b(u_i^h - g_i) \, ds. \end{aligned} \quad (2.28)$$

This shows that λ_i^h represents the total conserved boundary flux on P_{ext}^D . Remark that the last two members on the right-hand side result from the usage of weak boundary conditions on P_{int} and are thus absent when instead imposing these conditions strongly.

2.3.3 Conservative traction evaluation

With the aim of evaluating the time-dependent traction on the interior boundary Γ_{int} we select $\bar{\mathbf{W}}^h = \{\mathbf{e}_i N_a, 0\}$ in (2.26) with $N_a = N_a(t)$ an arbitrary basis function in the temporal direction. Note that this choice is permitted due to the tensor structure of the NURBS computational mesh. Substitution provides:

$$\begin{aligned} \int_{P_{\text{ext}}^D} \lambda_i^h N_a \, ds + \int_Q f_i N_a \, dx + \int_{P_{\text{ext}}^N} u_n^- u_i^h \, ds &= \int_{P_{\text{int}}} p^h n_i N_a - v(u_{i,j} + u_{j,i}) n_j N_a \, ds \\ &\quad + \int_{P_{\text{int}}} \tau_b(u_i^h - g_i) N_a \, ds. \end{aligned} \quad (2.29)$$

The right-hand side of (2.29) contains all the integrals on the interior boundary P_{int} . In order to evaluate the (vector-valued) traction force ψ we introduce the discrete problems for $i = 1, \dots, d$:

find $\psi_i^h \in \text{span}\{N_b\}_{b \in \xi}$ such that

$$\begin{aligned} \int_{P_{\text{int}}} \psi_i^h N_a \, ds &= \int_{P_{\text{int}}} p^h n_i N_a - v(u_{i,j} + u_{j,i}) n_j N_a \, ds \\ &\quad + \int_{P_{\text{int}}} \tau_b(u_i^h - g_i) N_a \, ds \end{aligned} \quad (2.30)$$

where ξ is the set of basis function numbers in the time direction. The traction forces ψ_i^h thus result from inverting a mass matrix (per direction).

2.4 Numerical experiments

In this section, we discuss the computational setup and subsequently provide results of four numerical experiments using the formulation in Section 2.2.4. We evaluate the forces in the space-time domain using the conservative traction evaluation of Section 2.3.3. First, we compare the results of the mesh-constraint boundary velocity of a sinusoidal heaving hydrofoil with the analytical solution and study its dependency on the temporal discretization. Second, in order to examine the capability of the proposed methodology of predicting steady flow, we study the results of fluid flow past a stationary hydrofoil. We perform a grid convergence study and compare our results with the literature. Third, we focus on the hydrodynamics of a moving body, which is much more complex than the case of a steady body. We simulate the flow past a low-frequency heaving hydrofoil. Lastly, we investigate the predictive capability of the methodology on capturing history effects in the wake. We simulate the flow past a pitching hydrofoil at a moderate frequency. Experimental data considering (unsteady) forces on a hydrofoil in a low Reynolds-number flow is not available in the literature. We support our predictions with numerical results from the literature and steady state simulations using the steady variant of the flow model (2.22). All results presented here correspond to simulations using two spatial dimensions. The third direction refers to time.

2.4.1 Computational setup

We introduce the space-time domain Q as an extrusion of the spatial domain Ω enclosing a symmetric four-digit NACA foil section [1]. The spatial domain is discretized as a C-shaped mesh using six NURBS patches employing second-order NURBS. NURBS are utilized instead of B-splines to more accurately represent the circular outer boundary of the domain. The spatial domain is illustrated in Figure 2.3. The discretization is C^1 -continuous inside the patches and C^0 -continuous across patches. The hydrofoil and its motion are incorporated into the space-time mesh using curve interpolation.

Figure 2.4 provides an overview and a close-up of a temporal slice of the mesh. The mesh is constructed with the aim of achieving high quality near the hydrofoil. Based on simulations of the flow past a cylinder [14], we choose the distance between Γ_{int} and Γ_{ext} to be 8 chord lengths in order to preclude influence from the outflow boundary Γ_{ext} . We have numerically verified that influence of Γ_{ext} is virtually absent. We select the chord c and free stream velocity U as $c = U = 1$. The numerical experiments are conducted in Delfi, which is based on the MFEM library [3].

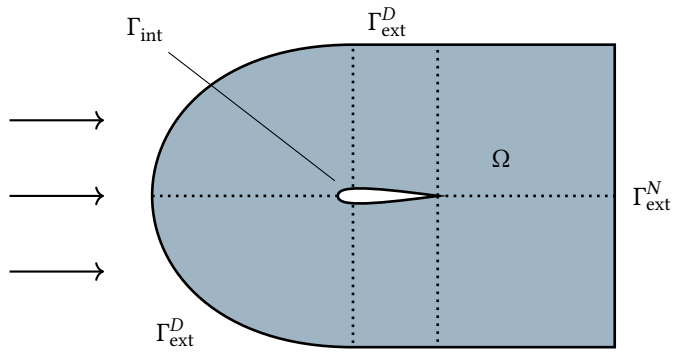


Figure 2.3: Schematic representation of the domain Ω , as a time slice of P , surrounding the hydrofoil with the no-slip boundary Γ_{int} , the inflow boundary Γ_{ext}^D and the outflow boundary Γ_{ext}^N . The arrows indicate the direction of the flow. The six NURBS patches are indicated with a dotted line.

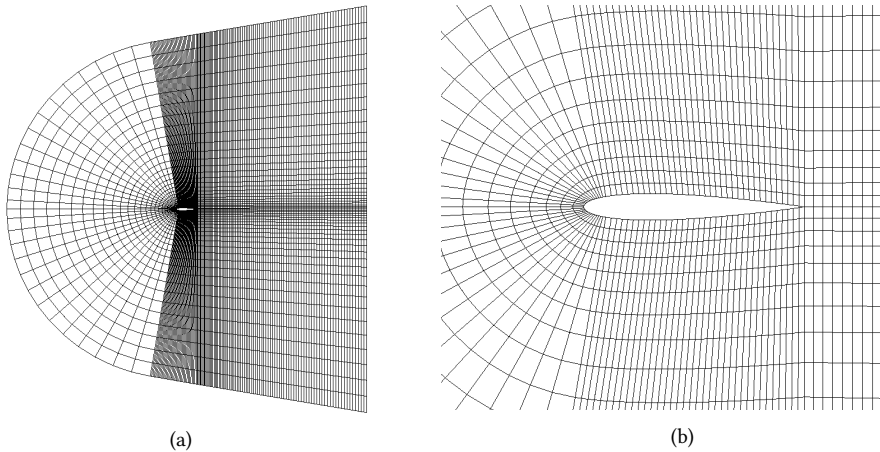


Figure 2.4: The spatial mesh as a slice in time: a) The full C-shaped spatial mesh; b) A close-up of the spatial mesh near the interpolated hydrofoil.

The time-marching in pseudo-time θ towards a steady solution typically consists of 14 pseudo-time steps of 5 seconds using the backward Euler method as a pseudo-time marching scheme. As a stopping criterion, we terminate the computation when the L^2 -norm of the residual of the momentum and mass equations is smaller than 10^{-6} at the start of the first Newton iteration. Per time step we use 5 Newton iterations. We choose the artificial speed of sound a as 4, which exceeds the velocities encountered in the simulations. This provides a significant reduction in simulation time. Furthermore, we select the inverse estimate coefficients as $C^I = 36$ and $C_b^I = 8$. We note that the latter is only suitable for polynomial degrees up to 2.

Lastly, we discuss the computation of the boundary velocity on the interior boundary \mathbf{g}_{int} . We recall the split:

$$\mathbf{g}_{\text{int}} = \mathbf{g}_n + \mathbf{g}_t, \quad (2.31a)$$

$$\mathbf{g}_n = (\mathbf{g}_{\text{int}} \cdot \mathbf{n})\mathbf{n} = v_n \mathbf{n}, \quad (2.31b)$$

$$\mathbf{g}_t \cdot \mathbf{n} = 0, \quad (2.31c)$$

where v_n satisfies the relation Equation (2.12). The domain motion fully prescribes \mathbf{g}_n , while the tangential component \mathbf{g}_t is still undetermined. To numerically determine \mathbf{g}_{int} however, we use the motion encoded in the mesh and do not rely on the relation Equation (2.12). The following procedure is permitted due to the extrusion structure of the space-time mesh. We have the following relations:

$$t = t(\xi_{d+1}), \quad (2.32a)$$

$$\mathbf{X} = \mathbf{X}(\xi_1, \dots, \xi_d), \quad (2.32b)$$

where \mathbf{X} is a Lagrangian coordinate labeling a particle, and where ξ are the coordinates in the reference domain. We compute the boundary velocity by taking the derivative of the spatial coordinate \mathbf{x} to the time direction $t = x_{d+1}$ on a particle path:

$$\mathbf{g}_{\text{int}} = \left. \frac{\partial \mathbf{x}}{\partial t} \right|_{\mathbf{X}} \quad \text{in } P_{\text{int}}. \quad (2.33)$$

Realizing the dependence $\mathbf{x} = \mathbf{x}(\xi_1, \dots, \xi_{d+1})$, we can use the chain rule to conclude:

$$\mathbf{g}_{\text{int}} = s \left. \frac{\partial \mathbf{x}}{\partial x_{d+1}} \right|_{\mathbf{X}} = s \sum_{i=1}^{d+1} \left. \frac{\partial \mathbf{x}}{\partial \xi_i} \frac{\partial \xi_i}{\partial x_{d+1}} \right|_{\mathbf{X}} = s \left. \frac{\partial \mathbf{x}}{\partial \xi_{d+1}} \frac{\partial \xi_{d+1}}{\partial x_{d+1}} \right|_{\mathbf{X}} \quad \text{in } P_{\text{int}}. \quad (2.34)$$

We note that the velocity \mathbf{g}_{int} computed via Equation (2.34) satisfies $\mathbf{g}_{\text{int}} \cdot \mathbf{n} = v_n$, where v_n is given by Equation (2.12).

2.4.2 Mesh-constraint boundary velocity

We evaluate the mesh motion and the resulting mesh-constraint boundary velocity \mathbf{g}_{int} . We apply a heave motion to the hydrofoil such that it only moves in the x_2 -direction. The heave motion of the hydrofoil is sinusoidal with $h(t) = h_a \sin(2\pi t/T)$, with the amplitude $h_a = 0.5 \text{ m}$ and the period $T = 8 \text{ s}$. We use three different temporal resolutions consisting of 6, 12 and 24 elements in the temporal direction n_{el,x_3} .

Figure 2.5a presents the resulting mesh motion with the corresponding analytical solution. The second-order NURBS are reconstructed using the control points from the mesh. We observe that the finest mesh with $n_{\text{el},x_3} = 24$ is virtually indistinguishable from the analytical solution. Next, we visualize the resulting vertical boundary velocity g_{x_2} and the corresponding analytical solution in Figure 2.5b. The velocities are linear within the element due to the C^1 mesh continuity. Again, the results on the finest mesh with $n_{\text{el},x_3} = 24$ are virtually indistinguishable from the analytical solution.

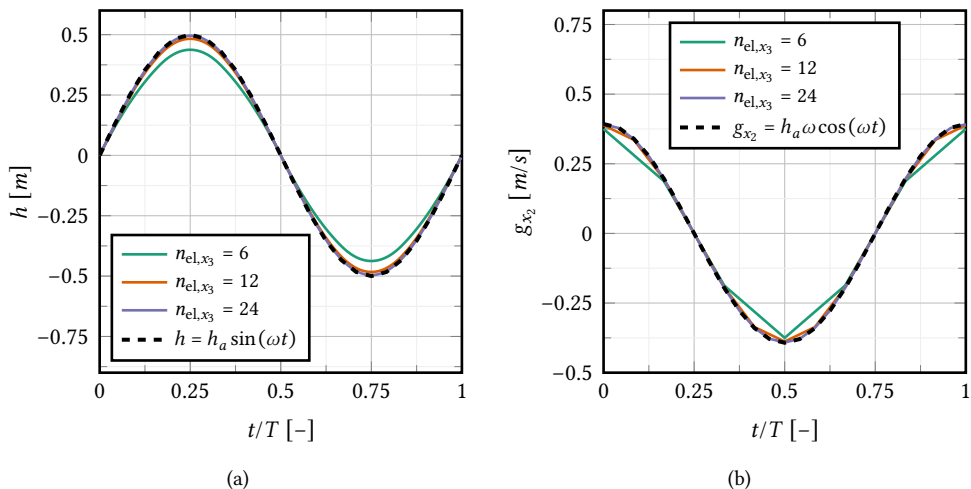


Figure 2.5: The motion h in (a) and velocity g_{x_2} in (b) of the hydrofoil in x_2 -direction for 3 resolutions n_{el,x_3} in time direction and the analytical solution for a heave motion with $T = 8$ s.

2.4.3 Stationary hydrofoil

We simulate the flow past a stationary hydrofoil for angles of attack α ranging from 1° to 5° . The simulations are performed on a NACA0012 foil section with Reynolds number $\text{Re} = Uc/\nu = 1000$ where ν is the kinematic viscosity. We study the resulting drag coefficient C_d and lift coefficient C_l defined as:

$$C_d = \frac{2F_d}{\rho c U^2}, \quad (2.35a)$$

$$C_l = \frac{2F_l}{\rho c U^2}, \quad (2.35b)$$

where F_d is the force component in the flow direction, F_l the force component perpendicular to the flow direction, and ρ denotes the density.

We first consider the steady state setup. Figure 2.6 shows the results of the spatial grid convergence study for C_d and C_l using 4 different meshes of varying resolution. In the coarsest mesh the domain is discretized using 30 elements over the length of the hydrofoil, 15 elements between the hydrofoil and the inflow boundary, and 45 elements between the hydrofoil and the outflow boundary. The finer meshes are generated by refining the coarsest mesh across the entire domain, doubling the number of elements in each direction in every NURBS patch. We use a Richardson extrapolation to examine the limit $h/h_0 \rightarrow 0$ using the three finest meshes only, as the coarsest mesh is not in the asymptotic range. We find 1.57 and 1.34 for the order of convergence of the drag and lift, respectively. We choose the mesh with two refinements for our computations as this gives a balance between results and computational efforts. For this mesh the error is 0.13% and 0.08% for C_d and C_l respectively considering the extrapolated result for $h/h_0 \rightarrow 0$.

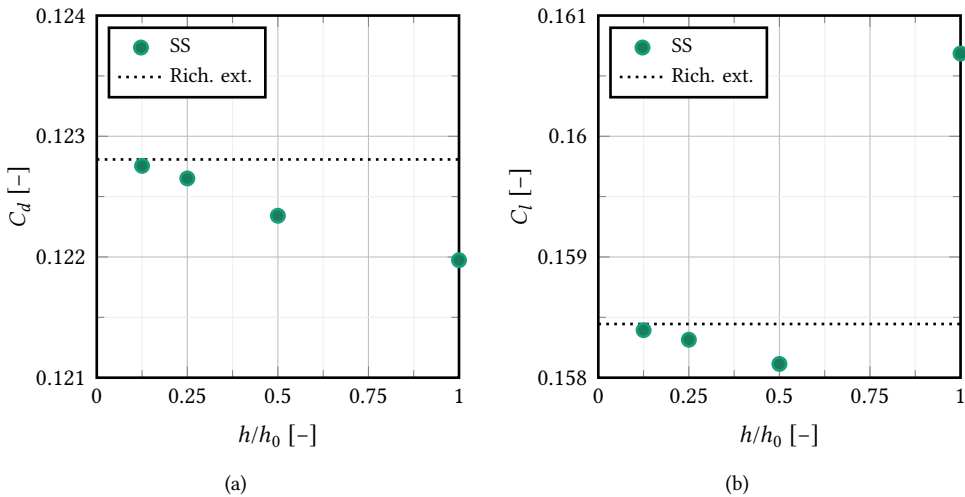


Figure 2.6: Results of steady state (SS) simulations for the drag coefficient C_d in (a) and lift coefficient C_l in (b) using four meshes and a Richardson extrapolation of the limit $h/h_0 \rightarrow 0$ based on the three finest meshes. The order of convergence is 1.57 and 1.34 for drag and lift respectively.

Next, we focus on the lift coefficient. Figure 2.7 shows C_l determined in stationary space-time and steady state simulations, supplemented with results from the literature. The computations are performed for 5 different angles of attack. The similarity of the results of the space-time and steady state simulations demonstrates that the spatial convergence of steady state simulations is indeed sufficient for space-time simulations. Moreover, the results are in good agreement with the results from the literature.

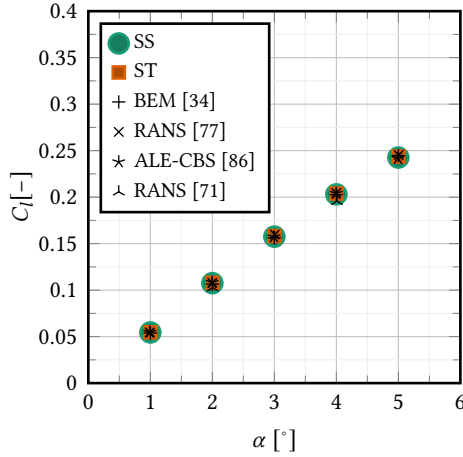


Figure 2.7: Lift coefficient C_l at $Re = 1000$ of a stationary NACA0012 hydrofoil for several angles of attack α determined using the proposed method and a steady state (SS) solution supplemented with results from the literature.

We compare with (i) a Boundary Element Method (BEM) with viscous correction Xfoil [34], (ii) the Reynolds Averaged Navier Stokes (RANS) solver Ansys Fluent [77], (iii) an Arbitrary-Lagrangian-Eulerian Characteristic Based Split Scheme (ALE-CBS) solver [86], and (iv) other Ansys Fluent computations [71]. The last computations are only available for the angles of attack of 2° and 4° . The numerical results obtained with this solver deviate more from the results that we have obtained. Lastly, we note that we have verified the force signal of the space-time simulations to be constant in time. This demonstrates that our method correctly predicts steady flow.

2.4.4 Heaving hydrofoil at a low reduced frequency

In this test case, we simulate a slowly heaving hydrofoil. The hydrofoil is oscillating at a low reduced frequency $k = \pi c/(TU)$. We note that the effect of the unsteady wake on the flow past the hydrofoil is very low [142] and added mass effects are negligible. As a consequence, the forces on the hydrofoil should match these from quasi-static simulations. We obtain the quasi-static results using stationary steady state simulations where we compensate the angle of attack α for inflow due to the heave motion. This provides the effective angle of attack:

$$\alpha_{\text{eff}} = \alpha - \arctan\left(\frac{2\pi h_a \cos(2\pi T^{-1}t)}{TU}\right). \quad (2.36)$$

The simulations are performed with $\text{Re} = 1000$, $k = 0.01$, $h_a = 0.1 \text{ m}$ and $\alpha = 0^\circ$. We use the same spatial discretization as for the stationary cases. In the temporal direction we use $n_{\text{el},x_3} = 24$. We note that further refinement does not improve the numerical results.

We visualize the convergence of the residuals in Figure 2.8a. We have verified that using stricter convergence criteria does not improve the solution quality. In Figure 2.8b we show C_l and C_d for the space-time and steady state simulations. We observe that both C_l and C_d agree with the quasi-static results.

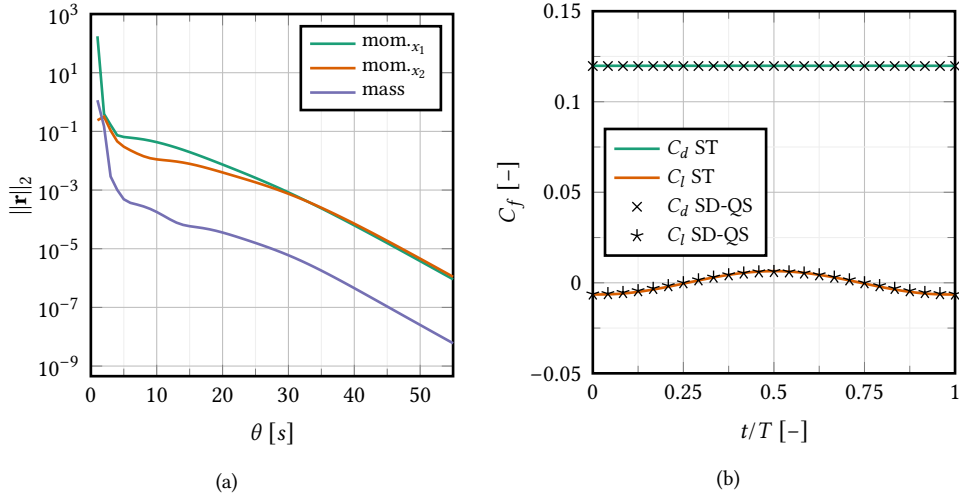


Figure 2.8: The convergence and results of the case of a slowly sinusoidal heaving NACA0012 hydrofoil with $k = 0.01$ and $\text{Re} = 1000$: a) L^2 -norm of the residuals at the start of the first Newton iteration of space-time momentum and mass conservation over pseudo-time θ ; b) Force coefficients $C_f = C_d, C_l$ in space-time (ST) compared to semi-discrete quasi-static (SD-QS) results.

2.4.5 Hydrofoil with large angle pitch motion

In this last test case, we focus on the prediction of the history effects in the wake. We simulate the flow past a sinusoidal pitching NACA0015 hydrofoil. The hydrofoil pitches around the $1/3$ chord with motion $\alpha(t) = \alpha_a \sin(2\pi t/T)$, where the amplitude is $\alpha_a = 23^\circ$, the Reynolds number is $\text{Re} = 1100$ and frequency is $k = 0.377$.

The same case is studied by [73] using Ansys Fluent. Their simulation setup uses an impulsive start and at least 20 large time steps to move the wake downstream of the hydrofoil. Their simulation is pursued with more than 2000 time steps per period. Its result is considered periodic if the maximum variation in mean statistics between the last cycles is 0.1%. In our setup we use the same spatial discretization as in our previous space-time simulations. To accurately capture the flow characteristics, we apply two extra refinements in the temporal direction. We note that further refinement does not yield improved solution quality.

In Figure 2.9 we show a time signal of the lift coefficient C_l . In general we observe good agreement between our result and the result of [73]. We see small differences in the regions $0.10 < t/T < 0.43$ and $0.58 < t/T < 0.84$. One important difference between our setup and the simulation in [73] is that our solution is exactly periodic which is not the case in the reference computation.

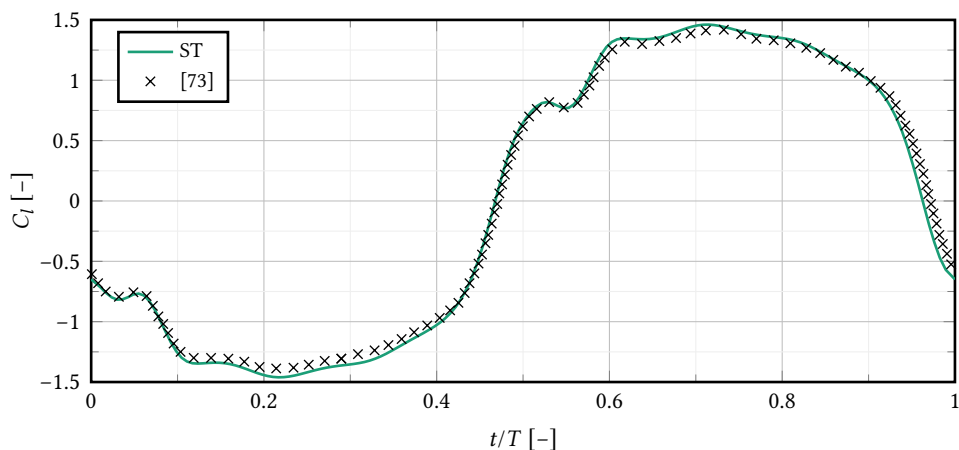


Figure 2.9: Lift coefficient C_l over time of a pitching NACA0015 hydrofoil with $\alpha_a = 23^\circ$, l and $\text{Re} = 1100$.

In Figures 2.10, 2.11 and 2.12 we show the velocity and pressure fields for 8 moments in time. Note the periodic solution behavior. This is most apparent in the flow behind the hydrofoil when comparing the velocity field at $t/T = 7/8$ and $t/T = 0$. Furthermore, note that the flow is symmetric around the x -axis. To see this, compare for instance the velocity field at $t/T = 0$ with $t/T = 4/8$ and $t/T = 2/8$ with $t/T = 6/8$. Both figures illustrate that the effect of the history in the wake is correctly predicted.

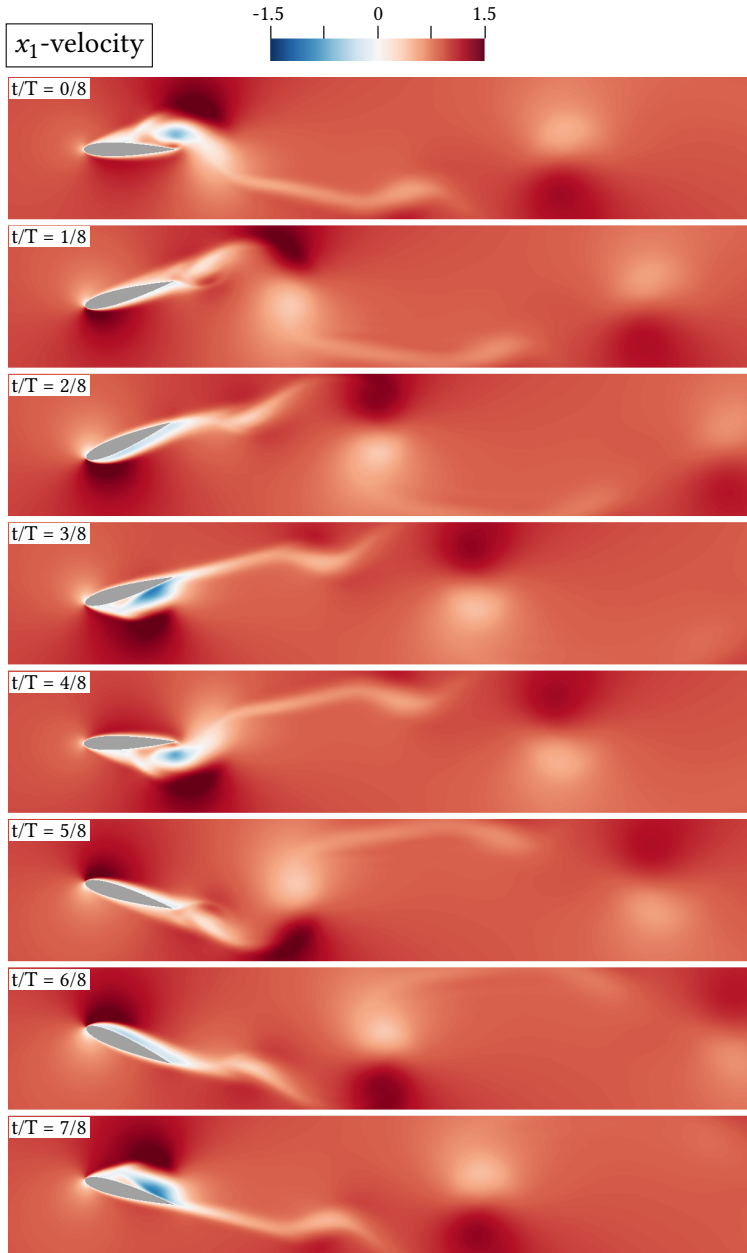


Figure 2.10: Velocity in x_1 -direction of a pitching hydrofoil with an angle of 23° and a period $T = 8.33$ s for 8 moments in time. $Re = 1100$. Visualized using VisIt [24].

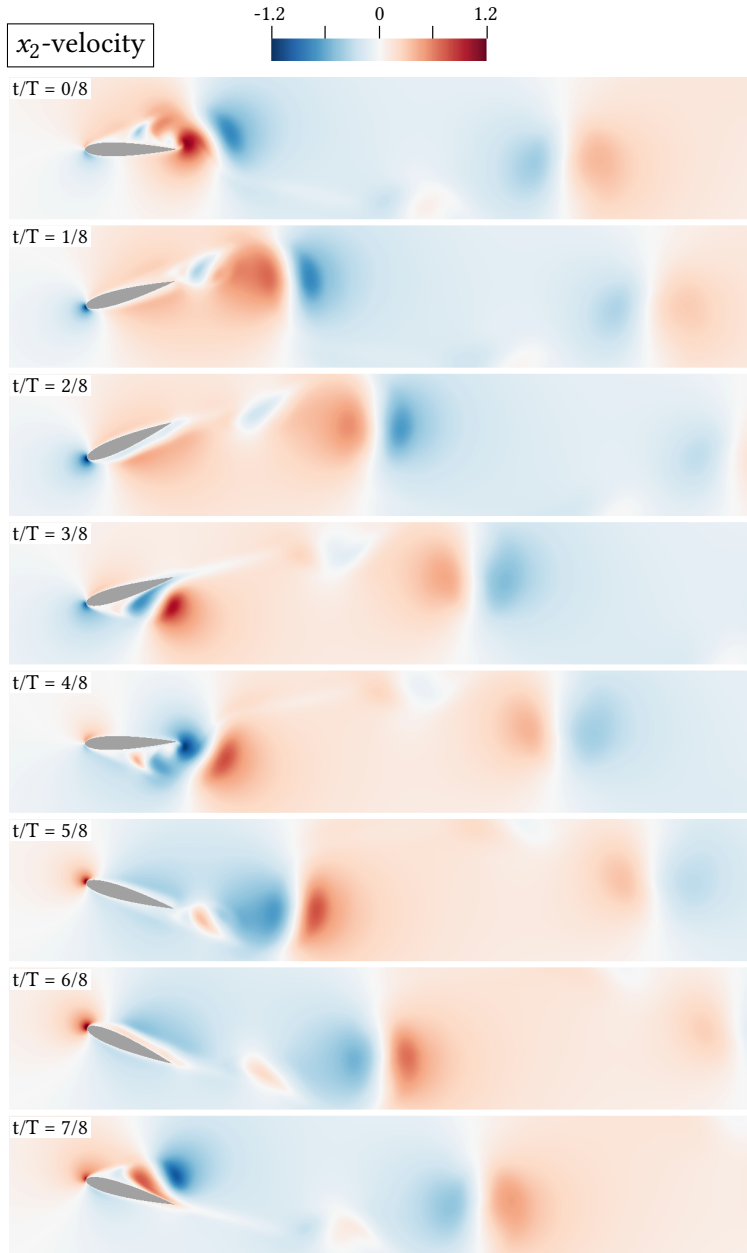


Figure 2.11: Velocity in x_2 -direction of a pitching hydrofoil with an angle of 23° and a period $T = 8.33$ s for 8 moments in time. $Re = 1100$. Visualized using VisIt [24].

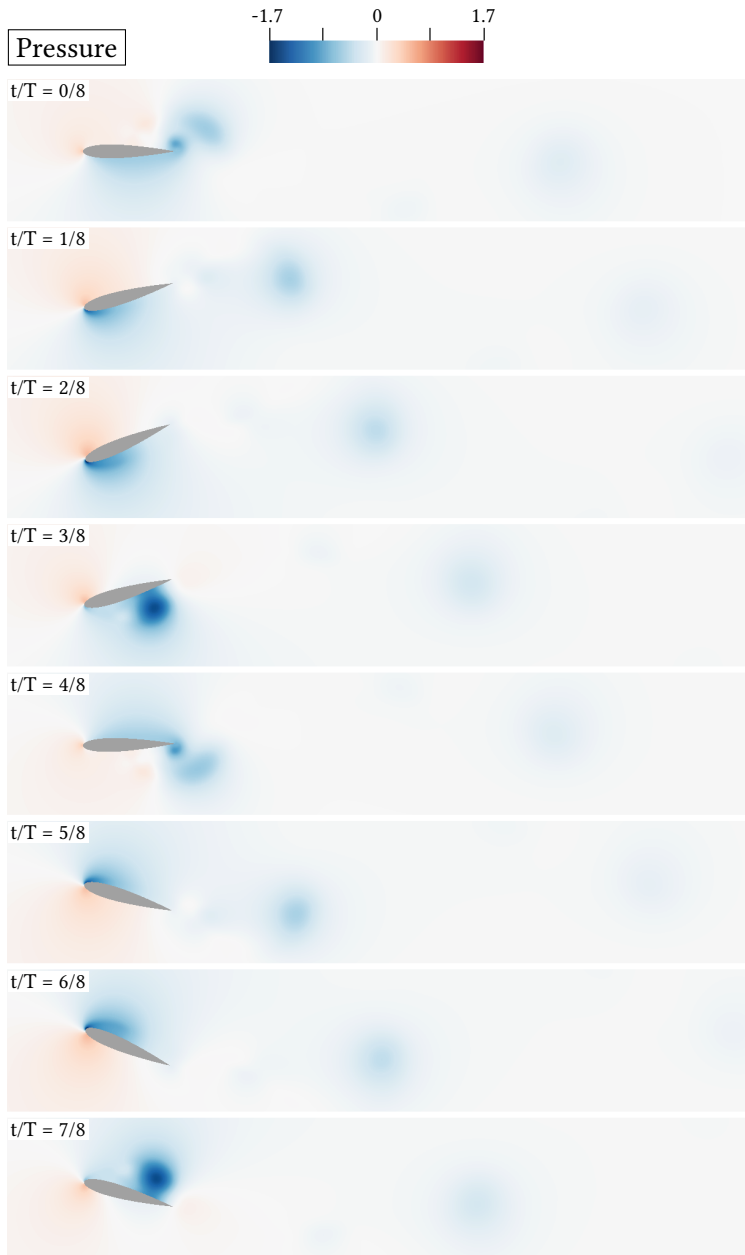


Figure 2.12: Pressure in the flow past a pitching hydrofoil with an angle of 23° and a period $T = 8.33$ s for 8 moments in time. $Re = 1100$. Visualized using VisIt [24].

2.5 Conclusions

In this work we present a time-periodic continuous space-time computational setup to simulate flow past periodically moving objects. This ensures that the flow is exactly periodic, and precludes working with needlessly long time domains. We enforce the time-periodicity constraint as a boundary condition in time. This changes the time-dependent two-dimensional problem into a three-dimensional boundary value problem in both space and time. The method employs isogeometric analysis to achieve higher-order smoothness in space and time. We discretize the formulation using residual-based variational turbulence modeling in which turbulent eddy viscosities are absent. Furthermore, we use weak boundary conditions to enhance the accuracy near the moving boundaries of the computational domain and pseudo-transient continuation to overcome some of the difficulties related to the saddle-point nature of the underlying problem. Here, we also employed artificial compressibility, this provided a reduction in simulation time. We show the conservation properties of the formulation and use a conservative traction evaluation. Numerical experiments on flow past stationary and moving hydrofoils demonstrate very good accuracy, even on coarse meshes. The computed drag and lift coefficients match with results from the literature and history effects in the wake are accurately captured.

We outline two possible further research directions. First, the computational setup should be extended to three spatial dimensions (i.e. the corresponding boundary value problem is four-dimensional). Second, exploring the benefits of the computational setup in the reduced order modeling context could yield various advantages. The transformation of the time-dependent problem into a boundary value problem might allow for faster and more accurate evaluation of reduced order models for periodic flows.

3

Projection-based reduced-order modelling of time-periodic problems

Simulating forced time-periodic flows in industrial applications presents significant computational challenges, partly due to the need to overcome costly transients before achieving time-periodicity. Reduced-order modelling emerges as a promising method to speed-up computations. We extend upon the work in Chapter 2 [88], where a time-periodic space-time model is introduced. We present a time-periodic reduced-order model that directly finds the time-periodic solution without requiring extensive time integration. The reduced-order model gives a reduction in variables in both space and time. Our approach involves a POD-Galerkin reduced-order model based on a time-periodic full-order model that employs isogeometric analysis, residual-based variational multiscale turbulence modelling and weak boundary conditions. The projection-based reduced-order model inherits these features. We evaluate the reduced-order model with numerical experiments on moving hydrofoils. The motion is known a priori and we restrict ourselves to two spatial dimensions. In these experiments, we vary the Strouhal and Reynolds numbers, and the motion profile respectively. Reduced-order model solutions agree well with those of the full-order model. The errors over the entire time period of thrust and lift forces are less than 0.2%. This includes complex scenarios such as the transition from drag to thrust production with increasing Strouhal number. Our time-periodic reduced-order model offers speed-ups ranging from $\mathcal{O}(10^2)$ - $\mathcal{O}(10^3)$ compared to the full-order model, depending upon the basis size. This makes it an appealing solution for prescribed time-periodic problems, with potential for additional speedup through nonlinear reduction techniques such as hyper-reduction.

This chapter is published as:

[89] **J. E. Lotz**, G. D. P. Weymouth, I. Akkerman, “Projection-based reduced-order modelling of time-periodic problems, with application to flow past flapping hydrofoils”, *Computer Methods in Applied Mechanics and Engineering* **429**, 117161 (2024)

3.1 Introduction

3 Finding a time-periodic solution of the flow past a prescribed periodically moving object using the Navier-Stokes equation is often associated with significant computational cost. Usually, a solution is found by integrating an initial condition over a sufficiently long time for a time-periodic solution to emerge. This transient phase usually consists of several periods. This makes these computations expensive in industrial applications, such as wind farm and propeller optimization. To overcome this problem, we explore the use of reduced-order models for speeding up this type of computations. Here, model assumptions or data are used to approximate the solution of the original model, the full-order model. In this work we focus on projection-based reduced-order models, where the full-order model is projected onto a reduced basis. This reduced basis is constructed from simulation data using proper orthogonal decomposition (POD). In this chapter, we introduce a reduced-order model that directly solves the time-periodic solution, eliminating the need for time integration. By leveraging the advantages of a space-time discretization, where space and time are treated equally, we achieve a reduction in degrees of freedom in both space and time.

In the literature, various techniques are developed to obtain periodic solutions more efficiently. The shooting method is one of these methods [66, 117, 119]. It involves converting the time-periodic boundary value problem into an initial value problem. The objective is then to determine the correct initial condition that satisfies the original, possibly expensive, boundary value problem. Another cost-effective alternative is the spectral method [51, 54]. The flow variables are represented by a Fourier series in time, facilitating the direct solution of periodic flows. This approach may face challenges in accurately capturing non-sinusoidal motion due to the rapid increase in the required number of Fourier modes. In the present study, we aim to develop an economical method for computing periodic solutions without assumptions on the motion. We use a time-periodic full-order model [53, 88, 109, 123] to create a POD-Galerkin reduced-order model. This full-order model is introduced in Chapter 2.

The stability of a reduced-order model is not guaranteed and a considerable amount of research is devoted to it. Instabilities of reduced-order models can be classified into at least two, and possibly more [52, 127], classes: inf-sup instabilities, related to solving a saddle point problem, and instabilities due to convection-dominated flows. For the first class of instabilities, efforts have been made in velocity-only reduced-order models [2, 87, 91]. However, many numerical methods for ob-

taining the snapshots do not provide pointwise divergence-free flow fields [21, 87], and neglecting the pressure term can lead to instabilities and large amplitude errors in the Galerkin model [103]. An attractive alternative is to enforce a solenoidal basis, which requires a Piola transform for data associated with essential boundary conditions [46]. For velocity-pressure reduced-order models, it is possible to enrich the velocity space with a supremizer, providing an additional set of degrees of freedom to solve for [8, 65, 120, 128]. For instabilities of the second class, subgrid closure models are a promising approach. This involves the modelling of the eddy viscosity of the missing modes [64, 114] or dynamic subgrid scales [143]. A successful alternative is the application of the variational multi-scale method [12] at both full-order and reduced-order model levels [29, 115, 127, 134], which does not require additional supremizers or a solenoidal basis, as it provides an inf-sup stable model [19, 115, 127]. Alternatives to subgrid closure models can be found in e.g. data-driven techniques [55, 65, 101] or the use of neural networks [5, 124, 145]. We stabilize the reduced-order model with the variational multi-scale method, following the work in [115].

We first consider the full-order model, which is a variational multi-scale method [12] using isogeometric analysis [58] adapted for time-periodic space-time [88]. By solving the time domain monolithically, we are able to impose the time-periodic constraints a priori. We effectively transform the initial value problem into a boundary value problem. The dimension of the domain is increased by one, but it allows us to enforce the time-periodic constraint as a classic periodic boundary condition. The motion of the periodically moving object is considered known and is accommodated by appropriately shaping the space-time mesh in advance. We construct the reduced-order model by applying a Galerkin projection of the full-order model on a time-periodic basis. The basis is computed by means of a proper orthogonal decomposition of a snapshot matrix of which each entry is the entire periodic space-time solutions of the full-order model for a chosen parameter set. The resulting time-periodic reduced-order model, like the full-order model, directly computes the entire space-time solution. We evaluate the quality of the computed solution fields and forces by comparing them with the full-order model for three numerical experiments. The experiments evaluate the reduced-order model for a variation of the Strouhal number, Reynolds number or motion shape for a periodically moving hydrofoil in two dimensions. The first experiment is studied more elaborately. It examines the transition from drag to thrust production as the Strouhal number increases. For this experiment, we also study the effect of the basis size on solution quality and speed-up. In the last two experiments, we study the effect of the Reynolds number or motion shape on lift and drag.

3.2 Full-order and reduced-order model for the time-periodic incompressible flow

In this work, we transform the initial value problem into a boundary value problem. This is achieved by treating time analogously to space. Our notation reflects this analogy by disguising the time as an additional spatial dimension. Therefore, we directly obtain a time-periodic solution in both the full-order and reduced-order model. This approach eliminates the need for separate time integration. We use the space-time full-order model for periodic flow as described in Chapter 2 [88].

For the reduced-order model, we consider a standard POD-Galerkin model. We are able to use this standard reduced order model as we effectively solve a boundary value problem. The reduced-order model gives a reduction of the number of variables in both spatial and temporal dimensions.

To provide a self-contained and reproducible work, we reproduce the strong formulation and discrete weak formulation of the model problem in the first two sections. For further details of the model, we refer to the original work.

3.2.1 Strong formulation of time-periodic incompressible flow

We consider incompressible flow on a periodically deforming domain $\Omega(t) = \Omega(t + T)$, where T is the period. We assume the unknown velocity \mathbf{u} and pressure p exhibit the same periodicity, that is $\mathbf{u}(\mathbf{x}, t) = \mathbf{u}(\mathbf{x}, t + T)$ and $p(\mathbf{x}, t) = p(\mathbf{x}, t + T)$. The boundary is composed of an exterior part Γ_{ext} and a periodic time-dependent interior $\Gamma_{\text{int}}(t)$. We introduce the normal velocity $u_n = \mathbf{u} \cdot \mathbf{n}$ with positive and negative parts $u_n^\pm = \frac{1}{2}(u_n \pm |u_n|)$. The exterior boundary is further separated in an inflow and outflow part,

$$\Gamma_{\text{ext}}^D := \{\mathbf{x} \in \Gamma_{\text{ext}} \mid u_n(\mathbf{x}) < 0\}, \quad (3.1a)$$

$$\Gamma_{\text{ext}}^N := \{\mathbf{x} \in \Gamma_{\text{ext}} \mid u_n(\mathbf{x}) \geq 0\}, \quad (3.1b)$$

where the superscripts refer to the Dirichlet and Neumann boundary conditions that will be imposed on these parts. Figure 3.1 depicts a sketch of a spatial domain Ω , similar to the one we will consider in Section 3.3.

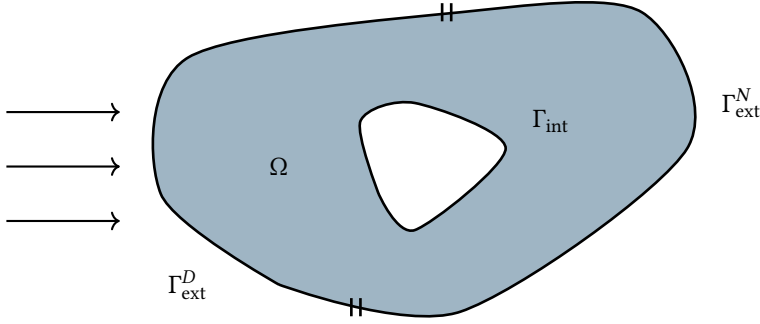


Figure 3.1: Sketch of the spatial domain with its boundaries, with inflow on the left.

We extrude the spatial domain over the time domain $\mathcal{I} = [0, T]$ to obtain a continuous space-time domain Q with space-time boundaries P_{ext} and P_{int} . Here, $P_{\text{ext}} = \Gamma_{\text{ext}} \times \mathcal{I}$ while Q and P_{int} are deformed version of $\Omega \times \mathcal{I}$ and $\Gamma \times \mathcal{I}$ to accommodate the motion.

We denote the space-time coordinate, using the time direction $d + 1$, as $\hat{\mathbf{x}}^T = [\mathbf{x}^T \ st] = [x_1 \dots x_d \ sx_{d+1}]$ and the extended velocity vector as $\hat{\mathbf{u}}^T = [\mathbf{u}^T \ s]$. Note that t is scaled with a reference velocity s to ensure dimensional consistency.

We substitute the traditional initial condition

$$\mathbf{u}(\cdot, 0) = \mathbf{u}_0(\cdot) \quad \text{in } \Omega, \quad (3.2)$$

with its time-periodic counterpart

$$\mathbf{u}(\cdot, 0) = \mathbf{u}(\cdot, T) \quad \text{in } \Omega, \quad (3.3)$$

which transforms an initial value problem into a boundary value problem. To make this point more clear we chose to denote the material derivative as

$$\partial_t \mathbf{u} + \mathbf{u} \cdot \nabla \mathbf{u} = \hat{\mathbf{u}} \cdot \nabla_{\hat{\mathbf{x}}} \mathbf{u}, \quad (3.4)$$

resulting in the Navier-Stokes equations for time-periodic incompressible flow,

$$\hat{\mathbf{u}} \cdot \nabla_{\hat{\mathbf{x}}} \mathbf{u} + \nabla p - \nu \nabla^2 \mathbf{u} = \mathbf{f} \quad \text{in } Q, \quad (3.5a)$$

$$\nabla \cdot \mathbf{u} = 0 \quad \text{in } Q, \quad (3.5b)$$

$$\mathbf{u} = \mathbf{g}_{\text{int}} \quad \text{in } P_{\text{int}}, \quad (3.5c)$$

$$\mathbf{u} = \mathbf{g}_{\text{ext}} \quad \text{in } P_{\text{ext}}^D, \quad (3.5d)$$

$$-p\mathbf{n} + \nu \nabla \mathbf{u} \cdot \mathbf{n} + u_n^- \mathbf{u} = \mathbf{0} \quad \text{in } P_{\text{ext}}^N, \quad (3.5e)$$

$$\mathbf{u}(\cdot, 0) = \mathbf{u}(\cdot, T) \quad \text{in } \Omega, \quad (3.5f)$$

where ν is the kinematic viscosity, \mathbf{f} is an external force and \mathbf{g}_{int} and \mathbf{g}_{ext} are prescribed velocities on the interior and exterior boundary.

The first two equations state the balance of linear momentum (3.5a) and mass (3.5b), respectively. Subsequently, the Dirichlet boundary conditions (3.5c) and (3.5d) prescribe the velocity on the interior and the inflow boundary. While (3.5e) governs the outflow boundary. Finally, (3.5f) enforces the time-periodic condition.

3.2.2 Discrete weak formulation of time-periodic incompressible flow

Converting the strong form, as given in the previous section, into a discrete formulation involves a couple of steps. First, we convert the strong form into a weak form, by multiplying the two balance equations with appropriate test-functions, integrating over the domain and applying integration by parts on the pressure and diffusion terms.

Subsequently, we discretize the formulation by decomposing the domain Q in non-overlapping elements Q_e . For ease of notation, we also define the union of element interiors as $\tilde{Q} = \bigcup Q_e$. We define simple polynomial (or rational) functions on each element and construct approximate function spaces, denoted as \mathcal{W}^h , by combining these appropriately.

Last, we stabilize the discrete formulation by accounting explicitly for the subgrid-scale effects. For this, we apply residual-based variational multiscale turbulence modelling as stabilization [11, 12]. We split \mathbf{u} and p into coarse-scale, denoted by h , and small-scale components, denoted with $'$,

$$\{\mathbf{u}, p\} = \{\mathbf{u}^h, p^h\} + \{\mathbf{u}', p'\}. \quad (3.6)$$

The small-scale components will be accounted for by a model.

For improved robustness, we choose to enforce the Dirichlet conditions weakly and added some residual-based discontinuity capturing. The resulting discrete variational formulation of (3.5) is similar to Chapter 2 [88]. After these choices, the discrete problem is stated as follows:

Find $\mathbf{U}^h = \{\mathbf{u}^h, p^h\} \in \mathcal{W}^h$ such that for all $\mathbf{W} = \{\mathbf{w}^h, q^h\} \in \mathcal{W}^h$:

$$B(\mathbf{U}^h, \mathbf{W}^h) = 0, \quad (3.7a)$$

where

$$B(U^h, \mathbf{W}^h) = B_{\text{GAL}}(U^h, \mathbf{W}^h) + B_{\text{VMS}}(U^h, \mathbf{W}^h) + B_{\text{WBC}}(U^h, \mathbf{W}^h) + B_{\text{DC}}(U^h, \mathbf{W}^h), \quad (3.7b)$$

$$B_{\text{GAL}}(U^h, \mathbf{W}^h) = (\mathbf{w}^h, \hat{\mathbf{u}}^h \cdot \nabla_{\hat{\mathbf{x}}} \mathbf{u}^h)_Q - (\nabla \cdot \mathbf{w}^h, p^h)_Q + (\nabla \mathbf{w}^h, \nu \nabla \mathbf{u}^h)_Q + (q^h, \nabla \cdot \mathbf{u}^h)_Q - (\mathbf{w}^h, u_n^{-h} \mathbf{u}^h)_{P_{\text{ext}}^N} - (\mathbf{w}^h, \mathbf{f})_Q, \quad (3.7c)$$

$$B_{\text{VMS}}(U^h, \mathbf{W}^h) = -(\nabla_{\hat{\mathbf{x}}} \mathbf{w}^h, \mathbf{u}' \otimes \hat{\mathbf{u}}^h)_{\tilde{Q}} - (\nabla \mathbf{w}^h, \mathbf{u}^h \otimes \mathbf{u}')_{\tilde{Q}} - (\nabla \mathbf{w}^h, \mathbf{u}' \otimes \mathbf{u}')_{\tilde{Q}} - (\nabla q^h, \mathbf{u}')_{\tilde{Q}} - (\nabla \cdot \mathbf{w}^h, p')_{\tilde{Q}}, \quad (3.7d)$$

$$B_{\text{WBC}}(U^h, \mathbf{W}^h) = (\mathbf{w}^h, p^h \mathbf{n} - \nu \nabla \mathbf{u}^h \cdot \mathbf{n})_{P_{\text{int}}} + (\nu \nabla \mathbf{w}^h \cdot \mathbf{n} - q^h \mathbf{n}, \mathbf{u}^h - \mathbf{g}_{\text{int}})_{P_{\text{int}}} + (\mathbf{w}^h \tau_b, \mathbf{u}^h - \mathbf{g}_{\text{int}})_{P_{\text{int}}}, \quad (3.7e)$$

$$B_{\text{DC}}(U^h, \mathbf{W}^h) = (\nabla \mathbf{w}^h, \nu_{dc} \nabla \mathbf{u}^h)_Q. \quad (3.7f)$$

Note: we have adopted the standard notation for the L_2 innerproduct, that is $(\mathbf{f}, \mathbf{g})_D = \int_D \mathbf{f} \cdot \mathbf{g} \, dD$.

In (3.7d) the small-scale velocities \mathbf{u}' and the small-scale pressure p' are modelled as

$$\mathbf{u}' = -\tau_M \mathbf{r}_M, \quad (3.8a)$$

$$p' = -\tau_C r_C, \quad (3.8b)$$

where τ_M and τ_C are stability parameters and \mathbf{r}_M and r_C are the strong form residuals defined as

$$\mathbf{r}_M = (\hat{\mathbf{u}}^h \cdot \nabla_{\hat{\mathbf{x}}}) \mathbf{u}^h - \nabla p - \nu \nabla^2 \mathbf{u}^h - \mathbf{f}, \quad (3.9a)$$

$$r_C = \nabla \cdot \mathbf{u}^h. \quad (3.9b)$$

The small-scale contributions directly depend on the strong residuals, ensuring their consistency. For the stabilization parameters we use

$$\tau_M = (\hat{\mathbf{u}}^h \cdot \hat{\mathbf{G}} \hat{\mathbf{u}}^h + C_I \nu^2 \mathbf{G} : \mathbf{G})^{-1/2}, \quad (3.10a)$$

$$\tau_C = \tau_M^{-1} \text{Tr}(\mathbf{G})^{-1}, \quad (3.10b)$$

where C_I is a user-provided input related to the inverse estimate, while $\hat{\mathbf{G}}$ and \mathbf{G} are two metric tensors providing size and deformation information of the current element. The space-time metric tensor $\hat{\mathbf{G}}$ and the spatial metric tensor \mathbf{G} are defined as

$$\hat{\mathbf{G}} = \left(\frac{\partial \xi}{\partial \hat{\mathbf{x}}} \right)^T \mathbf{G}_s \frac{\partial \xi}{\partial \hat{\mathbf{x}}}, \quad \mathbf{G} = \left(\frac{\partial \xi}{\partial \mathbf{x}} \right)^T \frac{\partial \xi}{\partial \mathbf{x}}, \quad \text{with} \quad \mathbf{G}_s = \begin{bmatrix} \mathbf{I}_{d \times d} & \mathbf{0}_{1 \times d} \\ \mathbf{0}_{d \times 1} & s^2 \end{bmatrix}. \quad (3.11)$$

The terms in (3.7e) result from the weak enforcement of the Dirichlet boundary condition. They consist of a consistency term, a dual consistency term and a penalty term. For the penalty parameter, we use

$$\tau_b = \frac{1}{2} C_b \nu (\mathbf{n} \cdot \mathbf{Gn})^{\frac{1}{2}}, \quad (3.12)$$

where C_b is a user-provided input related to a trace inequality.

The discontinuity capturing provided in (3.7e) results in additional diffusion in problem areas. The discontinuity capturing viscosity is inspired on [61],

$$\nu_{\text{dc}} = 2 \frac{C_{\text{dc}}}{\text{Tr}(\mathbf{G})^{1/2}} \frac{\|\mathbf{r}_M\|_2}{\|\nabla \mathbf{u}^h\|_F}, \quad (3.13)$$

where $\|\cdot\|_F$ denotes the Frobenius norm, and C_{dc} is a user defined coefficient. This type of discontinuity capturing viscosities is ubiquitous in the literature. Note that a VMS-based justification for this form of discontinuity capturing is given in [39, 40]. Similar to the stabilization terms the additional viscosity scales with the size of the residual, this makes it a consistent term. This ensures the accuracy of the final solution.

These semi-linear forms in (3.7) are implemented using the MFEM library [3].

3.2.3 System of nonlinear ordinary differential equations

The formulation provided in (3.7) results in a non-linear system of algebraic equations. To aid the exposition of the reduced-order model in Section 3.2.4, we will explicitly provide this system here. We discretize the coarse scale variables with

$$u_1^h(\hat{\mathbf{x}}) = \boldsymbol{\phi}_{u_1} \cdot \mathbf{N}(\hat{\mathbf{x}}), \quad (3.14a)$$

$$u_2^h(\hat{\mathbf{x}}) = \boldsymbol{\phi}_{u_1} \cdot \mathbf{N}(\hat{\mathbf{x}}), \quad (3.14b)$$

$$p^h(\hat{\mathbf{x}}) = \boldsymbol{\phi}_p \cdot \mathbf{N}(\hat{\mathbf{x}}), \quad (3.14c)$$

where $\mathbf{N}(\hat{\mathbf{x}})$ is the array of shape functions, and ϕ_{u_1} , ϕ_{u_2} and ϕ_p are the arrays with unknown coefficients of the entire space-time domain. Note that $N(\hat{\mathbf{x}})$ does not need to be split into spatial and temporal components, as space and time are treated the same in the continuous space-time discretization.

The bilinear form in (3.7) becomes of the form

$$B(U^h, \{\mathbf{N}, 0, 0\}) = \mathbf{b}_u + \mathbf{A}_{u_1 u_1} \phi_{u_1} + \mathbf{A}_{u_1 u_2} \phi_{u_2} + \mathbf{A}_{u_1 p} \phi_p + \mathbf{h}_{u_1}(\phi_{u_1}, \phi_{u_2}, \phi_p), \quad (3.15a)$$

$$B(U^h, \{0, \mathbf{N}, 0\}) = \mathbf{b}_{u_2} + \mathbf{A}_{u_2 u_1} \phi_{u_1} + \mathbf{A}_{u_2 u_2} \phi_{u_2} + \mathbf{A}_{u_2 p} \phi_p + \mathbf{h}_{u_2}(\phi_{u_1}, \phi_{u_2}, \phi_p), \quad (3.15b)$$

$$B(U^h, \{0, 0, \mathbf{N}\}) = \mathbf{b}_p + \mathbf{A}_{p u_1} \phi_{u_1} + \mathbf{A}_{p u_2} \phi_{u_2} + \mathbf{A}_{p p} \phi_p + \mathbf{h}_p(\phi_{u_1}, \phi_{u_2}, \phi_p), \quad (3.15c)$$

where \mathbf{b}_x are the zeroth order terms, \mathbf{A}_{xy} are the gradients defining the first order terms and $\mathbf{h}_x(\phi_{u_1}, \phi_{u_2}, \phi_p)$ are the remaining higher order terms. In matrix-vector form this becomes

$$\begin{bmatrix} \mathbf{A}_{u_1 u_1} & \mathbf{A}_{u_1 u_2} & \mathbf{A}_{u_1 p} \\ \mathbf{A}_{u_2 u_1} & \mathbf{A}_{u_2 u_2} & \mathbf{A}_{u_2 p} \\ \mathbf{A}_{p u_1} & \mathbf{A}_{p u_2} & \mathbf{A}_{p p} \end{bmatrix} \begin{bmatrix} \phi_{u_1} \\ \phi_{u_2} \\ \phi_p \end{bmatrix} + \begin{bmatrix} \mathbf{h}_{u_1}(\phi_{u_1}, \phi_{u_2}, \phi_p) \\ \mathbf{h}_{u_2}(\phi_{u_1}, \phi_{u_2}, \phi_p) \\ \mathbf{h}_p(\phi_{u_1}, \phi_{u_2}, \phi_p) \end{bmatrix} = - \begin{bmatrix} \mathbf{b}_{u_1} \\ \mathbf{b}_{u_2} \\ \mathbf{b}_p \end{bmatrix}. \quad (3.16)$$

For added robustness, we solve the nonlinear algebraic equations using a pseudo-time globalization technique. The pseudo-time is denoted by θ . In the discrete weak formulation in (3.7), both the momentum and continuity equation are augmented with a pseudo-time rate term. For dimensional consistency, we scale the rate term in the continuity equation appropriately. The parameter a can be interpreted as an artificial speed of sound, parametrizing pseudo-compressibility [26, 27, 135]. Note, this is with respect to pseudo-time. The actual time derivative in (3.4) is unaffected and consistency of the formulation is maintained. The discrete problem in becomes:

Given $\mathbf{U}^n = \{\mathbf{u}^n, p^n\} \in \mathcal{W}^h$ find $\mathbf{U}^{n+1} = \{\mathbf{u}^{n+1}, p^{n+1}\} \in \mathcal{W}^h$ such that for all $\mathbf{W} = \{\mathbf{w}^h, q^h\} \in \mathcal{W}^h$:

$$B(U(\mathbf{U}^n, \mathbf{U}^{n+1}), \mathbf{W}^h) + B_{\text{PT}}(\partial_\theta U(\mathbf{U}^n, \mathbf{U}^{n+1}), \mathbf{W}^h) = 0, \quad (3.17a)$$

where

$$B_{\text{PT}}(\partial_\theta U^h, \mathbf{W}^h) = (\mathbf{w}^h, \partial_\theta \mathbf{u}^h)_Q + \frac{1}{a^2} (q^h, \partial_\theta p^h)_Q. \quad (3.17b)$$

Additional interpolation rules for $U(U^n, U^{n+1})$ and $\partial_\theta U(U^n, U^{n+1})$ have to be specified to close the system. In this case, we select the backward Euler method, resulting in

$$U(U^n, U^{n+1}) = U^{n+1}, \quad (3.18a)$$

$$\partial_\theta U(U^n, U^{n+1}) = \frac{1}{\Delta\theta}(U^{n+1} - U^n), \quad (3.18b)$$

where $\Delta\theta$ is a user-specified pseudo-time step size.

Using the mass matrix,

$$\mathbf{M} = \int_Q \mathbf{N} \otimes \mathbf{N} d\mathbf{Q}, \quad (3.19)$$

and dropping the superscript gives the following non-linear system of algebraic equations:

$$\begin{aligned} \left(\frac{1}{\Delta\theta} \begin{bmatrix} \mathbf{M}_{u_1} & 0 & 0 \\ 0 & \mathbf{M}_{u_2} & 0 \\ 0 & 0 & \frac{1}{a^2} \mathbf{M}_p \end{bmatrix} + \begin{bmatrix} \mathbf{A}_{u_1 u_1} & \mathbf{A}_{u_1 u_2} & \mathbf{A}_{u_1 p} \\ \mathbf{A}_{u_2 u_1} & \mathbf{A}_{u_2 u_2} & \mathbf{A}_{u_2 p} \\ \mathbf{A}_{p u_1} & \mathbf{A}_{p u_2} & \mathbf{A}_{p p} \end{bmatrix} \right) \begin{bmatrix} \phi_u \\ \phi_v \\ \phi_p \end{bmatrix} \\ + \begin{bmatrix} \mathbf{h}_{u_1}(\phi_{u_1}, \phi_{u_2}, \phi_p) \\ \mathbf{h}_{u_2}(\phi_{u_1}, \phi_{u_2}, \phi_p) \\ \mathbf{h}_p(\phi_{u_1}, \phi_{u_2}, \phi_p) \end{bmatrix} = - \begin{bmatrix} \mathbf{b}_{u_1} \\ \mathbf{b}_{u_2} \\ \mathbf{b}_p \end{bmatrix} + \frac{1}{\Delta\theta} \begin{bmatrix} \mathbf{M}_{u_1} \phi_{u_1}^n \\ \mathbf{M}_{u_2} \phi_{u_2}^n \\ \frac{1}{a^2} \mathbf{M}_p \phi_p^n \end{bmatrix} \end{aligned} \quad (3.20)$$

Note that the time-dependent contributions are incorporated in the matrices \mathbf{A}_{xy} and vectors \mathbf{h}_x , while the pseudo-time contributions are represented by the first and last terms respectively. This problem is solved using a modified Newton iteration method, while the parallel sparse matrix problems are solved using precondition and GMRES provided by the Hypr library [44].

3.2.4 Reduced basis using Proper-Orthogonal Decomposition

The dimensionality n_f of the system of the full-order model in (3.20) is inherently large. This imposes a large computational effort. For scenarios involving solving numerous closely related problems, such as parameter studies or design optimization, there is an opportunity to mitigate this computational burden. We can reuse previously obtained solutions, leading to a remarkable reduction in computational effort with only a minor reduction in solution fidelity.

We find the reduced-order model basis \mathbf{V} using a discrete Proper Orthogonal Decomposition (POD) [90]. The POD generates a low-dimensional basis by finding meaningful behaviour in low-dimensional patterns of dynamic activity tailored to particular dynamics and parameters. The discrete POD consists of a singular value decomposition of a snapshot matrix \mathbf{X}_ϕ containing m full-order solutions in its columns. The full-order solutions are determined using a particular set of input parameters μ , which is a sample from a larger parameter space Θ . Each entry of the snapshot matrix contains one entire space-time solution of a full-order solution for a parameter set μ . The singular value decomposition is given as

$$\mathbf{X}_\phi = \Phi \Sigma \Psi^T, \quad (3.21)$$

where Φ contains the POD modes in the left singular vectors, Ψ gives the right singular vectors and Σ gives the singular values in the diagonal. The expansion coefficients of the ROM basis have standard algebraic orthogonality such that $\mathbf{V}^T \mathbf{V} = \mathbf{I}$. The singular values are ordered from smallest to largest with $\sigma_i < \sigma_{i+1} < \sigma_m$, indicating the relevance of the corresponding modes. We find the basis \mathbf{V} by choosing it as the first n_r columns of Φ based on a fraction of the missing energy in the basis

$$\epsilon_{\text{POD}} = \frac{\sum_i^{n_r} \sigma_i}{\sum_i^m \sigma_i}. \quad (3.22)$$

3.2.5 Projection-based reduced-order model

We reduce each variable separately and reduce the dimension of the system by restricting each variable to its own subspace. The reduced system approximates the entire space-time solution of the original system in a subspace spanned by a solution basis

$$\phi_{u_1} \approx \tilde{\phi}_{u_1} = \mathbf{V}_{u_1} \hat{\phi}_{u_1}, \quad (3.23a)$$

$$\phi_{u_2} \approx \tilde{\phi}_{u_2} = \mathbf{V}_{u_2} \hat{\phi}_{u_2}, \quad (3.23b)$$

$$\phi_p \approx \tilde{\phi}_p = \mathbf{V}_p \hat{\phi}_p. \quad (3.23c)$$

Here, ϕ_x is the sought for full-order solution, while $\tilde{\phi}_x$ is its the high-dimensional representation of the reduced-order model approximation ($\text{size}(\tilde{\phi}_x) = n_f$). Contrary $\hat{\phi}_x$ is the low dimensional representation and \mathbf{V}_x is the reduced basis as found in the previous section ($\text{size}(\hat{\phi}_x) = n_r$). The matrix \mathbf{V}_x serves as a linear map between the low-dimensional and high-dimensional representation of the reduced-order solution. The basis \mathbf{V}_x is composed of n_{r_x} space-time basis vectors \mathbf{v}_x as columns, $\mathbf{V}_x = \{\mathbf{v}_{x1}, \dots, \mathbf{v}_{xn_{r_x}}\}$ with $n_r \ll n_f$.

As the reduced-order model will be a direct projection of the full-order model, it implicitly uses the same stabilization as the full-order model. This is akin to work on POD-Galerkin reduced-order models with the variational multi-scale framework [19, 115, 127]. Upon substitution of (3.23) in (3.16), the number of unknowns reduces while the number of equations remains the same, resulting in an over-determined system. We apply a Galerkin projection to find the reduced system of equations. This is equivalent to using the subspace restriction of the trial-space on the test spaces as well.

In this case the full-order model (3.16) is reduced to

$$\begin{aligned} \begin{bmatrix} \mathbf{V}_{u_1} \\ \mathbf{V}_{u_2} \\ \mathbf{V}_p \end{bmatrix}^T \begin{bmatrix} \mathbf{A}_{u_1 u_1} & \mathbf{A}_{u_1 u_2} & \mathbf{A}_{u_1 p} \\ \mathbf{A}_{u_2 u_1} & \mathbf{A}_{u_2 u_2} & \mathbf{A}_{u_2 p} \\ \mathbf{A}_{p u_1} & \mathbf{A}_{p u_2} & \mathbf{A}_{pp} \end{bmatrix} \begin{bmatrix} \mathbf{V}_{u_1} \boldsymbol{\phi}_{u_1} \\ \mathbf{V}_{u_2} \boldsymbol{\phi}_{u_2} \\ \mathbf{V}_p \boldsymbol{\phi}_p \end{bmatrix} \\ + \begin{bmatrix} \mathbf{V}_{u_1} \\ \mathbf{V}_{u_2} \\ \mathbf{V}_p \end{bmatrix}^T \begin{bmatrix} \mathbf{h}_{u_1}(\mathbf{V}_{u_1} \boldsymbol{\phi}_{u_1}, \mathbf{V}_{u_2} \boldsymbol{\phi}_{u_2}, \mathbf{V}_p \boldsymbol{\phi}_p) \\ \mathbf{h}_{u_2}(\mathbf{V}_{u_1} \boldsymbol{\phi}_{u_1}, \mathbf{V}_{u_2} \boldsymbol{\phi}_{u_2}, \mathbf{V}_p \boldsymbol{\phi}_p) \\ \mathbf{h}_p(\mathbf{V}_{u_1} \boldsymbol{\phi}_{u_1}, \mathbf{V}_{u_2} \boldsymbol{\phi}_{u_2}, \mathbf{V}_p \boldsymbol{\phi}_p) \end{bmatrix} = - \begin{bmatrix} \mathbf{V}_{u_1} \\ \mathbf{V}_{u_2} \\ \mathbf{V}_p \end{bmatrix}^T \begin{bmatrix} \mathbf{b}_{u_1} \\ \mathbf{b}_{u_2} \\ \mathbf{b}_p \end{bmatrix}, \end{aligned} \quad (3.24)$$

which can be alternatively written as

$$\begin{bmatrix} \hat{\mathbf{A}}_{u_1 u_1} & \hat{\mathbf{A}}_{u_1 u_2} & \hat{\mathbf{A}}_{u_1 p} \\ \hat{\mathbf{A}}_{u_2 u_1} & \hat{\mathbf{A}}_{u_2 u_2} & \hat{\mathbf{A}}_{u_2 p} \\ \hat{\mathbf{A}}_{p u_1} & \hat{\mathbf{A}}_{p u_2} & \hat{\mathbf{A}}_{pp} \end{bmatrix} \begin{bmatrix} \hat{\boldsymbol{\phi}}_{u_1} \\ \hat{\boldsymbol{\phi}}_{u_2} \\ \hat{\boldsymbol{\phi}}_p \end{bmatrix} + \begin{bmatrix} \hat{\mathbf{h}}_{u_1}(\mathbf{V}_{u_1} \hat{\boldsymbol{\phi}}_{u_1}, \mathbf{V}_{u_2} \hat{\boldsymbol{\phi}}_{u_2}, \mathbf{V}_p \hat{\boldsymbol{\phi}}_p) \\ \hat{\mathbf{h}}_{u_2}(\mathbf{V}_{u_1} \hat{\boldsymbol{\phi}}_{u_1}, \mathbf{V}_{u_2} \hat{\boldsymbol{\phi}}_{u_2}, \mathbf{V}_p \hat{\boldsymbol{\phi}}_p) \\ \hat{\mathbf{h}}_p(\mathbf{V}_{u_1} \hat{\boldsymbol{\phi}}_{u_1}, \mathbf{V}_{u_2} \hat{\boldsymbol{\phi}}_{u_2}, \mathbf{V}_p \hat{\boldsymbol{\phi}}_p) \end{bmatrix} = - \begin{bmatrix} \hat{\mathbf{b}}_{u_1} \\ \hat{\mathbf{b}}_{u_2} \\ \hat{\mathbf{b}}_p \end{bmatrix}, \quad (3.25)$$

where

$$\hat{\mathbf{A}}_{xy} = \mathbf{V}_x^T \mathbf{A}_{xy} \mathbf{V}_y, \quad (3.26a)$$

$$\hat{\mathbf{h}}_x(\cdot) = \mathbf{V}_x^T \mathbf{h}_x(\cdot), \quad (3.26b)$$

$$\hat{\mathbf{b}}_x = \mathbf{V}_x^T \mathbf{b}_x. \quad (3.26c)$$

Note that $\hat{\mathbf{A}}_{xy}$ can be precomputed if it is independent of parameter μ . Additionally, it is worth noting that we do not use pseudo-time as a globalization technique in the reduced-order model. The non-linearity did not pose issues in solving the problem. The reduced-order model is unable to represent arbitrary unphysical flow features as it is constrained by the basis. We conjecture that this is the reason that a globalization technique such as pseudo-time is not needed in the reduced-order mode. Our experience showed that it was not necessary.

For obtaining the POD basis and implementing the reduced-order model we use the libROM library [25].

3.3 Numerical experiments

In this section, we apply the presented reduced-order model to simulate the flow past a periodically moving two-dimensional hydrofoil. First, we discuss the general setup of the problem, its discretization and numerical parameters. Following the general setup, we provide an overview of the reduced-order model's specifics and explain the metrics used for evaluation. After these preliminaries, we conduct three parameter studies, systematically varying parameters such as period, viscosity, and motion profile. This will provide a clear demonstration of the potential offered by the reduced-order model.

3

3.3.1 Problem setup

A typical isotime slice of the computational domain is given in Figure 3.2. The hydrofoil has a NACA 0012 profile with a chord denoted as c . To find a reasonable balance between artificial boundary influences and computational effort, the size of the domain is chosen to be 8 chords in the upwind and lateral directions and 8 chords in the downwind direction. The inflow from the left is a uniform flow, this velocity is denoted as U . The foil experiences a forced heave motion, with amplitude h_a .

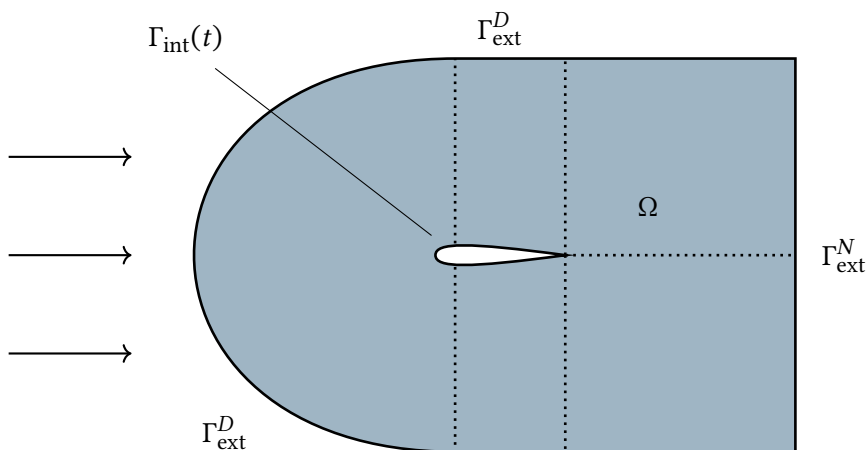


Figure 3.2: Schematic representation of the domain Ω , as an iso-time slice of P , surrounding the hydrofoil with the no-slip boundary Γ_{int} , the inflow boundary Γ_{ext}^D and the outflow boundary Γ_{ext}^N . The arrows indicate the direction of the flow. The five NURBS patches are indicated with a dotted line.

In the first two experiments, the motion is sinusoidal and given by

$$h(t) = h_a \sin\left(\frac{2\pi t}{T}\right), \quad (3.27)$$

where T is the period. To correctly categorize the motion, we introduce the Strouhal number

$$\text{St} = \frac{2 h_a}{U T}. \quad (3.28)$$

Furthermore, we will use the chord Reynolds number

$$\text{Re} = \frac{U c}{\nu}, \quad (3.29)$$

and force coefficients to non-dimensionalize the system,

$$C_x = \frac{F_x}{\frac{1}{2} \rho U^2 c}. \quad (3.30)$$

Discretization

The full-order model formulation in (3.7) is evaluated using isogeometric analysis. We discretize the domain using five second-order NURBS patches. This results in C^1 -continuity within each patch and C^0 -continuity over patch interfaces. The boundaries of the NURBS patches are indicated with the dotted lines in Figure 3.2. The patches are extruded in the time direction, resulting in 3D NURBS patches. We satisfy the time-periodic boundary condition with C^0 -continuous constraints.

The motion of the foil section is accommodated by appropriately shaping the space-time mesh a priori. This is achieved by first applying knot insertion to fit the shape of Γ_{int} to be the foil section on each time slab of P_{int} . Then, knots are inserted in the time direction to apply the prescribed motion on P_{int} . The resulting mesh contains the entire discretized space-time domain of the time-periodic problem. We refer to [50] for knot insertion and fitting algorithms.

This discretization results in 900k degrees-of-freedom per variable, making a total system size of 2.7M degrees-of-freedom. We use 49 control points in the time direction. See Appendix 3.A for details regarding the discretization choice and time slices of the mesh. Further refinement of the discretization gives only a small improvement of the solution and does not compensate for the additional computational costs.

The boundaries of the resulting discretized domain are shown in Figure 3.3. Here, one of the time-periodic boundaries is cut off, revealing the shape of P_{int} , which governs the motion of $\Gamma_{\text{int}}(t)$.

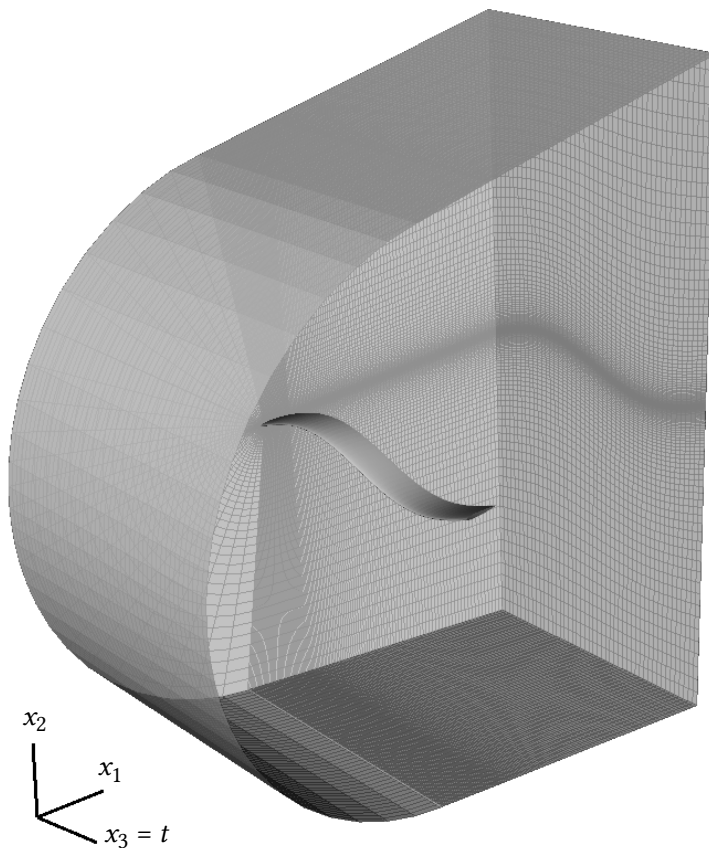


Figure 3.3: The boundaries of the resulting discretized domain. The shape of P_{int} , which governs the motion of $\Gamma_{\text{int}}(t)$, is revealed as one of the time-periodic boundaries is cut off. See Appendix 3.A for time slices of the mesh.

Numerical parameters

Due to the non-dimensional nature of the problem, the choice for freestream and chord is largely immaterial. For simplicity, we choose unity, that is $U = 1$ and $c = 1$. The time-dependent boundary velocities $\mathbf{g}_{\text{int}}(t)$ on the internal boundary are governed by the space-time mesh and are not given as an input. The velocity \mathbf{g}_{int} is computed with the derivative of the spatial coordinate \mathbf{x} to the time direction $t = x_{d+1}/s$

$$\mathbf{g}_{\text{int}} = \left. \frac{\partial \mathbf{x}}{\partial t} \right|_{\mathbf{x}_p} \quad \text{in } P_{\text{int}}, \quad (3.31)$$

where \mathbf{x}_p is a particle path on the solid of P_{int} . See Chapter 2 [88] for more details. Other relevant numerical parameters are given in Table 3.1.

Table 3.1: Numerical parameters and their corresponding values.

| Parameter | Value |
|----------------|-------|
| s | 1 |
| a | 4 |
| C_I | 36 |
| C_b | 8 |
| C_{dc} | 0.3 |
| $\Delta\theta$ | 1.0 |

For the convergence criterion, we choose an absolute tolerance of 10^{-5} for the two momentum conservation and mass conservation residuals of both the full-order and reduced-order model. For the full-order model, the residual is evaluated at the beginning of each pseudo-time step [88]. Tighter convergence criteria only result in negligible changes to the solution.

Reduced-order model

The reduced-order model as presented in (3.25) is constructed and evaluated in three stages: an offline, merge and online stage. In the offline stage, we evaluate the full-order model for 30 values of the input parameter μ , chosen with equal distance in the parameter space Θ . In the merge stage, the snapshot matrix of the time-periodic space-time solution of the full-order model is assembled and the solution basis \mathbf{V}_x is computed using a POD. In the online stage, the system in (3.25) is constructed and solved.

We compute the forces of the full-order model as introduced in Chapter 2 [88], using a space-time force extraction method inspired by the variationally consistent postprocessing method [78, 94]. For clarity, we repeat it here. The time-dependent force is given by

$$\mathbf{F}(t) = \int_{\Gamma_{\text{int}}} p\mathbf{n} - \nu\nabla\mathbf{u} \cdot \mathbf{n} + \tau_b(\mathbf{u} - \mathbf{g})d\Gamma \quad (3.32)$$

which requires a spatial integral at a fixed time level. For arbitrary space-time meshes evaluation of this integral is not trivial. We remedy this by discretizing the force in time,

$$\mathbf{F}^h(t) = \mathbf{F}_a N_a(t), \quad (3.33)$$

and project the signal as follows

$$\int_{\mathcal{J}} \mathbf{F}_a N_a N_b dt = \int_{P_{\text{int}}} (p\mathbf{n} - \nu\nabla\mathbf{u} \cdot \mathbf{n} + \tau_b(\mathbf{u} - \mathbf{g})) N_b dt, \quad (3.34)$$

which only involves integrals that are easily evaluated. Note that the last term on the right-hand side is the contribution of the weak boundary condition.

Performance metrics

We evaluate the accuracy of the reduced-order model by evaluating the normalized l_2 -norm of the error for each variable. The error is the difference between the full-order solution, ϕ_x , and the full representation of the reduced-order solution, $\tilde{\phi}_x$, over the entire space-time domain

$$\epsilon_x = \sqrt{(\tilde{\phi}_x - \phi_x) \cdot (\tilde{\phi}_x - \phi_x) / \sqrt{\phi_x \cdot \phi_x}}, \quad (3.35)$$

where x is a place holder for the different variables u_1, u_2 and p . The error is normalized with the l_2 -norm of the full-order solution of the entire space-time domain. The speed-up of the reduced-order model (ROM) over the full-order model (FOM) is defined as

$$\text{speed-up} = \frac{\text{wall-clock time FOM}}{\text{wall-clock time ROM}}. \quad (3.36)$$

The wall-clock time (elapsed real time) only includes the solve time of the non-linear system and excludes the assembly of the matrix. This ensures that the time required for assembling precomputable matrices is excluded from the wall-clock time.

We evaluate the accuracy of the computed forces \mathbf{F} using the average and root mean square error for each component. For a generic force component F we compute these as

$$\epsilon_{\text{avg}} = \frac{1}{T} \int_{\mathcal{J}} \tilde{F}^h - F^h dt = \frac{1}{n_f} \sum_{i=1}^{n_f} \tilde{F}^h(t_i) - F^h(t_i), \quad (3.37)$$

$$\epsilon_{\text{RMS}}^2 = \frac{1}{T} \int_{\mathcal{J}} (\tilde{F}^h - F^h)^2 dt = \frac{1}{n_f} \sum_{i=1}^{n_f} (\tilde{F}^h(t_i) - F^h(t_i))^2, \quad (3.38)$$

where n_f is a specified number of samples and $t_i = \frac{i}{n_f} T$. To get a more meaningful quantification of the error, the average and RMS errors are normalized with the range of the data ΔF ,

$$\epsilon_{\text{navg}} = \frac{\epsilon_{\text{avg}}}{\Delta F}, \quad (3.39)$$

$$\epsilon_{\text{nRMS}} = \frac{\epsilon_{\text{RMS}}}{\Delta F}, \quad (3.40)$$

where the range of the data is obtained using

$$\Delta F = \max_{i=1..n_f} (F^h(t_i)) - \min_{i=1..n_f} (F^h(t_i)). \quad (3.41)$$

3.3.2 Parameter studies

In this section, we evaluate three studies considering a variation in Strouhal number, Reynolds number and motion profile. For each scenario, we first discuss the general description of the problem and assess its reducibility, followed by a review of the results and the error metrics described earlier.

Strouhal number study

In this experiment, we will vary the Strouhal number and evaluate the efficacy of the reduced-order model to deal with this parameter change. The Strouhal number St is a measure of the velocity of the motion relative to the free-stream velocity. For flat objects with flapping motions, such as heaving foil sections, the range of $St = 0.1$ to $St = 0.3$ is of particular interest. Due to the interaction of the shed vortex with the foil section, it will make the transition from drag to thrust producing when St is increased in this range.

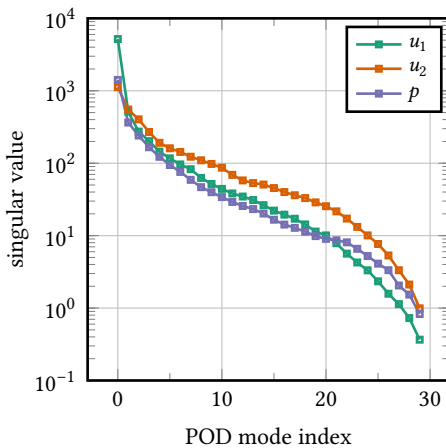
We will be looking at four different Strouhal numbers spread over the range of interest, that is

$$\text{St} \in [0.105, 0.155, 0.205, 0.255], \quad (3.42)$$

while we fix the motion amplitude $h_a/c = 0.5$. For the Reynolds number we set $\text{Re} = 800$.

To speed up the computations, we build a reduced-order model for a sinusoidal heaving foil section with a variation in Strouhal number. In the offline stage, we compute 30 equidistant snapshots in the range $0.08 \leq \text{St} \leq 0.28$. The Strouhal numbers we are interested in, given in (3.42), are not in this set. To extract an efficient basis for the reduced-order model out of the snapshots we compute the SVD of the snapshot matrix. The two most dominant modes of the basis of u_1 , u_2 and p are visualized in Appendix 3.B. The singular values σ_i of this decomposition are given in Figure 3.4.

From the steep decline in σ_i it can be concluded that the problem is suitable for reduction. Using the singular values, the missing energy fraction ϵ_{POD} for different reduced bases can be computed. The required size of the reduced basis for a given missing energy fraction ϵ_{POD} is indicated in Table 3.2.



| ϵ_{POD} | size u_1 | size u_2 | size p |
|-------------------------|------------|------------|----------|
| 10^{-3} | 7 | 20 | 13 |
| 10^{-4} | 14 | 25 | 22 |
| 10^{-5} | 20 | 27 | 26 |
| 10^{-6} | 24 | 29 | 29 |
| 0 | 30 | 30 | 30 |

Figure 3.4: Strouhal number study: Decay of singular values σ_i associated with \mathbf{V} .

Table 3.2: Strouhal number study: Basis size n_r per variable per missing energy fraction ϵ_{POD} (3.22).

For these five different reduced bases the speed-up and errors in solution and force are given in Figure 3.5. The solution error is computed as $\epsilon = \sqrt{\epsilon_{u_1}^2 + \epsilon_{u_2}^2 + \epsilon_p^2}$, using (3.35). The force errors are given by (3.37) and (3.38) and are averaged over the four Strouhal numbers. As expected the figure shows that the errors decrease if the missing energy fraction ϵ_{POD} is decreased. The speed-up also decreases but is still significant. Note that the errors of the forces converge to zero. Below $\epsilon_{\text{POD}} < 10^{-4}$ the speed-up does not further deteriorate, therefore we choose $\epsilon_{\text{POD}} = 0$ for further experiments as this gives a favourable compromise between speed-up and errors.

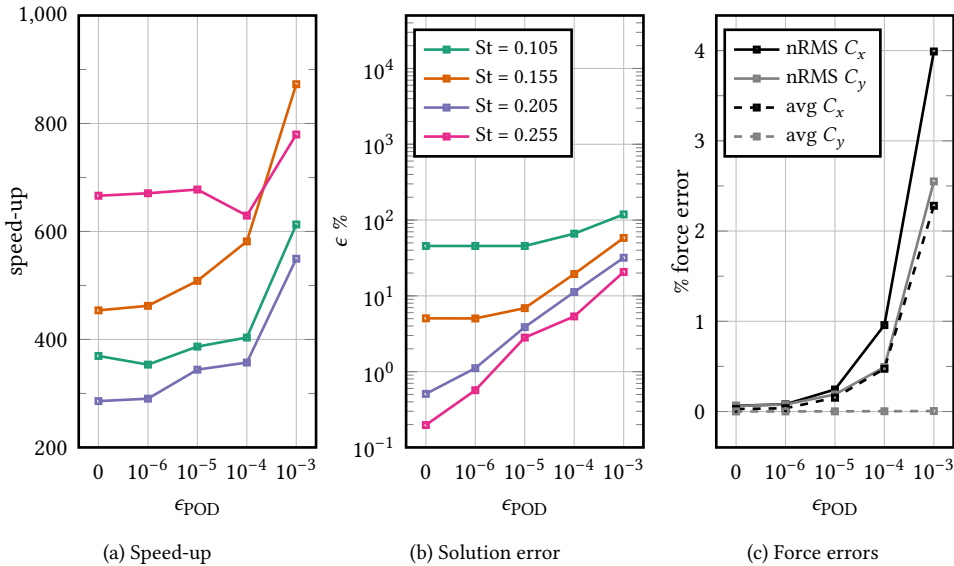


Figure 3.5: Strouhal number study: Reduced-order mode speed-up and convergence of the error as function of the missing energy fraction ϵ_{POD} as given in Table 3.2.

For higher Strouhal numbers the errors are smaller, as can be seen in Figure 3.5. The contribution of the separate variables u_1 , u_2 , and p to these errors are given in Figure 3.6. This is likely a consequence of the sampling of the parameter space used for generating the snapshots. Alternatively, instead of opting for a uniform sampling of the Strouhal number, one could have chosen a uniform sampling of

the period T , or equivalently $1/St$, which would have resulted in a higher density of samples at low Strouhal numbers. Another implementation of this experiment, with a uniform sampling of the period T , indeed showed smaller errors at low Strouhal numbers. Note that choices considering the sampling density can be avoided with the employment of an adaptive sampling method, leading to more uniform errors in the parameter space. The error for u_1 is smaller than the errors for u_2 and p . This can be explained by the normalized nature of ϵ_v . The norm of u_1 is dictated by the free stream velocity U .

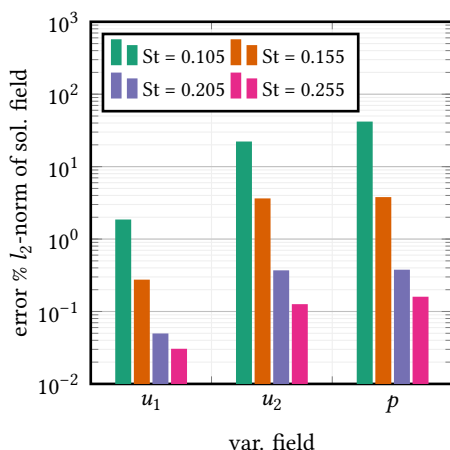


Figure 3.6: Strouhal number study: normalized l_2 -norm of the error ϵ_x (3.35) of reduced-order w.r.t. full-order model.

The computed forces of the reduced-order and full-order models are given in Figure 3.7 and Figure 3.8. The corresponding normalized RMS (3.38) and average (3.37) error are also provided. The agreement between the forces is very good. For the forces in the x_1 -direction and the x_2 -direction the errors are $< 0.2\%$. Note that the full-order and reduced-order models use different force extraction methods.

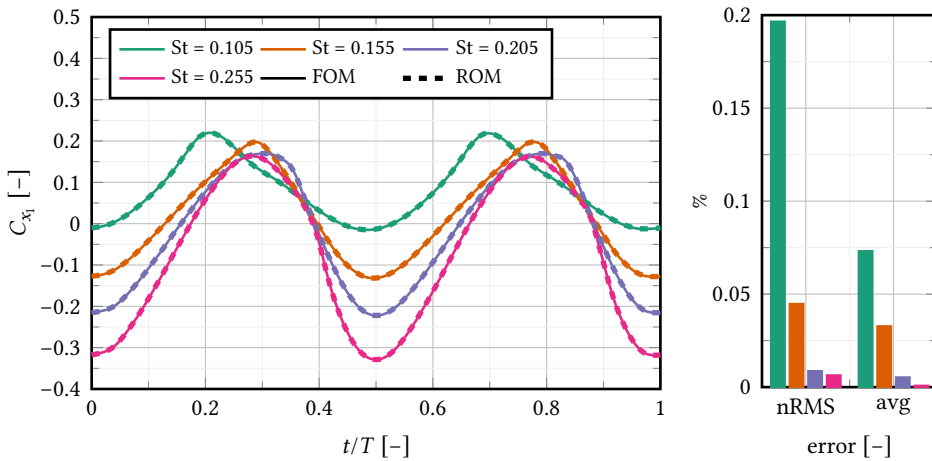


Figure 3.7: Strouhal number study: Horizontal force coefficient C_{x_1} and corresponding normalized RMS error and absolute error of the average force for reduced-order w.r.t. full-order model.

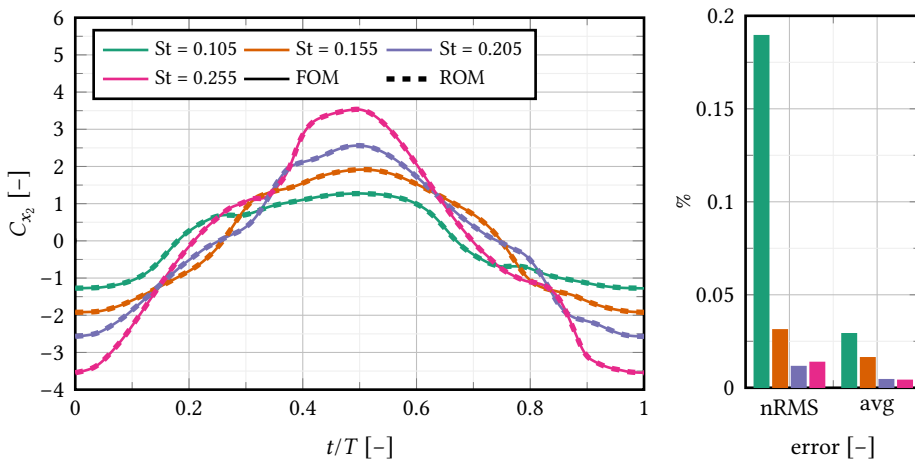


Figure 3.8: Strouhal number study: Vertical force coefficient C_{x_2} and corresponding normalized RMS error and absolute error of the average force for reduced-order w.r.t. full-order model.

Two typical velocity fields computed by the reduced-order model and full-order model, for $St = 0.105$ and $St = 0.255$, are depicted in Figure 3.9. The figure shows the agreement between the two velocity fields. Note that the wake interaction is qualitatively different. This qualitative difference is also reflected in the force signals as depicted in Figure 3.7 and Figure 3.8, particularly the force in the x_1 direction is notably different.

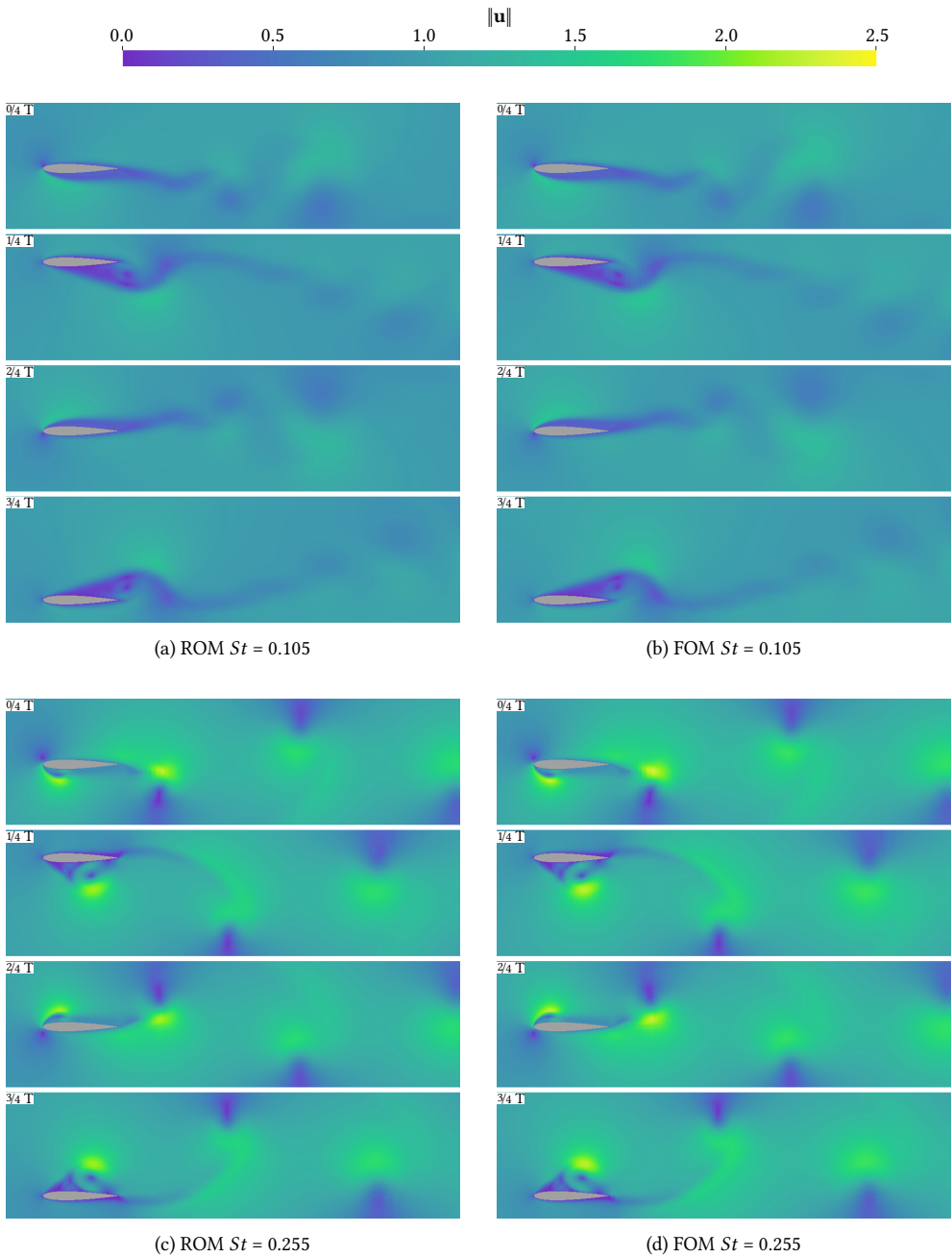


Figure 3.9: Strouhal number study: Magnitude of the velocity $\|\mathbf{u}\|$ computed by the reduced-order model (ROM) and full-order model (FOM) for $St = 0.105$ and $St = 0.255$. Visualized using VisIt [24].

Reynolds number study

The Reynolds number Re describes the ratio of inertial forces to viscous forces in fluid flow. It helps to characterize the flow regime, indicating whether it is laminar, transitional, or turbulent.

We study low Reynolds number flow with $Re < 10^3$, below the transition regime to turbulent flow. An increase in Reynolds number can be linked to either an increase in forward velocity or a decrease in viscosity. As the Reynolds number increases, we anticipate a reduction in drag forces and an increase in lift forces.

We create a reduced-order model for a sinusoidal heaving foil section with a variation in Reynolds number, $200 \leq Re \leq 800$. We choose a constant Strouhal number of $St = 0.125$ and a constant motion amplitude $h_a/c = 0.5$. Figure 3.10 shows a steep decrease of the singular values σ_i , indicating that the problem is reducible. We evaluate the reduced-order model, and the full-order model as ground truth, at

$$Re \in [275, 425, 575, 725]. \quad (3.43)$$

These Reynolds numbers do not coincide with the Reynolds numbers used to generate the snapshots.

Figure 3.11 gives the relative error (3.35) for the variable fields when comparing the reduced-order model with the full-order model. The errors are the smallest for

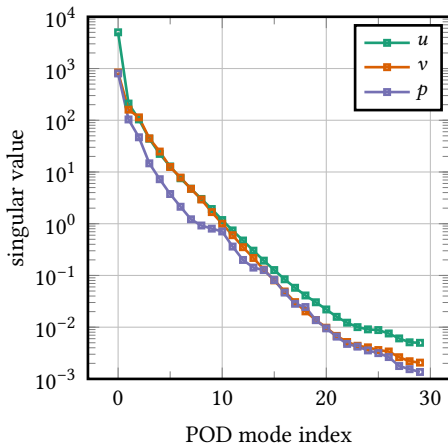


Figure 3.10: Decay of singular values σ_i associated with \mathbf{V} for the Reynolds number study.

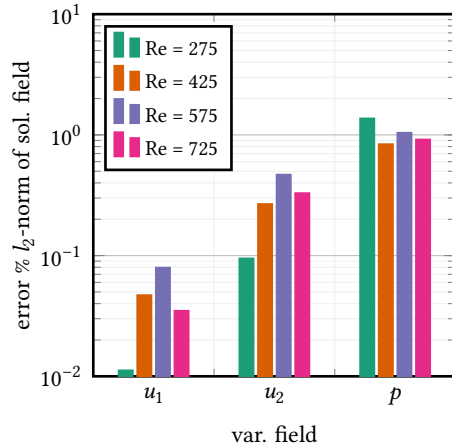


Figure 3.11: l_2 -norm of the error ϵ_x (3.35) of reduced-order w.r.t. full-order model normalized with the l_2 -norm of the solution field for the Reynolds number study.

the u_1 -solution field. The errors for the p -solution field are the largest. All errors are $\leq \mathcal{O}(1\%)$.

Figure 3.12 and Figure 3.13 show the agreement between the computed forces of the full-order and reduced-order models. The normalized root mean square error (3.38) and the normalized error of the average (3.37) are $< 0.08\%$ and $< 0.05\%$ for C_{x_1} and C_{x_2} respectively.

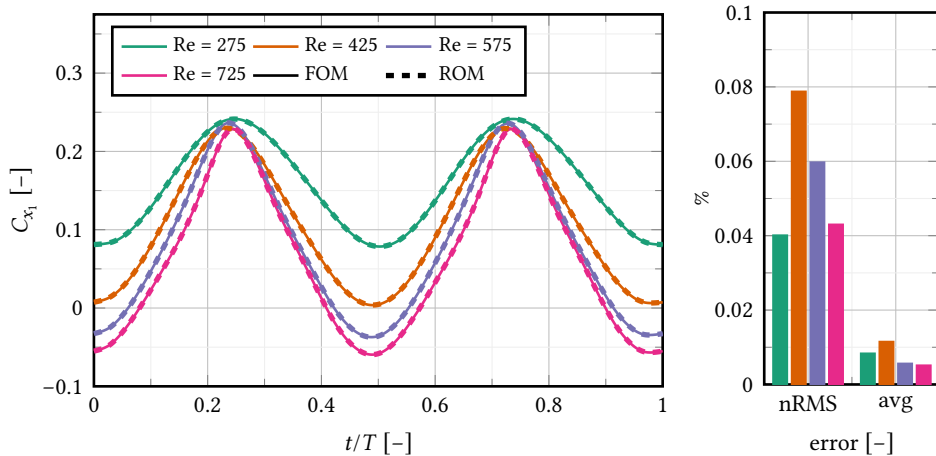


Figure 3.12: Reynolds number study: Horizontal force coefficient C_{x_1} and corresponding normalized RMS error and absolute error of the average force for reduced-order w.r.t. full-order model.

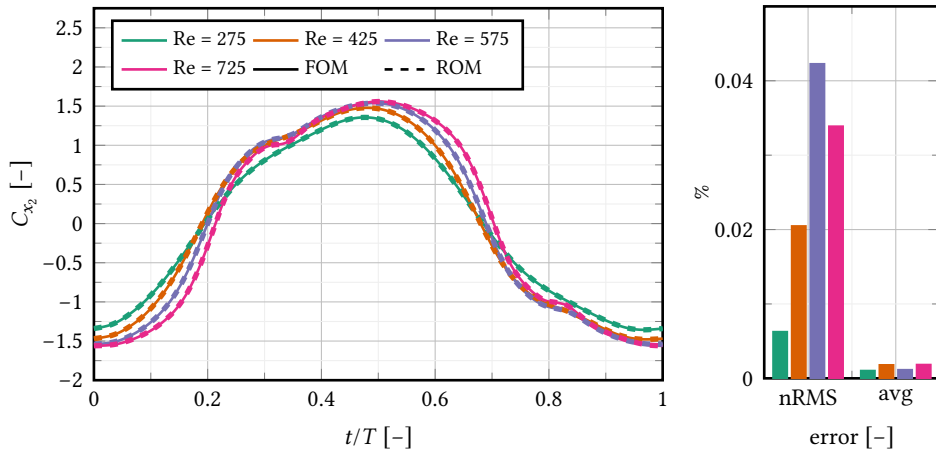


Figure 3.13: Reynolds number study: Vertical force coefficient C_{x_2} and corresponding normalized RMS error and absolute error of the average force for reduced-order w.r.t. full-order model.

Motion profile study

The motion profile significantly influences thrust production in a flapping wing. An optimized motion profile can enhance aerodynamic efficiency by maximizing lift and minimizing drag, ultimately leading to more effective thrust production. We study a group of non-sinusoidal motion profiles described with

$$h(t) = h_a \sin(\omega t + \phi(t),) \quad (3.44a)$$

$$\phi(t) = \phi_a \cos(\omega t). \quad (3.44b)$$

The time trace of this motion is given in Figure 3.14.

The time-dependent phase-shift modulation $\phi(t)$ is time-periodic, resulting in a time-periodic heave. As ϕ_a increases, the original sinusoidal motion is distorted in an unsymmetric way. At a positive heave, the motion slows down, while at a negative heave, the motion speeds up. This results in an uneven dwell time in the upper and lower parts of the stroke.

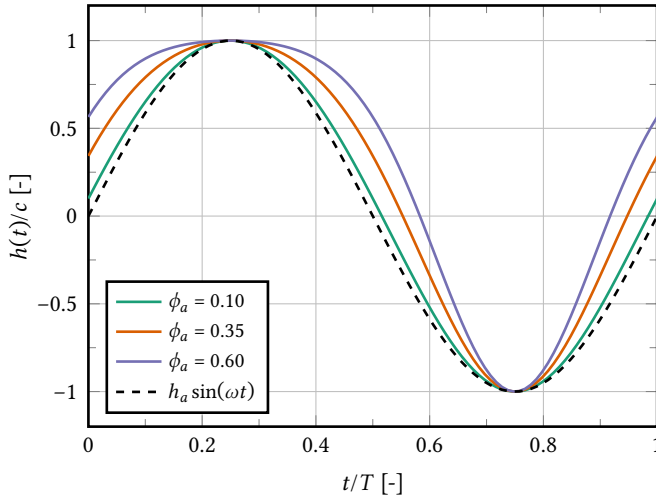


Figure 3.14: Motion profile study: Non-sinusoidal heave function as in (3.44).

We create a reduced-order model for a variation of the phase amplitude $0.1 \leq \phi_a \leq 0.6$. The other parameters are chosen similarly to the previous test cases, that is: the Reynolds number is $\text{Re} = 800$, the Strouhal number is $\text{St} = 0.125$ and a motion amplitude of $h_a/c = 0.5$.

The singular values σ_i of the snapshot matrix are given in Figure 3.15. The steep decrease in the singular values indicates that the problem is amenable to model-order reduction. We assess the reduced-order model at

$$\phi_a \in [0.1625, 0.2875, 0.4125, 0.5375]. \quad (3.45)$$

These values do not match the amplitudes used for generating the snapshots. We compare the reduced-order model against the full-order model, which is considered as ground truth.

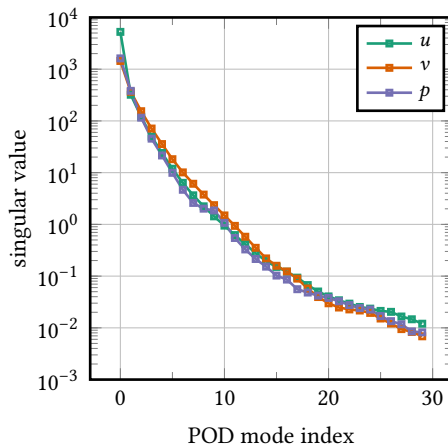


Figure 3.15: Motion profile study: Decay of singular values σ_i associated with \mathbf{V} .

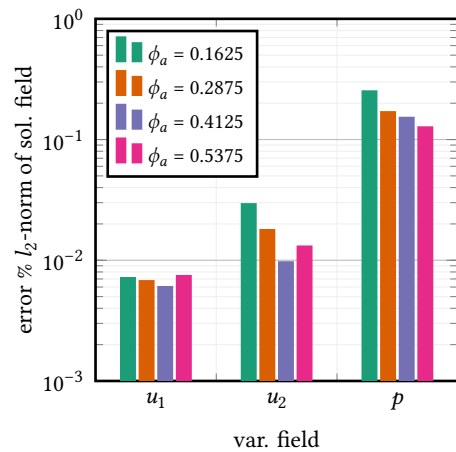


Figure 3.16: Motion profile study: l_2 -norm of the error ϵ_x (3.35) of reduced-order w.r.t. full-order model normalized with the l_2 -norm of the solution field.

Figure 3.16 shows similar trends when comparing the relative error (3.35) of the variable fields for the reduced-order model versus the full-order model as the previous cases. The errors are the smallest for u_1 and the largest for p . All errors are $\leq \mathcal{O}(0.1\%)$.

Figures 3.17 and 3.18 show very good agreement between the force coefficients computed by the full-order and reduced-order models. The normalized root mean square error (3.38) and the normalized error of the average (3.37) are $< 0.01\%$ for C_{x_1} and $< 0.005\%$ for C_{x_2} .

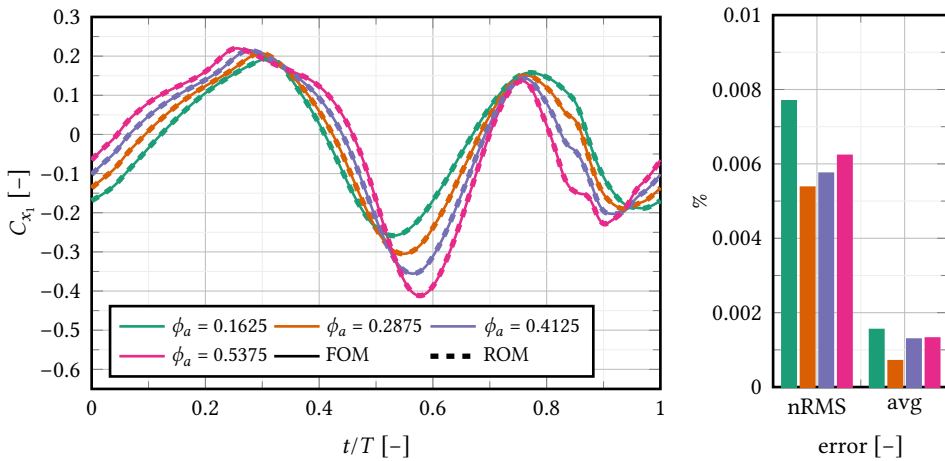


Figure 3.17: Motion profile study: Horizontal force coefficient C_{x_1} and corresponding normalized RMS error and absolute error of the average force for reduced-order w.r.t. full-order model.

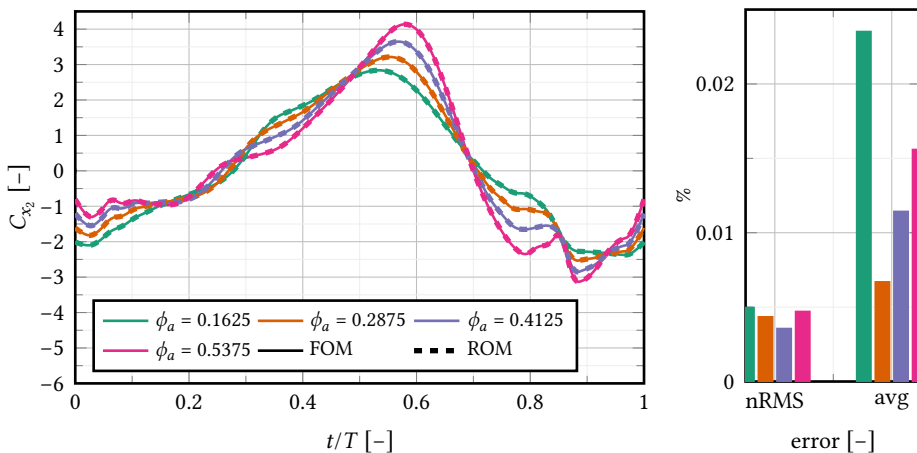


Figure 3.18: Motion profile study: Horizontal force coefficient C_{x_2} and corresponding normalized RMS error and absolute error of the average force for reduced-order w.r.t. full-order model.

3.4 Conclusions

We have successfully implemented a time-periodic reduced-order model. We confirmed the favourable performance of the reduced-order model on the problem of a moving hydrofoil, where we varied the Strouhal number, Reynolds number and heave motion profile.

The computed solution fields of the reduced-order model and full-order model show good agreement. The same is true for the postprocessed forces. While reducing the dimension of the problem from $\mathcal{O}(10^6)$ to $\mathcal{O}(10^2)$ the errors in the force are less than 0.2% for drag and lift. This makes the reduced-order model suitable for computations of a wide variety of time-periodic flows.

The reduced-order model behaved predictably as increasing the size of the reduced basis caused the errors to converge to zero. The reduced-order model offers a speed-up of $\mathcal{O}(10^2)$ - $\mathcal{O}(10^3)$ over the full-order model, depending on the basis size. Higher speed-ups are likely possible when appropriate non-linear reduction techniques, such as hyper-reduction, would be adopted.

Looking forward, there are several interesting avenues for future work. First, extending the model to three spatial dimensions would significantly enhance its applicability. Second, additional verification for higher Reynolds numbers makes the model suitable for more industrial applications. Finally, applying the model to industrial contexts, such as optimizing the performance and layout of wind farms or ship propellers, provides an opportunity to bridge the gap between the ideas in this work and practical solutions.

3.A Temporal and spatial discretization

The spatial convergence for a steady-state case of a foil section at an angle of attack of 3° is given in Figure 3.19. The convergence orders of C_{x_1} and C_{x_2} are 1.3 and 1.4, respectively. A spatial discretization of $h/h_0 = 0.5$ was chosen, as it exhibited errors of 3.0% and 1.1% with the Richardson extrapolated results, offering a balance between computational costs and discretization error.

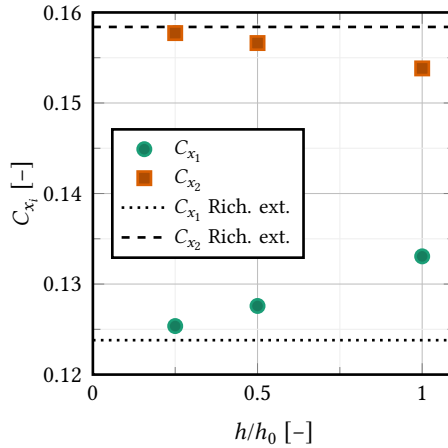


Figure 3.19: Numerical results and Richardson extrapolation of the steady-state force coefficients C_{x_i} . The order of convergence is 1.30 and 1.35 for directions x_1 and x_2 respectively.

In the spatial discretization with $h/h_0 = 0.5$, the patches are refined to 68 control points between the foil section and the inflow boundary, 62 control points over the length of the foil section and 78 control points between the foil section and the out-flow boundary. The spacing of the control points is similar as in Chapter 2 [88]. The resulting spatial discretization is visualised in Figure 3.20.

The temporal domain is discretized with 49 control points. For a further refinement, the added computational costs do not balance the reduction in error on a pure heaving test case.

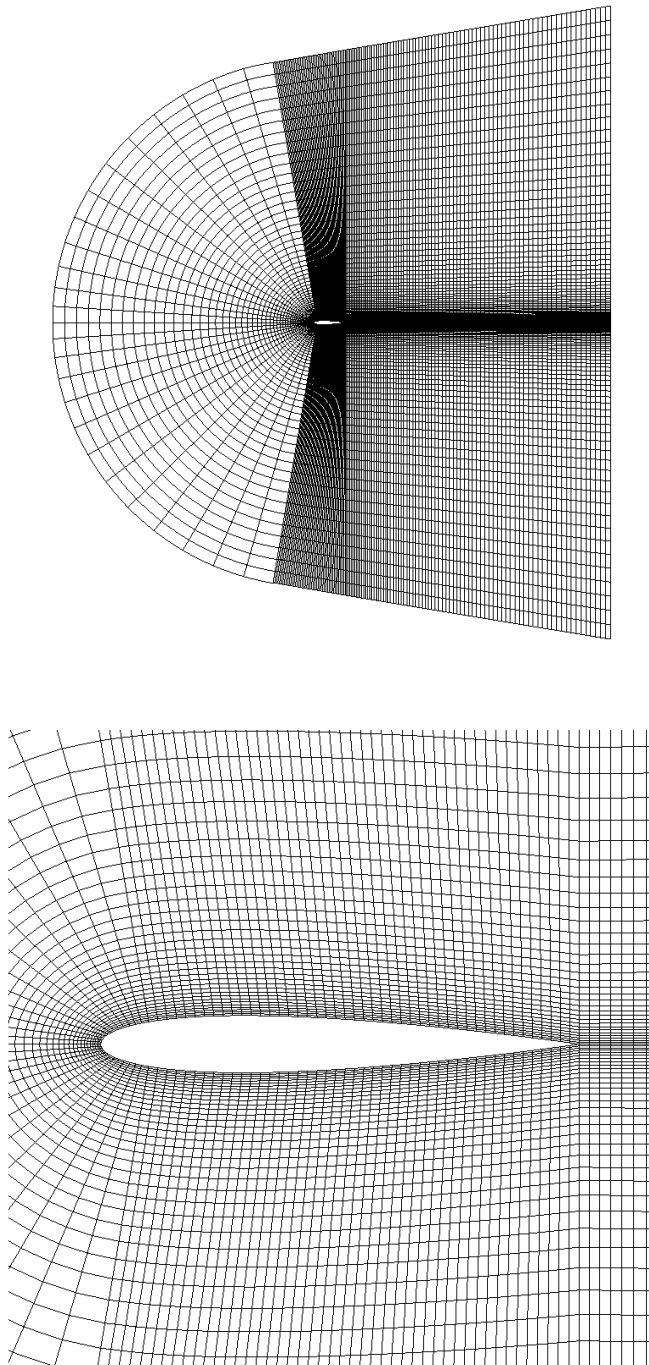


Figure 3.20: Slices of the space-time mesh, showing the discretization of the spatial domain at $t = 0$. Visualized using VisIt [24].

3.B Visualization of the basis

Figures 3.21, 3.22 and 3.23 visualizes four slices of the shapes of the two most dominant modes of the time-periodic basis. The slices are taken at $t = 0$, $t = \frac{1}{4}T$, $t = \frac{2}{4}T$, $t = \frac{3}{4}T$ for u_1 , u_2 and p .

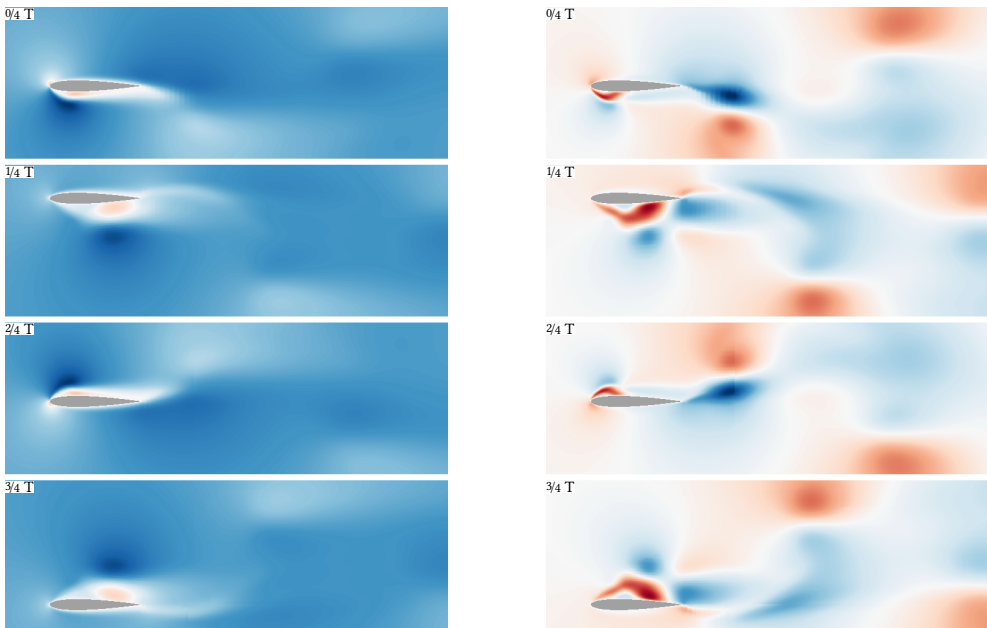


Figure 3.21: Strouhal number study: slices of mode 1 (a) and mode 2 (b) of the basis for u_1 at $t = 0$, $t = \frac{1}{4}T$, $t = \frac{2}{4}T$, $t = \frac{3}{4}T$. Visualized using VisIt [24].

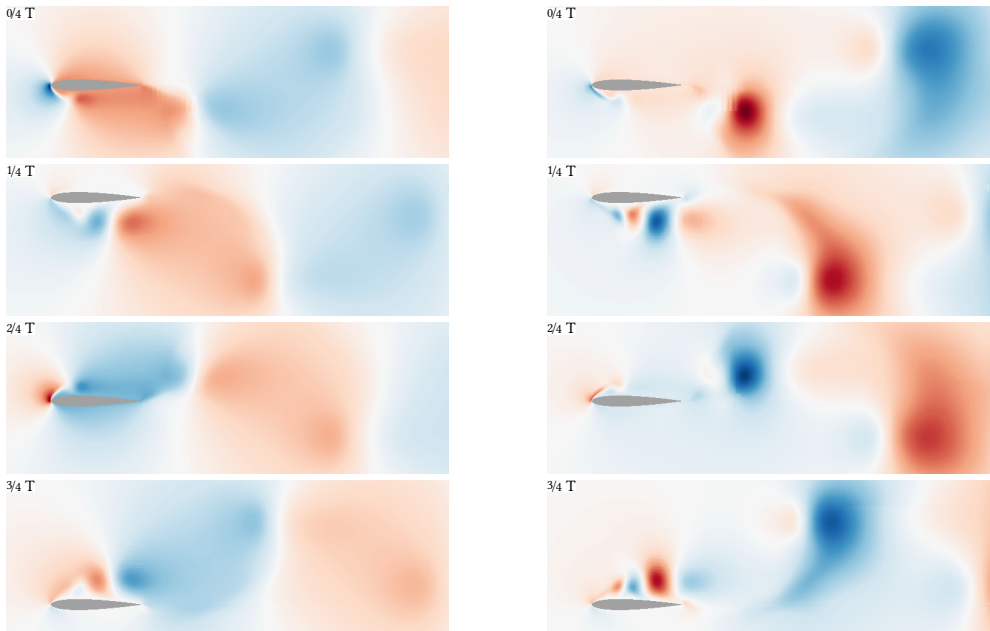


Figure 3.22: Strouhal number study: slices of mode 1 (a) and mode 2 (b) of the basis for u_2 at $t = 0$, $t = 1/4 T$, $t = 2/4 T$, $t = 3/4 T$. Visualized using VisIt [24].

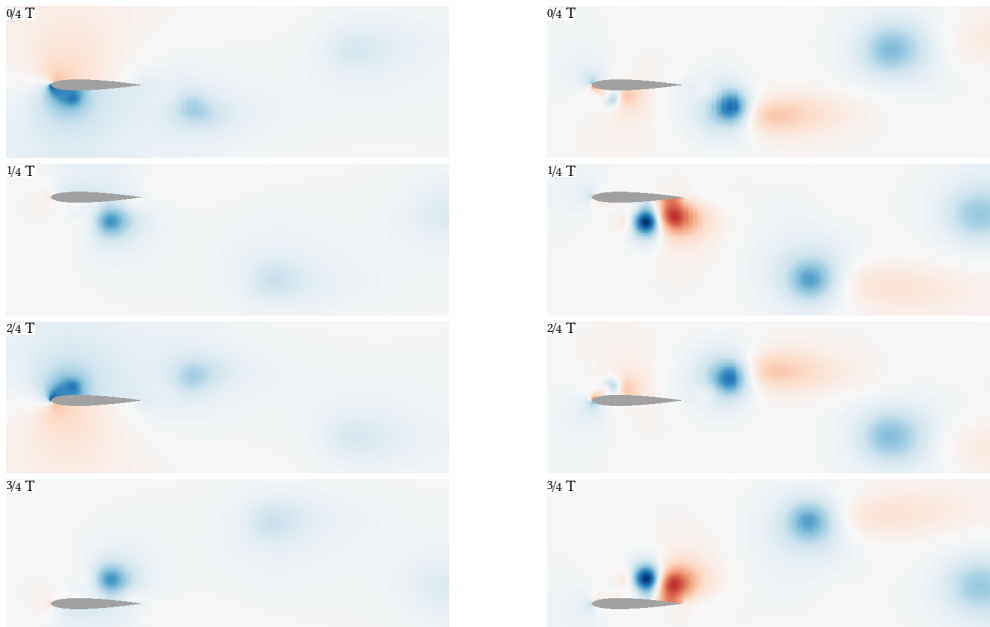


Figure 3.23: Strouhal number study: slices of mode 1 (a) and mode 2 (b) of the basis for p at $t = 0$, $t = 1/4 T$, $t = 2/4 T$, $t = 3/4 T$. Visualized using VisIt [24].

4

Considerations on a hyper-reduced model of time-periodic flows

4

A space-time discretization approach can exploit the time-periodic nature of flow problems. By converting the initial value problem into a boundary value problem with a time-periodic boundary condition it enables simple projection-based reduced-order model techniques. However, the non-linear nature of the Navier–Stokes equations creates a computational bottleneck in the reduced-order model. We explore hyper-reduction techniques to mitigate these challenges. We focus on empirical interpolation methods, which have shown promise in reducing the complexity of non-linear operators. While these methods are effective, their success is limited due to issues such as the slow decay of the Kolmogorov n -width and stability concerns. We evaluate the hyper-reduced model in two numerical experiments: steady flow past a foil section and time-periodic flow past a periodically heaving foil section. The model performed well for the experiment with steady flow, with force and solution errors ranging from $\mathcal{O}(0.01\% - 10\%)$, depending on the sampling method. The hyper-reduced model achieves a speed-up of $\mathcal{O}(10^5)$ compared to the full-order model, and $\mathcal{O}(10^3)$ compared to the reduced-order model. This enables real-time computations. However, the hyper-reduced model could not provide a solution for the time-periodic flow experiment, possibly due to the aforementioned challenges.

4.1 Introduction

Finding a time-periodic solution for flow past a periodically moving object using the Navier–Stokes equation is computationally costly, requiring integrating an initial condition over multiple periods until convergence. We treat space and time analogously in a space-time discretization. Then, we can take advantage of the time-periodic nature of the problem by applying a time-periodic boundary condition [53, 88, 109, 123]. The original initial value problem is converted into a boundary value problem avoiding lengthy time integration and allowing efficient evaluation of time-periodic problems. The conversion to a boundary value problem also opens the door for simple projection-based model reduction techniques with a great reduction of the number of solution variables. Such reduced-order models allow for speed-ups up to $\mathcal{O}(10^3)$ of the original full-order model [89].

The Navier-Stokes equations are inherently non-linear due to its convective term. Furthermore, if the full-order model incorporates stabilization, the additional stabilization terms also contribute to this non-linearity. This non-linearity requires a repeated evaluation of the non-linear operator in the reduced-order model, with a complexity that scales with the size of the full-order model, inducing a major computational bottleneck in the evaluation of the reduced-order model. In this chapter, we explore the application of non-linear reduction techniques in the time-periodic reduced-order model, allowing for much greater speed-ups than conventional reduced-order models.

Non-linear reduction techniques help alleviate the computational bottlenecks related to constructing the non-linear operator in reduced-order models. The goal is to evaluate this operator with a complexity independent of the full-order model's size. For a comprehensive overview of non-linear projection-based reduction methods, we refer to [45]. Here, we provide a brief introduction to the available methods.

We start with the the Gappy-POD method. This method is initially developed for handling sparse data in image reconstruction [43] and has been a pioneering technique in the field. It has inspired various approaches in model order reduction, including the empirical interpolation method (EIM) [9], the best point interpolation method [102], and the missing point estimation approach [4]. Among these, the empirical interpolation method, which approximates the non-linear operator using empirically derived basis functions, led to the development of the widely-used discrete empirical interpolation method (DEIM) [23] and the Gauss-Newton with approximated tensors method [22]. The discrete empirical interpolation method enables

fast evaluation of the non-linear operator by projecting it onto a discrete basis and evaluating it using only a small number of indices. The Gauss-Newton with approximated tensors method works similarly but has a Petrov-Galerkin approach.

In these methods, the key to reducing the complexity of the non-linear operator lies in identifying a sampling operator that selects the specific indices that can be used to approximate it best. The sampling points can be determined in various ways. The original DEIM method uses a greedy algorithm to select indices of the non-linear operator by sequentially identifying maxima in the basis. Alternatively, Q-DEIM determines sampling points through the pivot locations in a QR factorization with column pivoting [35]. This method is independent of the basis ordering, unlike DEIM. Both DEIM and Q-DEIM aim to maximize the smallest singular values of the projection operator. A more recent method, S-OPT, identifies sampling points by maximizing the product of all singular values and enhancing the orthogonality of the sampling operator's columns [81].

In this work, we use the class of empirical interpolation hyper-reduction methods as they are applied successfully in reduced-order models for flow problems, see for instance [19], and fit well in the existing framework of the reduced-order model introduced in Chapter 3 [89]. However, we would like to briefly touch upon two recent developments. A promising avenue is the empirical quadrature procedure, which uses sparse empirical quadrature rules for rapid approximation of a non-linear operator [146]. Also, an important development is the introduction of neural-network-based reduced-order models such as [72, 84, 118]. This class of reduced-order models achieves a considerable speed-up with a low-dimensional solution representation.

These hyper-reduction methods introduce an additional approximation to the original problem, which in turn induces an error and presents certain challenges. The linear approximation is often associated with a slow decay of the Kolmogorov n -width, implying that the approximation error exhibits a gradual decay while increasing the dimensionality of the subspace. As a result, not all problems are amenable to hyper-reduction and achieving a satisfactory approximation may necessitate a large subspace dimension [45]. Furthermore, the linear approximation may affect the system stability, requiring hyper-reduced models to be finely tuned [19]. These models may fail to converge or yield an accurate solution.

In this chapter, we begin by introducing the time-periodic problem and the hyper-reduced system of equations. We use an isogeometric analysis discretization for the full-order model and explain how hyper-reduction is applied to it. Fol-

lowing this, we implement the hyper-reduced model and analyze two numerical experiments. First, we verify the implementation of the hyper-reduced model with a basic test case of steady two-dimensional flow past a foil section with a variation of the Reynolds number. We use this case to evaluate the performance of the hyper-reduced model and show its potential. Second, we study the ability of the hyper-reduced model to analyze time-periodic flow. This experiment considers two-dimensional flow past a heaving foil section.

4.2 Hyper-reduction using empirical interpolation methods

We first consider the Navier-Stokes equations for time-periodic flow

$$\partial_t \mathbf{u} + \mathbf{u} \cdot \nabla \mathbf{u} + \nabla p - \nu \nabla^2 \mathbf{u} = \mathbf{f} \quad \text{in } Q, \quad (4.1a)$$

$$\nabla \cdot \mathbf{u} = 0 \quad \text{in } Q, \quad (4.1b)$$

$$\mathbf{u} = \mathbf{g}_{\text{int}} \quad \text{in } P_{\text{int}}, \quad (4.1c)$$

$$\mathbf{u} = \mathbf{g}_{\text{ext}} \quad \text{in } P_{\text{ext}}^D, \quad (4.1d)$$

$$-p \mathbf{n} + \nu \nabla \mathbf{u} \cdot \mathbf{n} + u_n^- \mathbf{u} = \mathbf{0} \quad \text{in } P_{\text{ext}}^N, \quad (4.1e)$$

$$\mathbf{u}(\cdot, 0) = \mathbf{u}(\cdot, T) \quad \text{in } \Omega, \quad (4.1f)$$

where Q denotes the space-time domain, P_{int} the internal no-slip boundary, P_{ext}^D the inflow boundary and P_{ext}^N the outflow boundary. The kinematic viscosity is represented by ν , \mathbf{f} denotes an external force, and \mathbf{g}_{int} and \mathbf{g}_{ext} are the prescribed velocities on the interior and exterior boundaries, respectively. Note that using (4.1f), instead of an initial condition, transforms the time-dependent problem into a boundary value problem. The space-time domain is Q an extrusion of the spatial domain Ω in time-direction. The spatial domain Ω , with boundary Γ , is depicted in Figure 4.1.

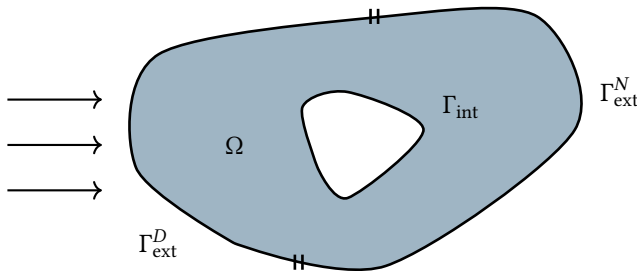


Figure 4.1: The spatial domain with its boundaries and inflow on the left.

The Navier-Stokes equations for steady flow can be derived by dropping the time derivative in (4.1a) and the time periodicity boundary condition in (4.1f). The following derivation leads to a similar result whether we consider the Navier-Stokes equations for steady or periodic flow.

We discretize the boundary value problem in (4.1) using isogeometric analysis as it enables a high-continuity solution. We find the system of equations of the full-order model

$$\begin{bmatrix} \mathbf{A}_{u_1 u_1} & \mathbf{A}_{u_1 u_2} & \mathbf{A}_{u_1 p} \\ \mathbf{A}_{u_2 u_1} & \mathbf{A}_{u_2 u_2} & \mathbf{A}_{u_2 p} \\ \mathbf{A}_{p u_1} & \mathbf{A}_{p u_2} & \mathbf{A}_{p p} \end{bmatrix} \begin{bmatrix} \boldsymbol{\phi}_{u_1} \\ \boldsymbol{\phi}_{u_2} \\ \boldsymbol{\phi}_p \end{bmatrix} + \begin{bmatrix} \mathbf{h}_{u_1}(\boldsymbol{\phi}_{u_1}, \boldsymbol{\phi}_{u_2}, \boldsymbol{\phi}_p) \\ \mathbf{h}_{u_2}(\boldsymbol{\phi}_{u_1}, \boldsymbol{\phi}_{u_2}, \boldsymbol{\phi}_p) \\ \mathbf{h}_p(\boldsymbol{\phi}_{u_1}, \boldsymbol{\phi}_{u_2}, \boldsymbol{\phi}_p) \end{bmatrix} = - \begin{bmatrix} \mathbf{b}_{u_1} \\ \mathbf{b}_{u_2} \\ \mathbf{b}_p \end{bmatrix}. \quad (4.2)$$

where \mathbf{A}_{xy} represents the mass matrix, \mathbf{h}_x the non-linear contributions and \mathbf{b}_x the right hand side. Also, each solution vector $\boldsymbol{\phi}_x$ is attributed a size n_f . The matrices \mathbf{A}_{xy} and vectors \mathbf{h}_x include the time-dependent contributions.

The system of equations in Equation (4.2) involves a large number of variables, making it computationally expensive to solve. To reduce this cost, we seek a reduced system of equations with a much smaller number of variables, that can approximate the solution of the full-order model more efficiently. For this purpose, we apply a Galerkin-POD reduced-order model, which significantly lowers the computational burden while retaining the essential features of the original system.

We first approximate the full-order model solution with

$$\boldsymbol{\phi}_x \approx \tilde{\boldsymbol{\phi}}_x = \mathbf{V}_x \hat{\boldsymbol{\phi}}_x. \quad (4.3)$$

to reduce the number of variables. Here, each reduced-order model solution variable vector $\hat{\boldsymbol{\phi}}_x$ is attributed a size n_r . The size of $\hat{\boldsymbol{\phi}}_x$ is much smaller than that of $\boldsymbol{\phi}_x$, such that $n_r \ll n_f$. We use a basis \mathbf{V}_x for each variable separately. The basis is constructed using a discrete Proper Orthogonal Decomposition (POD), as it is an optimal basis decomposition. It consists of a singular value decomposition of a snapshot matrix \mathbf{X}_ϕ [90]

$$\mathbf{X}_\phi = \boldsymbol{\Phi} \boldsymbol{\Sigma} \boldsymbol{\Psi}^T. \quad (4.4)$$

The matrix $\boldsymbol{\Phi}$ contains the POD modes (left singular vectors), $\boldsymbol{\Psi}$ gives the right singular vectors and $\boldsymbol{\Sigma}$ gives the singular values in the diagonal. The snapshot matrix \mathbf{X}_ϕ contains m full-order space-time solutions in its columns. We fill the snapshot matrix using space-time solutions obtained using specific input parameters μ , being selected samples from the broader parameter space Θ .

The singular values are arranged in ascending order, with $\sigma_i < \sigma_{i+1} < \sigma_m$, reflecting the significance of the corresponding modes. We determine the basis \mathbf{V} by selecting the first n_r columns of Φ , based on a fraction of the missing energy in the basis

$$\epsilon_{\text{POD}} = \frac{\sum_i^{n_r} \sigma_i}{\sum_i^m \sigma_i}. \quad (4.5)$$

This approach allows for the selection of a basis size that meets the desired information requirements of the basis.

We perform a Galerkin projection on (4.2) and use (4.3) to get the reduced system of equations

$$\begin{aligned} \begin{bmatrix} \mathbf{V}_{u_1} \\ \mathbf{V}_{u_2} \\ \mathbf{V}_p \end{bmatrix}^T \begin{bmatrix} \mathbf{A}_{u_1 u_1} & \mathbf{A}_{u_1 u_2} & \mathbf{A}_{u_1 p} \\ \mathbf{A}_{u_2 u_1} & \mathbf{A}_{u_2 u_2} & \mathbf{A}_{u_2 p} \\ \mathbf{A}_{p u_1} & \mathbf{A}_{p u_2} & \mathbf{A}_{p p} \end{bmatrix} \begin{bmatrix} \mathbf{V}_{u_1} \phi_{u_1} \\ \mathbf{V}_{u_2} \phi_{u_2} \\ \mathbf{V}_p \phi_p \end{bmatrix} \\ + \begin{bmatrix} \mathbf{V}_{u_1} \\ \mathbf{V}_{u_2} \\ \mathbf{V}_p \end{bmatrix}^T \begin{bmatrix} \mathbf{h}_{u_1}(\mathbf{V}_{u_1} \phi_{u_1}, \mathbf{V}_{u_2} \phi_{u_2}, \mathbf{V}_p \phi_p) \\ \mathbf{h}_{u_2}(\mathbf{V}_{u_1} \phi_{u_1}, \mathbf{V}_{u_2} \phi_{u_2}, \mathbf{V}_p \phi_p) \\ \mathbf{h}_p(\mathbf{V}_{u_1} \phi_{u_1}, \mathbf{V}_{u_2} \phi_{u_2}, \mathbf{V}_p \phi_p) \end{bmatrix} = - \begin{bmatrix} \mathbf{V}_{u_1} \\ \mathbf{V}_{u_2} \\ \mathbf{V}_p \end{bmatrix}^T \begin{bmatrix} \mathbf{b}_{u_1} \\ \mathbf{b}_{u_2} \\ \mathbf{b}_p \end{bmatrix}, \end{aligned} \quad (4.6)$$

which can be rewritten with denser notation as

$$\begin{bmatrix} \hat{\mathbf{A}}_{u_1 u_1} & \hat{\mathbf{A}}_{u_1 u_2} & \hat{\mathbf{A}}_{u_1 p} \\ \hat{\mathbf{A}}_{u_2 u_1} & \hat{\mathbf{A}}_{u_2 u_2} & \hat{\mathbf{A}}_{u_2 p} \\ \hat{\mathbf{A}}_{p u_1} & \hat{\mathbf{A}}_{p u_2} & \hat{\mathbf{A}}_{p p} \end{bmatrix} \begin{bmatrix} \hat{\phi}_{u_1} \\ \hat{\phi}_{u_2} \\ \hat{\phi}_p \end{bmatrix} + \begin{bmatrix} \hat{\mathbf{h}}_{u_1}(\mathbf{V}_{u_1} \phi_{u_1}, \mathbf{V}_{u_2} \phi_{u_2}, \mathbf{V}_p \phi_p) \\ \hat{\mathbf{h}}_{u_2}(\mathbf{V}_{u_1} \phi_{u_1}, \mathbf{V}_{u_2} \phi_{u_2}, \mathbf{V}_p \phi_p) \\ \hat{\mathbf{h}}_p(\mathbf{V}_{u_1} \phi_{u_1}, \mathbf{V}_{u_2} \phi_{u_2}, \mathbf{V}_p \phi_p) \end{bmatrix} = - \begin{bmatrix} \hat{\mathbf{b}}_{u_1} \\ \hat{\mathbf{b}}_{u_2} \\ \hat{\mathbf{b}}_p \end{bmatrix}, \quad (4.7)$$

using

$$\hat{\mathbf{A}}_{xy} = \mathbf{V}_x^T \mathbf{A}_{xy} \mathbf{V}_y^T, \quad (4.8a)$$

$$\hat{\mathbf{h}}_x(\cdot) = \mathbf{V}_x^T \mathbf{h}_x(\cdot), \quad (4.8b)$$

$$\hat{\mathbf{b}}_x = \mathbf{V}_x^T \mathbf{b}_x. \quad (4.8c)$$

The place-holders x and y represent u_1 , u_2 or p respectively. \mathbf{A}_{xy} are the blocks of the stiffness matrix and \mathbf{h}_x are the blocks of the non-linear contribution respectively. We refer to this model as the reduced model.

Evaluating the non-linear operators $\hat{\mathbf{h}}_x(\cdot)$ in (4.7) remains dependent of the size of the full-order model n_f . For each evaluation, the first step is to compute ϕ_x using (4.3), to determine \mathbf{h}_x , both of which are operations that depend on size n_f . Following this, the result is projected onto the basis \mathbf{V}_x to obtain $\hat{\mathbf{h}}_x(\cdot)$. The non-linear terms are hyper-reduced to address this bottleneck.

We adopt the group of empirical interpolation methods as the hyper-reduction technique. Here, the range of the non-linear operator is approximated by restricting the output in the subspace spanned by n_{hr} columns in the basis $\mathbf{U} = \{\mathbf{u}_1, \dots, \mathbf{u}_{n_{hr}}\}$,

$$\mathbf{h}_x(\mathbf{V}_x \hat{\boldsymbol{\phi}}_x) \approx \mathbf{U}_x \mathbf{c}_x, \quad (4.9)$$

with \mathbf{c}_x being a coefficient vector. We find the non-linear basis \mathbf{U}_x by applying a discrete proper orthogonal decomposition (4.4) on a snapshot matrix \mathbf{X}_h with samples of $\mathbf{h}_x(\boldsymbol{\phi}_x)$ for converged $\boldsymbol{\phi}_x$ in (4.2) in its columns. The snapshot matrix \mathbf{X}_h contains samples for same the set of input parameters μ as for \mathbf{X}_ϕ .

In (4.9) we introduce new variables \mathbf{c}_x , that need to be solved. To approximate \mathbf{c}_x , we use a sampling operator. Specifically, we introduce a coarse sampling operator \mathbf{P}_x which is a matrix composed of n_{hr} selected columns from the identity matrix of size $n_f \times n_f$. This operator is used to sample both sides of (4.9),

$$\mathbf{P}_x^T \mathbf{h}_x(\mathbf{V}_x \hat{\boldsymbol{\phi}}_x) \approx \mathbf{P}_x^T \mathbf{U}_x \mathbf{c}_x. \quad (4.10)$$

We can now easily approximate \mathbf{c}_x by multiplying both sides with $(\mathbf{P}_x^T \mathbf{U}_x)^{-1}$. We find

$$\mathbf{c}_x \approx (\mathbf{P}_x^T \mathbf{U}_x)^{-1} \mathbf{P}_x^T \mathbf{h}_x(\mathbf{V}_x \hat{\boldsymbol{\phi}}_x). \quad (4.11)$$

The non-linear operator of the reduced-order model $\hat{\mathbf{h}}_x(\mathbf{V}_x \hat{\boldsymbol{\phi}})$ can be approximated, independent of an evaluation of size n_f , with

$$\begin{aligned} \hat{\mathbf{h}}_x(\mathbf{V}_x \hat{\boldsymbol{\phi}}) &= \mathbf{V}_x^T \mathbf{h}_x(\mathbf{V}_x \hat{\boldsymbol{\phi}}_x) \\ &\approx \mathbf{V}_x^T \mathbf{U}_x \mathbf{c}_x \\ &\approx \hat{\mathbf{h}}_{hr,x} = \mathbf{V}_x^T \mathbf{U}_x (\mathbf{P}_x^T \mathbf{U}_x)^{-1} \mathbf{P}_x^T \mathbf{h}_x(\mathbf{V}_x \hat{\boldsymbol{\phi}}_x). \end{aligned} \quad (4.12)$$

The sampling operator \mathbf{P}_x strategically selects a set of indices leading to an accurate approximation of the non-linear operator. The matrix $\mathbf{V}_x^T \mathbf{U}_x (\mathbf{P}_x^T \mathbf{U}_x)^{-1}$ can be pre-computed online and the sampled non-linear operator $\mathbf{P}_x^T \mathbf{h}_x(\mathbf{V}_x \hat{\boldsymbol{\phi}}_x)$ is only evaluated on n_{hr} interpolation indices.

The hyper-reduced system of equations reads as

$$\begin{bmatrix} \hat{\mathbf{A}}_{u_1 u_1} & \hat{\mathbf{A}}_{u_1 u_2} & \hat{\mathbf{A}}_{u_1 p} \\ \hat{\mathbf{A}}_{u_2 u_1} & \hat{\mathbf{A}}_{u_2 u_2} & \hat{\mathbf{A}}_{u_2 p} \\ \hat{\mathbf{A}}_{p u_1} & \hat{\mathbf{A}}_{p u_2} & \hat{\mathbf{A}}_{p p} \end{bmatrix} \begin{bmatrix} \hat{\boldsymbol{\phi}}_{u_1} \\ \hat{\boldsymbol{\phi}}_{u_2} \\ \hat{\boldsymbol{\phi}}_p \end{bmatrix} + \begin{bmatrix} \hat{\mathbf{h}}_{hr,u_1}(\hat{\boldsymbol{\phi}}_{u_1}) \\ \hat{\mathbf{h}}_{hr,u_2}(\hat{\boldsymbol{\phi}}_{u_2}) \\ \hat{\mathbf{h}}_{hr,p}(\hat{\boldsymbol{\phi}}_p) \end{bmatrix} = - \begin{bmatrix} \hat{\mathbf{b}}_{u_1} \\ \hat{\mathbf{b}}_{u_2} \\ \hat{\mathbf{b}}_p \end{bmatrix}. \quad (4.13)$$

We refer to this model as the hyper-reduced model.

The key to simplifying the complexity of the non-linear operator is to identify a sampling operator \mathbf{P}_x that effectively selects the specific indices most suitable for accurate approximation. The sampling points in \mathbf{P}_x can be determined in various ways and the success of the method depends entirely this choice. In this chapter we use three choices for \mathbf{P}_x .

We employ the Discrete Empirical Interpolation Method (DEIM) [23], Q-DEIM [35], and S-OPT [81] sampling techniques to determine the sampling operator \mathbf{P}_x . DEIM utilizes a greedy algorithm to select indices by sequentially identifying maxima in the basis, while Q-DEIM determines \mathbf{P}_x through QR factorization with column pivoting, making it independent of the basis ordering. Both DEIM and Q-DEIM aim to maximize the smallest singular values of the projection matrix. In contrast, S-OPT finds \mathbf{P}_x by maximizing the product of all singular values and enhancing the orthogonality of the sampling operator's columns, offering a different approach to selecting the optimal sampling points.

4.3 Finite element hyper-reduction with isogeometric solutions

In the hyper-reduced system of equations, (4.13), $\hat{\mathbf{h}}_{\text{hr},x}$ in (4.12) is evaluated in two parts. The first part, $\mathbf{V}_x^T \mathbf{U}_x (\mathbf{P}_x^T \mathbf{U}_x)^{-1}$, can be pre-computed. However, the second part, $\mathbf{P}_x^T \mathbf{h}_x (\mathbf{V}_x \hat{\phi}_x)$, is evaluated in the online stage upon every iteration.

We use the libROM library [25] as our reduction tool. This open-source library is specifically designed for model order reduction, helping to lower the computational costs of large-scale simulations while offering a variety of implemented hyper-reduction methods. To effectively evaluate $\mathbf{P}_x^T \mathbf{h}_x (\mathbf{V}_x \hat{\phi}_x)$ in the online stage in libROM, we construct a sample mesh containing only the degrees of freedom to evaluate the sampled degrees of freedom in \mathbf{P}_x . This sample mesh is used to construct non-linear operators that only evaluate $\mathbf{P}_x^T \mathbf{h}_x (\mathbf{V}_x \hat{\phi}_x)$. Unfortunately, implementing such an approach in an isogeometric analysis discretization is not trivial. The tensor structure of isogeometric analysis makes that a large number of variables are interrelated, which complicates the process. We therefore use the existing implementation of sample meshes for discretisations using finite elements.

We use the finite element framework as an intermediate step in hyper-reduction in isogeometric analysis. In this way we are able to exploit the high continuity associated with isogeometric analysis discretisations and the flexibility of finite element discretisations. We first introduce the solution in the isogeometric analysis frame-

work ϕ_I and the solution in the finite element framework ϕ_F . These solutions are virtually the same as ϕ_F is ϕ_I projected onto the finite element space.

We project the isogeometric solution on the finite element space to get the finite element solution using

$$\phi_F = \mathbf{K}\phi_I. \quad (4.14)$$

The operator \mathbf{K} can be interpreted as

$$\mathbf{K} = \mathbf{K}_{I2F}\mathbf{K}_{KI} \quad (4.15)$$

where \mathbf{K}_{KI} is an operator that represents knot insertion, making the isogeometric shape functions C^0 -continuous. \mathbf{K}_{I2F} is the operator projecting the IgA solution onto the finite element solution.

The operator \mathbf{K}_{KI} re-inserts the internal knots such that the knot vectors associated with the mesh consist entirely of repeated internal knots. It is important to note that while \mathbf{K}_{KI} allows for the possibility of reduced smoothness in the solution, it does not inherently decrease the smoothness. Instead, it maps the solution into a larger space, but only a small portion of that space is utilized. After applying \mathbf{K}_{KI} , the solution still has its initial continuity.

The basis \mathbf{V}_x in the finite element context is constructed as follows. First, we find the isogeometric analysis solution ϕ_I by evaluating the full-order model in the offline stage for a choice of input parameter μ . Then, we apply (4.14) to find ϕ_F and construct the snapshot matrix \mathbf{X}_ϕ with ϕ_F in its columns. We apply a POD to find the basis \mathbf{V}_x for each variable x .

The basis associated with the construction of the non-linear operator \mathbf{V}_x in the finite element context is constructed similarly. With ϕ_F already available, we evaluate the non-linear contribution on the finite element space $\mathbf{h}_F(\phi_F)$. We only have to construct a snapshot matrix \mathbf{X}_h with $\mathbf{h}_F(\phi_F)$ in its columns. \mathbf{U}_x is found by applying a POD on \mathbf{X}_h .

With \mathbf{V}_x and \mathbf{U}_x in the finite-element context available, we simply have to construct $\hat{\mathbf{A}}_{xy}$ and $\hat{\mathbf{b}}_x$ on the finite-element discretisation. We can evaluate the sampling operator \mathbf{P}_x on a finite-element space and solve (4.13) efficiently in the finite-element context.

4.4 Numerical experiments

In this section, we apply the hyper-reduced model. First, we apply the model to two-dimensional stationary flow as verification. We study one case in which the viscosity is systematically varied. Hereafter, we assess three parameter studies considering variations in the parameters period, viscosity, and motion profile on the hyper-reducability of the problem. The same cases have been studied in [89] (Chapter 3) for the reduced-order model.

Similar to [89], the full-order model, we stabilize the reduced-order model and hyper-reduced order model with residual-based variational multiscale turbulence modelling [11, 12] and discontinuity capturing such as in [61]. The boundary condition on the internal boundary P_{int} is enforced weakly [13]. Appendix 4.A gives the numerical parameters required for the stabilisation, the boundary conditions and the pseudo-transient relaxation. We discretize the spatial domain with five second-order NURBS patches with 68 control points between the foil section and the inflow boundary, 62 control points over the length of the foil section and 78 control points between the foil section and the outflow boundary. The total number of variables for the spatial discretisation is $\mathcal{O}(9 \cdot 10^4)$. The temporal discretization employs 49 control points for space-time simulations. The total number of variables for the space-time discretisation is $\mathcal{O}(2.7 \cdot 10^6)$.

We construct a snapshotmatrix \mathbf{X}_ϕ with 30 solutions of the full-order model ϕ_x for a linear spacing of μ in a selected range in its columns. Furthermore, we construct a snapshotmatrix \mathbf{X}_h with 30 entries of $\mathbf{h}_x(\phi_x)$ with the same choices of μ . We use these to construct \mathbf{V}_x and \mathbf{U}_x . Realize that the number of columns in the snapshot matrix limits the number of reduced order model variables, n_r , and number of columns in the sampling operator \mathbf{P} , n_{hr} . This means that $n_r \leq \text{columns}(\mathbf{X}_\phi)$, and $n_{hr} \leq \text{columns}(\mathbf{X}_\phi)$. Note that the number of columns in the sampling operator \mathbf{P} is equal to n_{hr} .

4.4.1 Verification using the Navier-Stokes equations for steady flow

First, we verify the implementation of the hyper-reduced reduced-order model in (4.13) using a numerical experiment consisting of steady flow past a foil section with a variation of Reynolds number. The Reynolds number describes the ratio between inertial and viscous forces in fluid flow. We use the Reynolds number with the chord c as the length scale,

$$\text{Re} = \frac{U c}{\nu}, \quad (4.16)$$

with free-stream velocity U . We study low Reynolds number flow, with $\text{Re} < 1000$, below the transition regime to turbulent flow. The constant angle of attack is 2° and the chord length $c = 1$.

In this section, we first determine a value for n_r by reducing the missing information in the basis ϵ_{POD} in (4.5) using the reduced-order model (without hyper-reduction). Next, we examine the behavior of the hyper-reduced model with this n_r value, focusing on the effects of the basis size and the number of samples in \mathbf{P} , denoted by n_{hr} .

The bases \mathbf{V}_x and \mathbf{U}_x are constructed by sampling the solutions of the full-order model in $200 \leq \text{Re} \leq 800$. Figure 4.2 gives the singular values associated with the construction of \mathbf{V}_x and \mathbf{U}_x . The figure shows a steep initial decline in singular values associated with the construction of \mathbf{V}_x and \mathbf{U}_x . From this, we can conclude that the problem is probably reducible and hyper-reducible.

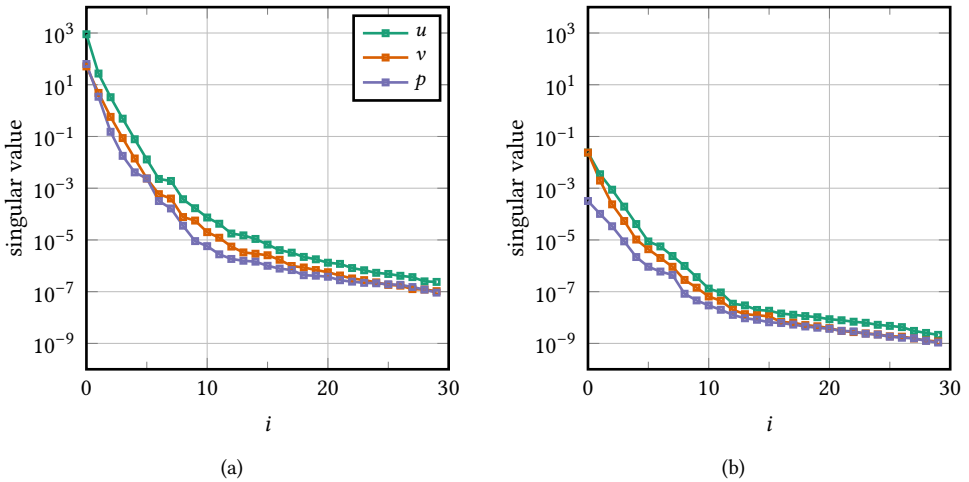


Figure 4.2: Singular values associated with the construction of a) the basis \mathbf{V}_x for u , v and p , and b) the basis \mathbf{U}_x used for the reconstruction of the non-linear contribution to the residual $\hat{\mathbf{h}}_{hr,x}$.

We compare the solution of the reduced-order model and the hyper-reduced model and the corresponding forces to assess the correctness of the hyper-reduced model. We evaluate the reduced-order and hyper-reduced model at the unsampled

$Re = 416.7$. The l_2 -norm of the error of the (hyper-)reduced model with the full-order model computes as

$$\epsilon_x = \sqrt{(\tilde{\phi}_x - \phi_x) \cdot (\tilde{\phi}_x - \phi_x) / \sqrt{\phi_x \cdot \phi_x}}. \quad (4.17)$$

The normalized error of the forces computed by the reduced-order model and hyper-reduced model (ROM) concerning the force of the full-order model (FOM) is computed as

$$\epsilon_F = \left| \frac{F_{ROM} - F_{FOM}}{F_{FOM}} \right|. \quad (4.18)$$

Here, F is a force in x_1 or x_2 -direction.

Figure 4.3 gives the solution and force errors for the reduced-order model with respect to the full-order model. The errors decrease upon increasing the size of the basis \mathbf{V}_x and stabilize at $\epsilon_{\text{POD}} = 1e-6$. The decrease is not constant and shows some fluctuation. For the upcoming results, we fix the sizes of bases \mathbf{V}_x such that the value for the missing information in the basis $\epsilon_{\text{POD}} = 1e-6$. Beyond this point, adding more information does not improve the solution.

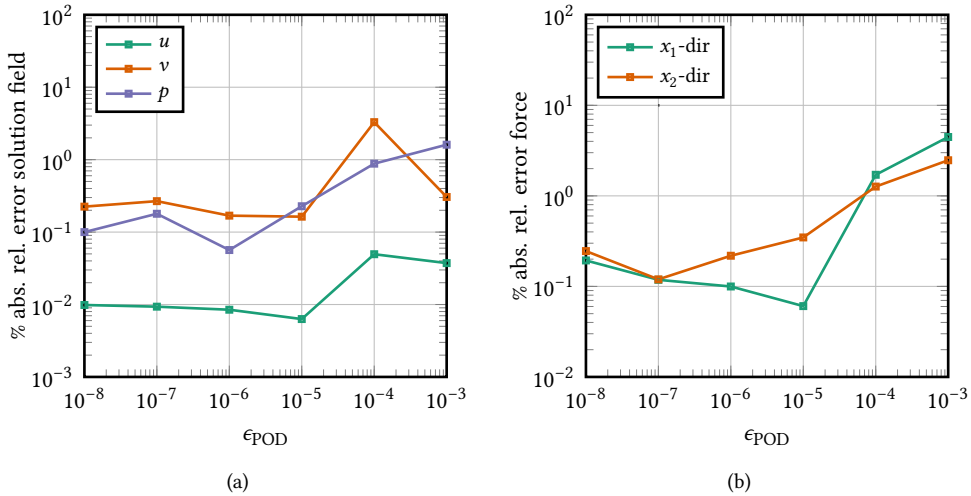


Figure 4.3: The solution (4.17) and force errors (4.18) for the reduced-order model with respect to the full-order model.

Figure 4.4 gives the results of the hyper-reduced model using the DEIM, Q-DEIM and S-OPT sampling methods while increasing the size of \mathbf{U}_x . We use a constant $\epsilon_{\text{POD}} = 1e-6$ for the size of \mathbf{V}_x . We plot the results of the (not hyper-reduced) reduced-order model with horizontal lines for easy comparison.

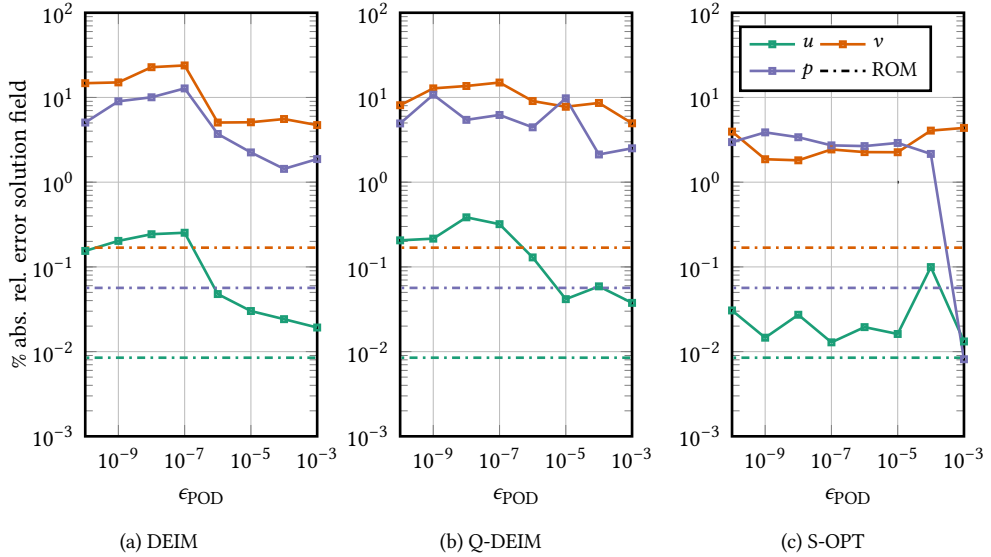


Figure 4.4: Relative error of the solution field (4.17) as function of basis size for the DEIM [23], Q-DEIM [35] and S-Opt [81] sampling techniques. The horizontal lines represent the errors of the (not hyperreduced) reduced-order model results as a reference.

As expected, the errors of the hyper-reduced model $\mathcal{O}(0.01\% - 10\%)$ are larger than those of the reduce-order model $\mathcal{O}(0.01\% - 0.1\%)$. The S-OPT sampling method performs the best with errors $< 5\%$. The DEIM sampling method is the worst with errors $< 12\%$. Using the S-OPT method, the error of the hyper-reduced model increases with a factor of $\mathcal{O}(10)$ with respect to the reduced-order model.

The errors of the hyper-reduced model using the DEIM and Q-DEIM sampling method fluctuate upon increasing the size of \mathbf{U}_x , similar to the results of the reduced-order model with increasing the size of \mathbf{V}_x . The results of the hyper-reduced model using the S-OPT sampling method are stable when increasing the size of \mathbf{U}_x .

Figure 4.5 visualizes the errors of the force F of the hyper-reduced model in x_1 and x_2 -direction with respect to the full order model. Also here, we plot the results of the (not hyper-reduced) reduced-order model with horizontal lines for easy comparison. The force errors computed with the hyper-reduced model also fluctuate for the DEIM and the Q-DEIM sampling methods and are smaller than 10%. The force errors computed with S-OPT sampling fluctuate less and are smaller than 4%.

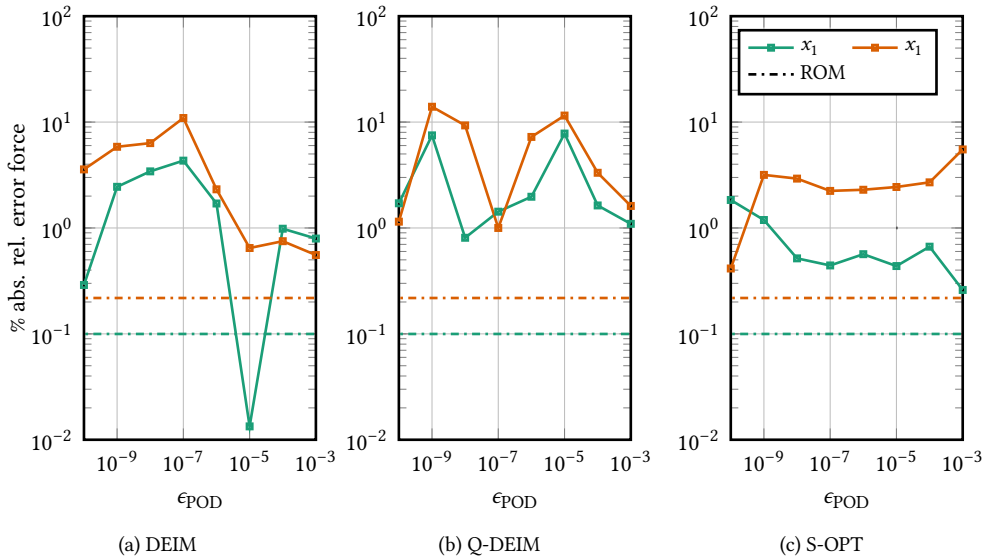


Figure 4.5: Relative error of the force (4.18) as function of basis size for the DEIM [23], Q-DEIM [35] and S-Opt [81] sampling techniques. The horizontal lines represent the errors of the (not hyper-reduced) reduced-order model results as a reference.

We analyze the performance of the hyper-reduced order model by comparing its wall-clock time with that of the reduced-order and the full-order model. The reduced-order and full-order model require 32 processors to find a solution. The hyper-reduced model finds a solution using only one processor. We define the speed-up as

$$\text{speed-up} = \frac{\#\text{proc FOM} \cdot \text{wall-clock time FOM}}{\#\text{proc ROM} \cdot \text{wall-clock time ROM}}. \quad (4.19)$$

Figure 4.6 gives the typical speed-up of the reduced-order model and the hyper-reduced model using $\epsilon_{\text{POD}} = 1e-6$ for the size of \mathbf{V}_x and \mathbf{U}_x . These results are typical and show the great potential of the hyper-reduction methods. The speed-up of the reduced-order model is of $\mathcal{O}(10^2)$. The speed-up of the hyper-reduced model is $\mathcal{O}(10^5)$. The typical wall-clock time of the hyper-reduced model is $\mathcal{O}(10^{-2})$ seconds, allowing for real-time computations.

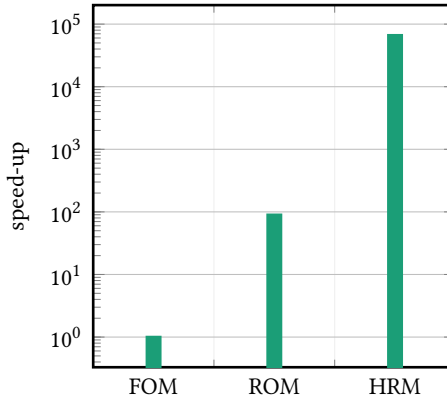


Figure 4.6: Typical speed-up (4.19) of reduced-order model (ROM), hyper-reduced model (HRM) with respect to the full-order model (FOM).

The hyper-reduced model shows the expected behaviour for the studied test case. The errors of the solution and the forces computed by the hyper-reduced model are acceptable and greater than the errors of the reduced-order model.

4.4.2 Towards hyper-reduction for time-periodic problems

We have been unable to successfully evaluate the hyper-reduced model for three time-periodic problems considering flow past flapping foil sections. We have tested the hyper-reduced model on parameter studies considering variations in the parameters period, viscosity, and motion profile. In these experiments, the solution did not converge for all possible choices of the size of \mathbf{U}_x and sampling methods.

The same three numerical experiments with the hyper-reduced model are described elaborately in [89]. We give a short description here. In the first two experiments, the heave motion is sinusoidal and given by

$$h(t) = h_a \sin\left(\frac{2\pi t}{T}\right), \quad (4.20)$$

where T is the period and h_a heave-amplitude. In the third experiment, the motion is non-sinusoidal.

The first experiment studies the interaction between the wake produced by a heaving foil-section and the foil-section. The interaction is characterized by the Strouhal number

$$\text{St} = \frac{2 h_a}{U T}. \quad (4.21)$$

The Reynolds number (4.16) is constant at $\text{Re} = 800$, and the motion-amplitude is fixed at $h_a/c = 0.5$.

The second experiment studies the effect of the Reynolds number on thrust. The Reynolds number describes the ratio of inertial forces to viscous forces in fluid flow. We explore the range of $200 \leq \text{Re} \leq 800$. The motion-amplitude is constant at $h_a/c = 0.5$. The Strouhal number is fixed at $\text{St} = 0.125$.

The last experiment studies the influence of the motion profile on thrust with a family of motion shapes characterized by

$$h(t) = h_a \sin(\omega t + \phi(t)), \quad (4.22a)$$

$$\phi(t) = \phi_a \cos(\omega t). \quad (4.22b)$$

where ϕ_a describes the phase-amplitude. We use the phase-amplitude range of $0.1 \leq \phi_a \leq 0.6$. The motion-amplitude is constant at $h_a/c = 0.5$, and the Strouhal number is fixed at $\text{St} = 0.125$. The Reynolds number is constant at $\text{Re} = 800$.

Figures 4.7, 4.8 and 4.9 give the singular values associated with the construction with the solution basis \mathbf{V}_x and the basis \mathbf{U}_x used for the reconstruction of the non-linear contribution to the residual $\hat{\mathbf{h}}_x$ for the three numerical experiments.

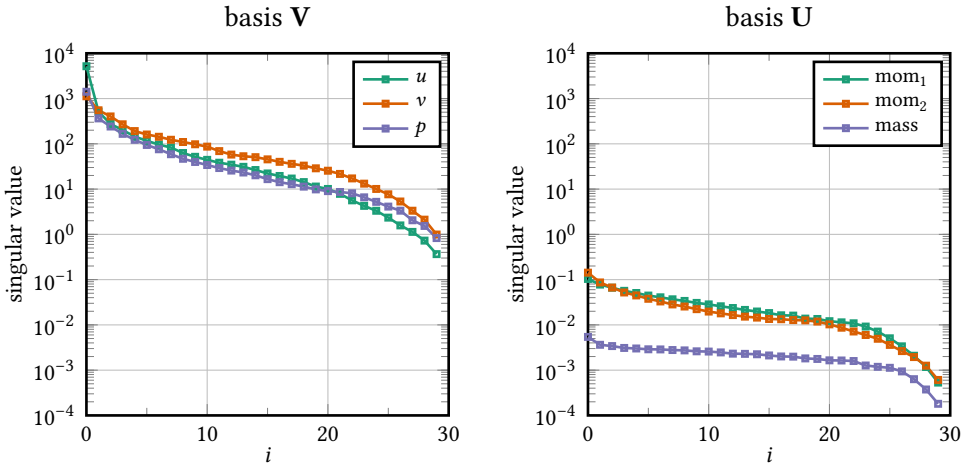


Figure 4.7: Singular values associated with the construction of the solution basis \mathbf{V}_x and the basis \mathbf{U}_x used for the reconstruction of the non-linear contribution to the residual $\hat{\mathbf{h}}_x$ for numerical experiments with a variation in Strouhal number.

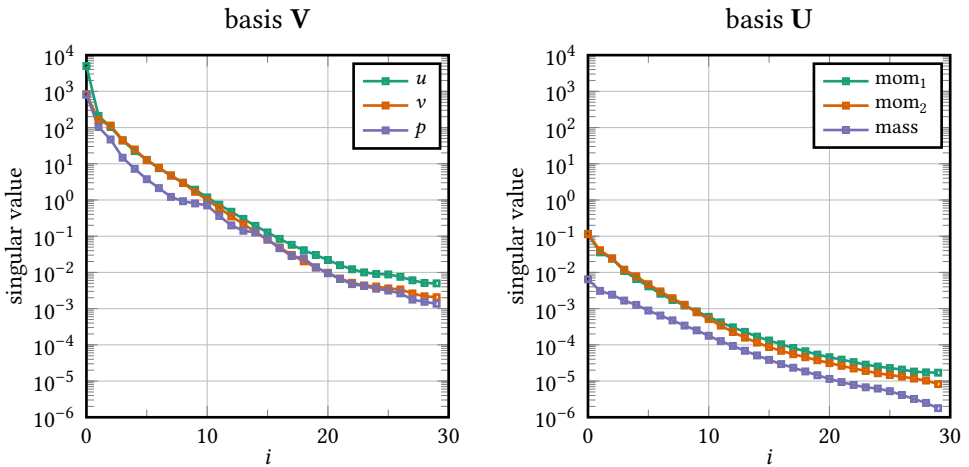


Figure 4.8: Singular values associated with the construction of the solution basis \mathbf{V}_x and the basis \mathbf{U}_x used for the reconstruction of the non-linear contribution to the residual $\hat{\mathbf{h}}_x$ for numerical experiments with a variation in Reynolds number.

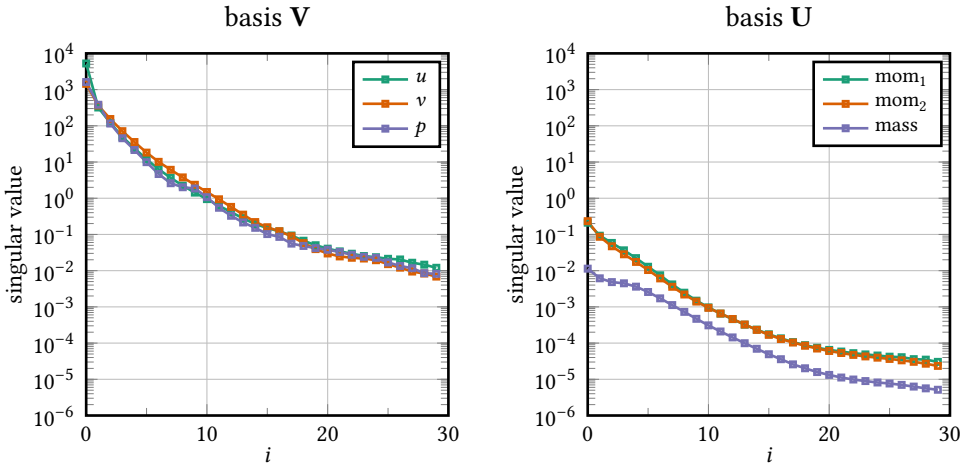


Figure 4.9: Singular values associated with the construction of the solution basis \mathbf{V}_x and the basis \mathbf{U}_x used for the reconstruction of the non-linear contribution to the residual $\hat{\mathbf{h}}_x$ for numerical experiments with a variation in motion profile.

There are at least two reasons why the hyper-reduced model may fail to find a solution. First, the assumption in (4.9) where we approximate $\mathbf{h}_x(\mathbf{V}_x \hat{\phi}_x)$ might not hold for the studied test case in the time-periodic frame work. Second, it might also be possible that with the approximation in (4.11) the stability of the time-periodic space-time system is altered such that it is unable to find a solution.

The figures indicate that the singular values associated with the construction of the basis \mathbf{U}_x decay slower than the ones associated with the construction of the basis \mathbf{V}_x for the three experiments. The ratio of $\sigma_{\min}/\sigma_{\max}$ is a factor of $\mathcal{O}(10^2)$ higher for the singular values associated with the construction of \mathbf{V}_x than the singular values associated with the construction of the basis \mathbf{U}_x for the three experiments. Based on (4.5), this indicates that a larger basis \mathbf{U}_x is required to capture the same amount of information as for a basis \mathbf{V}_x and that the assumption in (4.9) might not hold.

We have studied the effect of increasing the size of the basis \mathbf{U} beyond 30. We increased the size of \mathbf{U}_x up to 60, by sampling additional solutions for the Reynolds number experiment in the offline stage. The solution did also not converge for this larger basis. Constructing an even larger basis is not feasible due to the high computational costs. This can be related to a slow decay of the Kolmogorov n -width. In other words, a disproportional amount of information is required to reduce the approximation error sufficiently in Equation (4.9).

One may also wonder if the approximation of the coefficient vector \mathbf{c}_x in (4.11) holds. With approximating \mathbf{h}_x by sampling only a small percentage of its entries, the stability of the non-linear system in (4.7) might be adjusted. This prevents finding a solution to the system. Similar behavior has been seen by including [19], where they required very precise tuning of ϵ_{POD} in (4.5).

4.5 Conclusions

We have implemented a hyper-reduced model using empirical interpolation method hyper-reduction techniques. The hyper-reduced model is independent of the complexity that scales with the size of the full-order model.

We have successfully evaluated the hyper-reduced model on steady two-dimensional flow. The solution and force error of the hyper-reduced model with respect to the full-order model is of $\mathcal{O}(0.01\% - 10\%)$ depending on the sampling method. These errors are larger than the ones computed by the reduce-order model, which are $\mathcal{O}(0.01\% - 0.1\%)$. The S-OPT sampling method performed the best in the hyper-reduced model. The corresponding speed-up of the hyper-reduced model compared to the full-order model is $\mathcal{O}(10^5)$, which is a speed-up of $\mathcal{O}(10^3)$ to the reduced-order model. The typical wall-clock time of the hyper-reduced model of $\mathcal{O}(10^{-2})$ seconds allows for real-time computations.

We were unable to evaluate the hyper-reduced model for time-periodic flow. This difficulty may be attributed to the linear approximation of the non-linear operator or the modified stability characteristics of the hyper-reduced model. To address these challenges, future research could benefit from exploring areas such as the application of the empirical quadrature procedure or the development of neural-network-based reduced-order models, such as autoencoders. Additionally, the direct application of hyper-reduction in isogeometric discretizations would offer significant advantages.

4.A Numerical parameters

4.1 gives the numerical parameters required for the stabilisation, the boundary conditions and the pseudo-transient relaxation for reproduction of the results.

Table 4.1: Numerical parameters and their corresponding values.

| Parameter | Value |
|----------------|-------|
| s | 1 |
| a | 4 |
| C_I | 36 |
| C_b | 8 |
| C_{dc} | 0.3 |
| $\Delta\theta$ | 1.0 |

5

Study of flow past a vertical-axis wind turbine

5

Vertical-axis wind turbines offer significant advantages for urban applications due to their lower noise levels, but their performance is highly sensitive to various factors requiring high-fidelity simulations to optimize its performance. This chapter investigates the application of a time-periodic reduced-order model for analyzing the flow past a single-bladed vertical-axis wind turbine at a Reynolds number of 1000. The reduced-order model is validated against experimental data and used to study flow characteristics as a function of tip-speed ratio. The results demonstrate that the reduced-model can achieve accurate predictions with significantly less data during the offline stage compared to previous work. Additionally, the model was used to determine the optimal operating point of the turbine, maximizing energy production per cycle under the given conditions. It was observed that the turbine's energy output was negative, likely due to the low Reynolds number used in this study. The findings suggest that the time-periodic reduced-order model is well-suited for industrial applications involving vertical-axis wind turbines. Future work should focus on extending the model to include parameters such as angle of attack, tip-speed ratio, and non-dimensional radius at higher Reynolds numbers for a more comprehensive analysis. Furthermore, incorporating fluid-structure interaction could help in understanding potential instabilities like flutter, further enhancing the model's applicability in practical scenarios.

5.1 Introduction

Wind energy is key in achieving a climate-neutral global power strategy [10], and vertical-axis wind turbines can contribute to this goal. Unlike horizontal-axis wind turbines, vertical-axis wind turbines are especially advantageous for urban settings due to their lower noise levels [122]. However, their efficiency and optimal performance depend on various factors such as blade design, flow conditions, and operational parameters. A vast amount of research focuses on understanding these factors, as detailed in the comprehensive reviews by [33, 110]. Among these factors, dynamic stall is a key phenomenon that significantly impacts the vertical axis wind turbine performance [82, 83], making accurate flow predictions essential to study power production. In this context, parametric reduced-order modelling emerges as a valuable tool for optimizing vertical-axis wind turbine performance. This chapter has two primary objectives: first, to demonstrate the applicability of the reduced-order model in industrial problems, and second, to analyze the flow past vertical-axis wind turbines and show how the reduced-order model can be utilized to identify its optimal operating point under specific flow conditions.

We investigate the flow characteristics past a Darrieus-type vertical axis wind turbine, as depicted in Figure 5.1, using a reduced-order model. We approximate the flow past the turbine as two-dimensional, providing a simplified model that captures the essential features of the flow dynamics. A schematic representation of the turbine is depicted in Figure 5.1b. In this study, we focus exclusively on the flow around a single blade, thereby excluding the complex interactions of wake effects between multiple blades. This approach allows for a more controlled analysis of the interaction between the wake produced by a single blade and the blade itself.

We study the flow past the vertical axis wind turbine using a time-periodic POD-Galerkin reduced-order model described in [89], Chapter 3. The reduced-order model employs a time-periodic full-order model [88], Chapter 2, and a time-periodic basis to effectively approximate the pressure and the velocity field. The reduced model is developed and evaluated through three key stages. The first stage, the offline stage, involves running the full-order model for different parameter values of interest, with the resulting solutions stored in a snapshot matrix. In the second stage, the merge stage, a basis is generated by gathering the solutions into a solution matrix and applying proper orthogonal decomposition (POD) to identify the time-periodic basis. In the final stage, the online stage, the reduced-order model is constructed by approximating the solution using this basis and projecting the full-order system of equations onto it. The reduced-order model is then evaluated during the online stage.

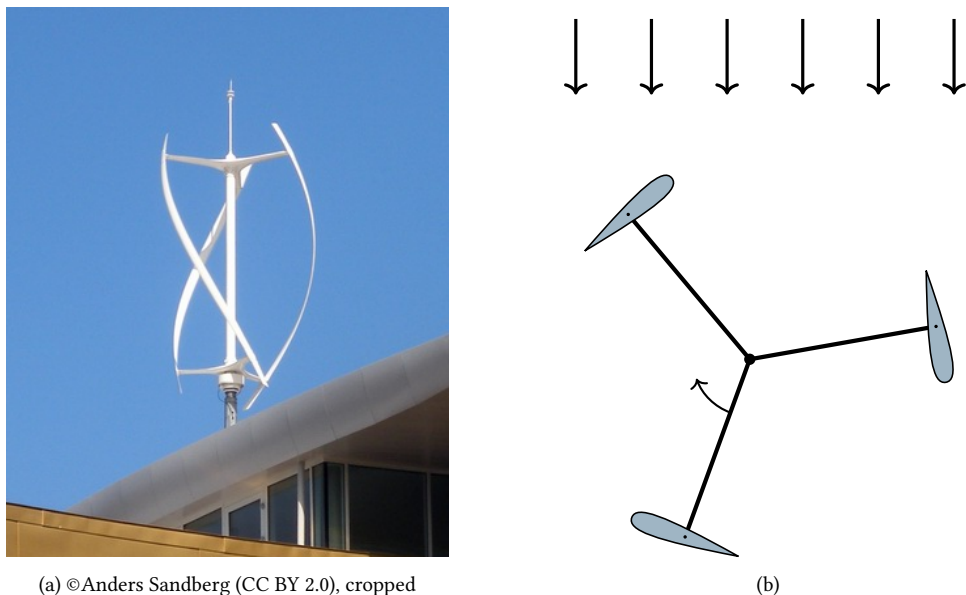


Figure 5.1: Vertical axis wind turbine in operation and its schematical representation with inflow due to wind.

In section Section 5.2, we introduce the model problem and the governing parameters. The latter can be leveraged for non-dimensionalization of the problem and applying model order reduction. This section also explains the modelling approach within a non-inertial frame of reference and provides a short introduction to both the full-order and reduced-order models. Following this, in Section 5.3, we validate the implementation of the non-inertial frame of reference using experimental results. We study a reduced-order model built for the tip-speed ratio, which is the ratio of the turbine's rotational speed to the inflow velocity at a Reynolds number of 1000. Section 5.4 evaluates the reduced-order model's suitability for industrial applications to vertical-axis wind turbines. We examine the amount of data needed to construct the reduced-order model, to reduce its costs in the offline stage. Next, in Section 5.5 we study the accuracy of the reduced-order model and explore how variations in the tip-speed ratio affect flow characteristics. Last, in Section 5.6, we demonstrate how the reduced-order model can be used to optimize the performance of vertical-axis wind turbines. Conclusions are drawn in Section 5.7.

5.2 The reduced-order model of vertical axis wind turbine

In this section, we first present the model problem and introduce the non-dimensionalization process within a non-inertial frame of reference. Following this, we introduce both the full-order and reduced-order models.

The flow past the turbine is characterized by three essential non-dimensional parameters, which are used to non-dimensionalize the model problem. The first parameter is the non-dimensional radius \tilde{R} , defined as the ratio of the turbine's radius R to the blade chord length c ,

$$\tilde{R} = \frac{R}{c}. \quad (5.1)$$

The non-dimensional radius is typically $\tilde{R} \geq 2.5$ [83]. The second parameter is the tip-speed ratio λ , which represents the ratio of the blade velocity to the free-stream velocity U_∞ ,

$$\lambda = \frac{\omega R}{U_\infty}. \quad (5.2)$$

where $\omega = 2 * \pi T$ with period T . Low tip-speed ratios ($\lambda \leq 2.5$) are characterized by large amplitude variations in angles of attack, leading to dynamic stall and a subsequent drop in the power coefficient. At high tip-speed ratios ($\lambda \geq 4$), the turbine experiences lower angles of attack, resulting in reduced power and force coefficients [83]. The maximum power coefficient typically occurs between these two extremes. The third parameter is the Reynolds number Re , defined as

$$Re = \frac{\omega R c}{\nu}, \quad (5.3)$$

where ν is the kinematic viscosity of the fluid. The typical Reynolds number of the flow past a vertical axis wind turbine is $\mathcal{O}(10^5)$ [82, 83].

5.2.1 Model problem

We model the flow past the vertical axis-wind turbine using the Navier-Stokes equations for incompressible flow. The model problem reads as

$$\partial_t \mathbf{u} + \mathbf{u} \cdot \nabla \mathbf{u} + \nabla p - \nu \nabla^2 \mathbf{u} = \mathbf{f} \quad \text{in } Q, \quad (5.4a)$$

$$\nabla \cdot \mathbf{u} = 0 \quad \text{in } Q, \quad (5.4b)$$

$$\mathbf{u} = \mathbf{g}_{\text{int}} \quad \text{in } P_{\text{int}}, \quad (5.4c)$$

$$\mathbf{u} = \mathbf{g}_{\text{ext}} \quad \text{in } P_{\text{ext}}^D, \quad (5.4d)$$

$$-p \mathbf{n} + \nu \nabla \mathbf{u} \cdot \mathbf{n} + u_n^- \mathbf{u} = \mathbf{0} \quad \text{in } P_{\text{ext}}^N, \quad (5.4e)$$

$$\mathbf{u}(\cdot, 0) = \mathbf{u}(\cdot, T) \quad \text{in } \Omega. \quad (5.4f)$$

Here, $Q = \Omega \times \mathcal{I}$ denotes the space-time domain with boundary P . The space-time boundary is decomposed in the inflow boundary P_{ext}^D , the outflow boundary P_{ext}^N and the internal no-slip boundary P_{int} . The kinematic viscosity is represented by ν , \mathbf{f} denotes a dimensionless external force which is described in more detail later. Dimensionless \mathbf{g}_{int} and \mathbf{g}_{ext} are the prescribed velocities on the interior and exterior boundaries. Note that using (5.4f), instead of an initial condition, transforms the time-dependent problem into a boundary value problem.

Figure 5.2 visualizes the spatial domain in its inertial frame of reference Ω_{iner} and its boundaries Γ . The rotation of the vertical-axis wind turbine in Figure 5.1b is represented by rotation of the internal boundary by moving Γ_{int} .

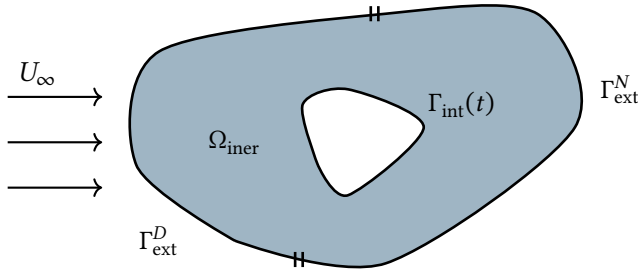


Figure 5.2: Schematical representation of the spatial domain in an inertial frame of reference with its boundaries. The arrows on the left indicate the direction of the flow.

5.2.2 The non-inertial frame of reference

We model the flow around the blade of a vertical-axis wind turbine using a non-inertial reference frame. This approach allows us to use a simple mesh, as it eliminates the need to account for the full motion of the turbine within the mesh by moving Γ_{int} .

The non-inertial domain $\Omega_{\text{non-iner}}$ is illustrated in Figure 5.3. Here, the rotation of the vertical-axis wind turbine, depicted in Figure 5.1b is modelled, through a combination of the inflow into the domain, \mathbf{g}_{ext} , and an external forcing term, \mathbf{f} . The motion of the internal boundary $\Gamma_{\text{int}}(t)$ can be used to model blade instabilities, such as flutter. However, we choose it as time-independent, resulting in $\mathbf{g}_{\text{int}} = \mathbf{0}$.

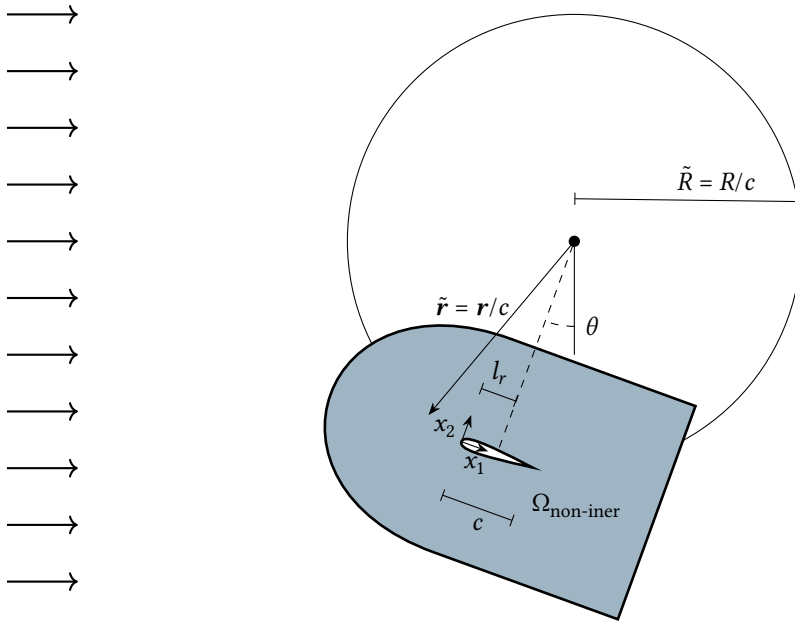


Figure 5.3: The domain Ω in a non-inertial frame of reference surrounding a blade of a vertical axis wind turbine. The coordinates x and y are in units of chord c .

In Figure 5.3, θ represents the azimuthal angle, which is zero when the blade is aligned with the external flow. The rod is attached to the turbine blade at a distance l_r from the blade tip. The coordinate $\tilde{\mathbf{r}}$ relates the centre of rotation to the domain. Its dimensionless form, with respect to the chord c , reads as $\tilde{\mathbf{r}} = \mathbf{r}/c$.

We non-dimensionalize the boundary velocity with respect to the rotational velocity of the turbine blade ωR . With this, governing parameters can be set freely without affecting each other. Then, we decompose the inflow boundary velocity into two components,

$$\mathbf{g}_{\text{ext}} = \mathbf{g}_{\text{rot}} + \mathbf{g}_{\infty} \quad \text{on } \Gamma. \quad (5.5)$$

Here, the velocities denoted by the subscript *rot* correspond to the inflow generated by the turbine's rotation, while those with the subscript ∞ represent the external turbine inflow due to U_{∞} . The inflow velocities are non-dimensionalized with respect to the rotational velocity of the foil section, ωR .

The non-dimensional inflow due to the rotation of the turbine is

$$\mathbf{g}_{rot} = \frac{\omega \mathbf{r}}{\omega R} = \frac{\tilde{\mathbf{r}}}{\tilde{R}} \quad \text{in } \Gamma. \quad (5.6)$$

The non-dimensional inflow due to the external turbine inflow U_∞ reads as

$$\mathbf{g}_\infty = \frac{U_\infty}{\omega R} \begin{bmatrix} \cos \theta \\ \sin \theta \end{bmatrix} = \frac{1}{\lambda} \begin{bmatrix} \cos \theta \\ \sin \theta \end{bmatrix} \quad \text{in } \Gamma. \quad (5.7)$$

The forcing term is composed of two components: the centrifugal force, denoted by the subscript ce , and the Coriolis force, denoted by the subscript co . The split is expressed as

$$\mathbf{f} = \mathbf{f}_{ce} + \mathbf{f}_{co} \quad \text{in } \Omega_{\text{non-iner}}. \quad (5.8)$$

The centrifugal force is non-dimensionalized with respect to the chord length and the blade velocity. It reads as

$$\mathbf{f}_{ce} = \omega^2 \mathbf{r} \frac{c}{\omega^2 R^2} = \mathbf{r} \frac{c}{R^2} = \mathbf{r}/c \frac{1}{(R/c)^2} = \tilde{\mathbf{r}} \frac{1}{\tilde{R}^2}. \quad \text{in } \Omega_{\text{non-iner}}. \quad (5.9)$$

The Coriolis force is similarly non-dimensionalized, using a coefficient $f(\tilde{R}, \omega, c)$. This coefficient is selected to ensure consistency with the chosen non-dimensionalization of other parameters. The resulting non-dimensional Coriolis force is denoted as

$$\mathbf{f}_{co} = \frac{2}{\lambda} f(\tilde{R}, \omega, c) \begin{bmatrix} -\sin \theta \\ \cos \theta \end{bmatrix} \quad \text{in } \Omega_{\text{non-iner}}. \quad (5.10)$$

5.2.3 Evaluation of the full-order model

The full-order model is evaluated in the offline stage [88]. It employs space-time isogeometric analysis [58], where space and time are treated equally, and the variational multi-scale method as turbulence model [12]. Figure 5.4 depicts the domain and indicates the orientation of the NURBS patches. To reduce computational demands of the offline stage, the size of the domain is reduced to three chords instead of the recommended eight chords to exclude influences of the inflow boundary [14, 88]. This means that the inflow boundary might have a small effect on the results, but we can use fewer control points to discretize the domain between the foil section and the inflow boundary.

In this discretization, the patches are refined to 34 control points between the foil section and the inflow boundary, 62 control points along the foil section's length, and 78 control points between the foil section and the outflow boundary. Additionally, time is discretized using 49 control points. Overall, this discretization utilizes only 50% of the control points compared to the flapping foil simulations in Chapter 3.

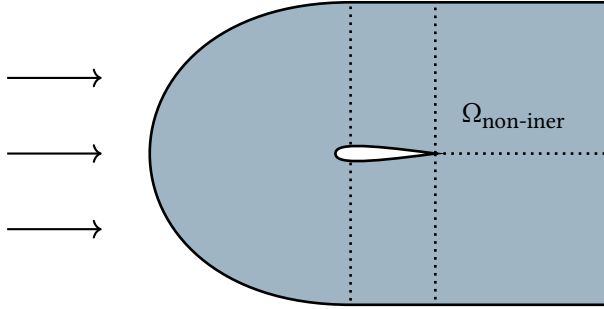


Figure 5.4: Schematic representation of NURBS patches in the domain $\Omega_{\text{non-iner}}$, surrounding the hydrofoil. The five NURBS patches are indicated with a dotted line.

5.2.4 Model reduction

We create a POD-Galerkin reduced-order model for a single-bladed vertical-axis wind turbine for a variation of the tip-speed ratio λ (5.2), following [89]. In the offline stage, we sample space-time solutions for values of λ within the parameter range $2 \leq \lambda \leq 6$, which corresponds to the typical operating range [83]. Then, we construct a POD-basis in the merge stage using these samples to create a reduced-order model.

The reduced order-model approximates the entire space-time solution ϕ of the full-order model using a solution basis \mathbf{V} for each variable. The approximation reads as

$$\phi_{u_1} \approx \mathbf{V}_{u_1} \hat{\phi}_{u_1}, \quad (5.11a)$$

$$\phi_{u_2} \approx \mathbf{V}_{u_2} \hat{\phi}_{u_2}, \quad (5.11b)$$

$$\phi_p \approx \mathbf{V}_p \hat{\phi}_p. \quad (5.11c)$$

where $\hat{\phi}$ are the reduced variables.

To investigate the amount of data required in the offline stage for constructing the reduced-order model, we employ two sets of bases $\{\mathbf{V}_{u_1}, \mathbf{V}_{u_2}, \mathbf{V}_p\}$. The two basis sets are denoted with Basis A and Basis B. Basis A is constructed with 30 samples in the offline stage. Basis B has a much lower sampling density and is constructed with 10 samples in the offline stage. In both bases, the samples are distributed with equal distances over the sampling range. Figure 5.5 depicts the distribution of the sample points with black vertical lines. Bases B is constructed at one third of the costs of Bases A.

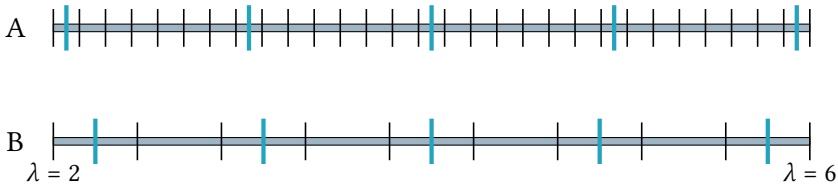


Figure 5.5: Schematical representation of the distribution of samples of solutions in the offline stage for $2 \leq \lambda \leq 6$ as black vertical lines. Sample set A contains 30 samples, whereas sample set B contains 10 samples. The reduced-order model is evaluated at the non-sampled blue vertical thick lines.

We evaluate the reduced-order model at five points covering the parameter space for both bases. In Figure 5.5 the model evaluation points are indicated with green vertical lines. The evaluation points are chosen such that their distance to the two adjacent sampling points is the longest and are denoted with $\lambda_1, \lambda_2, \lambda_3, \lambda_4$ and λ_5 . The evaluation points for Basis A are

$$[\lambda_1, \lambda_2, \lambda_3, \lambda_4, \lambda_5] = [2.07, 3.03, 4.00, 4.97, 5.93],$$

and for Basis B are

$$[\lambda_1, \lambda_2, \lambda_3, \lambda_4, \lambda_5] = [2.22, 3.11, 4.00, 4.89, 5.78].$$

We evaluate the reduced-order model using the maximum available reduced-variable size, equal to the number of samples taken in the offline stage.

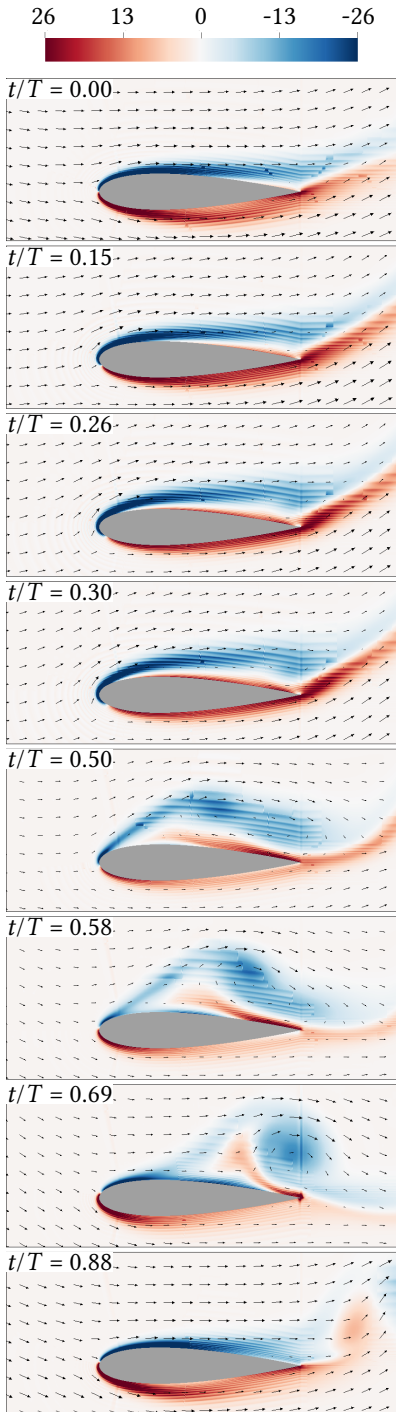
5.3 Validation using the full-order model

To ensure the correctness of the implementation of the rotating domain in a non-inertial frame of reference, introduced in 5.2, we compare our numerical results to experimental results. We compare the results computed by the full-order model, at a Reynolds number of 10^3 , to a study that explores the occurrence of dynamic stall by Le Fouest & Mulleners [82].

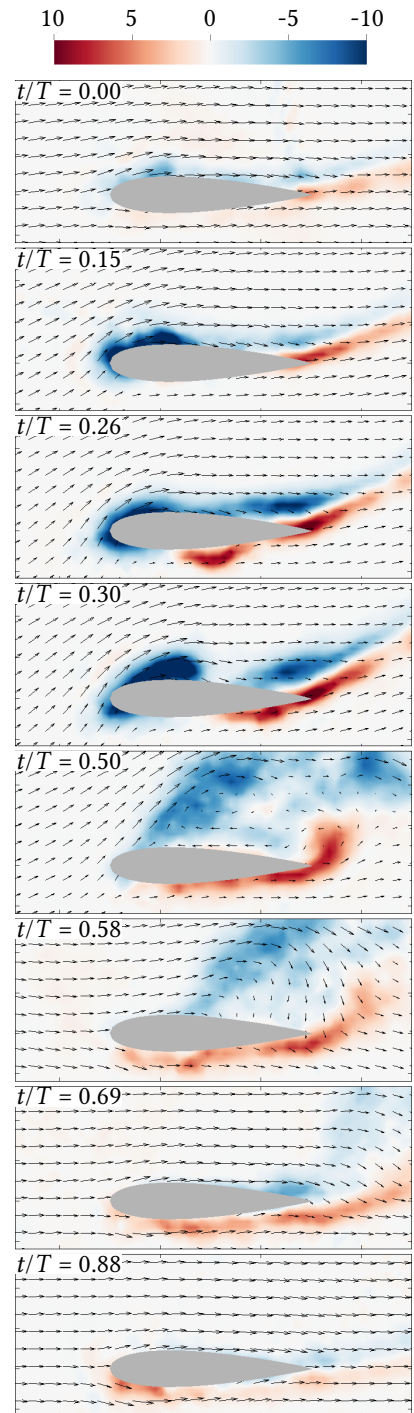
The physical experiments were conducted in a recirculating water channel using high-speed particle image velocimetry (PIV) to measure the flow field around a scaled H-type Darrieus wind turbine. The experiments focused on a single turbine blade to isolate the flow development around the blade and eliminate interactions with the wakes of other blades. For each trial, the turbine blade began at rest, oriented towards the incoming flow, and was then accelerated to its rotational speed. After five initial cycles, time-resolved PIV data were collected over 19 turbine revolutions and the results were subsequently phase-averaged. The experiments are conducted at a Reynolds number of $5 \cdot 10^4$.

We compare our numerical results with physical experiments conducted at a non-dimensional radius of $\tilde{R} = 2.5$ and a tip-speed ratio of $\lambda = 3.0$. The corresponding results are shown in Figure 5.6. At the start of its orbit, the leading edge of the blade is oriented into the flow. As the rotation begins, the effective angle of attack increases, reaching its maximum at $t/T = 0.25$. At this point, the flow begins to separate, and as the blade continues to rotate, a vortex is shed. By $t/T = 0.5$, the trailing edge is now facing into the flow, and the blade interacts with the shed vortex. As the blade rotates further, it experiences a negative angle of attack, causing the vorticity on the pressure side to increase and the flow to reattach.

In our simulations, flow separation occurs much earlier than in the experiments. While the figures provide some indication of when this separation begins, it can be challenging to pinpoint the exact moment. In the simulations, the flow remains attached only until $t/T = 0.88$, whereas in the experiments, it appears attached at $t/T = 0.00$ and during the interval $0.69 < t/T < 1$. This discrepancy is expected due to the 50-fold higher Reynolds number in the experiments. In both cases, a separation bubble first forms at the leading edge of the blade, which later connects with another separation bubble that grows from the trailing edge.



(a) full-order model, $Re = 10^3$, vis. u. VisIt [24]



(b) phys. experiment [82], $Re = 5 \cdot 10^5$

Figure 5.6: Vorticity ω_{x_3} of the flow past a vertical axis wind turbine a) computed by the full-order model and b) from experimental kindly supplied by Le Fouest & Mulleners conducted in 2022 [82] at $t/T = [0.00, 0.15, 0.26, 0.30, 0.50, 0.58, 0.69, 0.88]$. $\lambda = 3.0$, $\tilde{R} = 2.5$.

The measured and computed wake angles show close alignment for the first three time-stamps, and the onset of vortex growth occurs at approximately the same time in both cases. Despite the difference in Reynolds number between the simulations ($Re = 10^3$) and experiments ($Re = 5 \cdot 10^4$), the overall agreement in the wake shape is satisfactory. Based on these results, we can conclude that the implementation of the rotating domain is correct.

5.4 Data collected in the offline stage

We evaluate the performance of the reduced-order model using two different sampling densities during the offline stage. This provides one basis built with a large amount of data and another basis constructed with a smaller amount of data. Since the computational costs in the offline stage are directly tied to the number of samples taken, reducing the number of samples is advantageous. The goal is to provide practical insights into the model's performance when supplied with a more practical basis, with less data from the offline stage. We evaluate the reduced-order and full-order models at λ_1 , λ_3 and λ_5 as these points represent the parameter space best.

To assess the accuracy of the reduced-order model for both bases, we compute the normalized l_2 -norm of the error for the discretized solution variables. We denote the two velocity variables u_1 and u_2 , and the pressure variable p , as x . The error is defined as the difference between the full-order solution, ϕ_x , and the fully reconstructed reduced-order solution, $\tilde{\phi}_x$, across the entire space-time domain,

$$\epsilon_x = \sqrt{(\tilde{\phi}_x - \phi_x) \cdot (\tilde{\phi}_x - \phi_x)} / \sqrt{\phi_x \cdot \phi_x}. \quad (5.12)$$

Figure 5.7 presents the errors of the reduced-order model solution field compared to the full-order model for both bases. The results show a strong agreement between the reduced-order and full-order models for both Basis A and Basis B. The errors for both solution fields remain below 1%, while the pressure errors are below 3%. The average errors for each basis are indicated by black dashed lines. As expected, the average errors associated with Basis B, which has a lower sampling density, are slightly higher than those associated with Basis A, which has a higher sampling density. However, the average difference in error between the two bases is minimal.

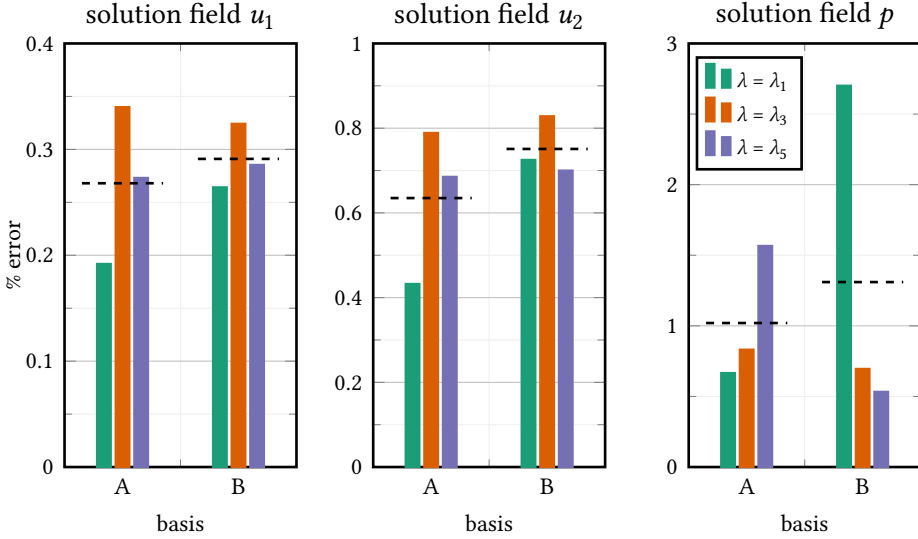


Figure 5.7: Errors of the solution fields of the reduced-order model with respect to the full-order model for variables u_1 , u_2 and p for basis A and B. The dashed lines black indicate averages of the errors per basis. $\tilde{R} = 2.5$ and $Re = 1000$.

The pressure solution shows the largest errors. In particular, for Basis B, the large error associated with λ_1 stands out. This tip-speed ratio is the most difficult to predict among those considered, due to it having the largest separation and the fact that it is represented by the smallest basis.

We evaluate the accuracy of the computed forces by determining the average error and root mean square error for each component. For a generic force F , these are computed as follows

$$\epsilon_{\text{avg}} = \frac{1}{n_f} \sum_{i=1}^{n_f} \tilde{F}^h(t_i) - F^h(t_i), \quad (5.13)$$

$$\epsilon_{\text{RMS}}^2 = \frac{1}{n_f} \sum_{i=1}^{n_f} (\tilde{F}^h(t_i) - F^h(t_i))^2. \quad (5.14)$$

Here, \tilde{F} represents the force computed by the reduced-order model in either the x_1 or x_2 direction, while F denotes its counterpart from the full-order model. The number

of samples on which the force is evaluated is denoted by n_f . We non-dimensionalize the error with the range of the data, such that

$$\epsilon_{\text{navg}} = \frac{\epsilon_{\text{avg}}}{\Delta F}, \quad (5.15)$$

$$\epsilon_{\text{nRMS}} = \frac{\epsilon_{\text{RMS}}}{\Delta F}. \quad (5.16)$$

Figure 5.8 presents the average and root mean square errors of the forces computed by the reduced-order model in comparison to the full-order model. The errors for both Basis A and Basis B fall within the acceptable range, with $\epsilon_{\text{nRMS}} < 1.1\%$ and $\epsilon_{\text{navg}} < 10\%$ of the range of the data. For the forces in the x_1 direction, the errors are of similar magnitude for both bases. However, in the x_2 direction, the accuracy of the force predictions deteriorates more significantly, indicating that forces in this direction are more challenging to predict accurately with a basis with less information. These errors decrease as λ increases. This is because higher tip-speed ratios have less flow separation which is better captured on the basis with less information.

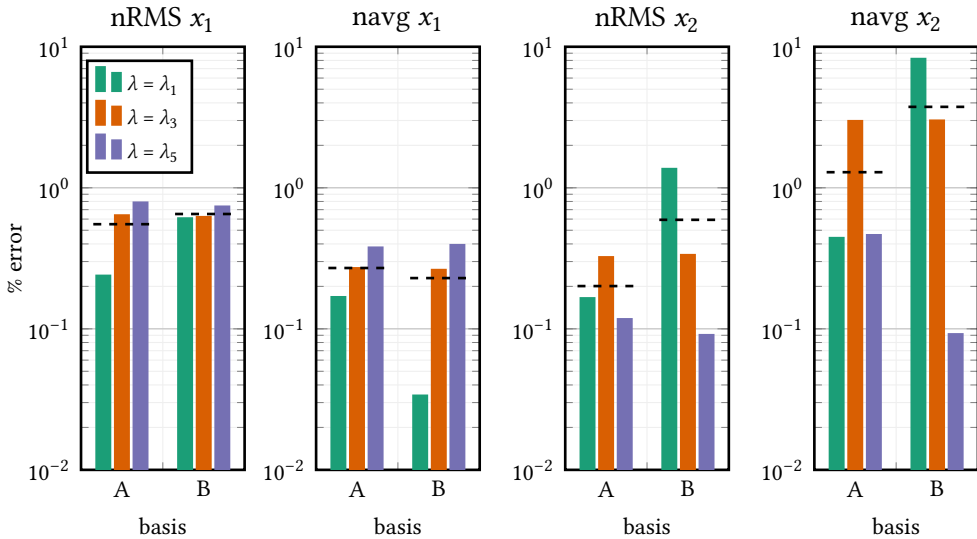


Figure 5.8: Normalized root mean square error and average error of the forces computed by the reduced-order model with respect to the full-order model for basis A and B. The dashed black lines indicate averages of the errors per basis. $\bar{R} = 2.5$ and $\text{Re} = 1000$.

The typical speed-up, defined as

$$\text{speed-up} = \frac{\text{wall-clock time FOM}}{\text{wall-clock time ROM}}. \quad (5.17)$$

is $\mathcal{O}(70)$ for both bases, which is considerably lower than the speed-up of 800 reported in previous work [89]. This discrepancy is primarily due to the full-order model being faster in the current study, owing to the lower number of control points used in the discretisation. The computational cost of evaluating the reduced-order model remains comparable, with a typical wall-clock time of $\mathcal{O}(3)$ minutes on 32 cores.

The performance of both Basis A and Basis B is comparable. However, given the lower computational costs in the offline stage associated with Basis B, we choose to use Basis B for further computations.

5.5 Tip-speed ratio study

We study the forces, power, and flow fields computed by the reduced-order model for the tip-speed ratios λ_1 , λ_2 , λ_3 , λ_4 and λ_5 to assess the performance of the vertical axis wind turbina at $\text{Re} = 1000$. We align the force vectors with the axis system in Figure 5.3. The orientation of the force vectors is depicted in Figure 5.9.

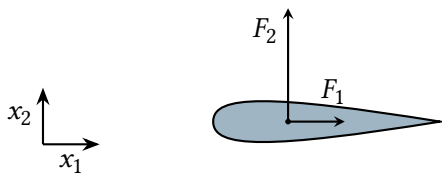


Figure 5.9: Orientation of the force vectors in the rotating domain in Figure 5.3.

Figure 5.10 depicts the force coefficients computed by the reduced-order and full-order models. The force coefficients are defined as

$$C_x = \frac{F}{\frac{1}{2} \rho U_b^2 c}, \quad (5.18)$$

with density ρ . We use the blade velocity $U_b = \omega \cdot R$ as reference velocity instead of U_∞ to make the force coefficient independent of the tip-speed ratio λ . The computed forces from the reduced-order model show good agreement with those from the full-order model. The only exception occurs at the lowest value of λ , denoted as λ_1 , where the reduced-order model slightly deviates in its prediction of the vertical force coefficient.

The turbine blade generates thrust only for a brief period at the two lowest tip-speed ratios, λ_1 and λ_2 . Here, the interaction of the produced vortex with the blade

gives a net thrust for a short moment. For higher tip-speed ratios, the blade is unable to overcome drag and thus does not produce thrust at all. This behavior may be attributed to the low Reynolds number considered in the analysis. Since the flow remains separated for almost the entire rotation of the blade, the drag is large.

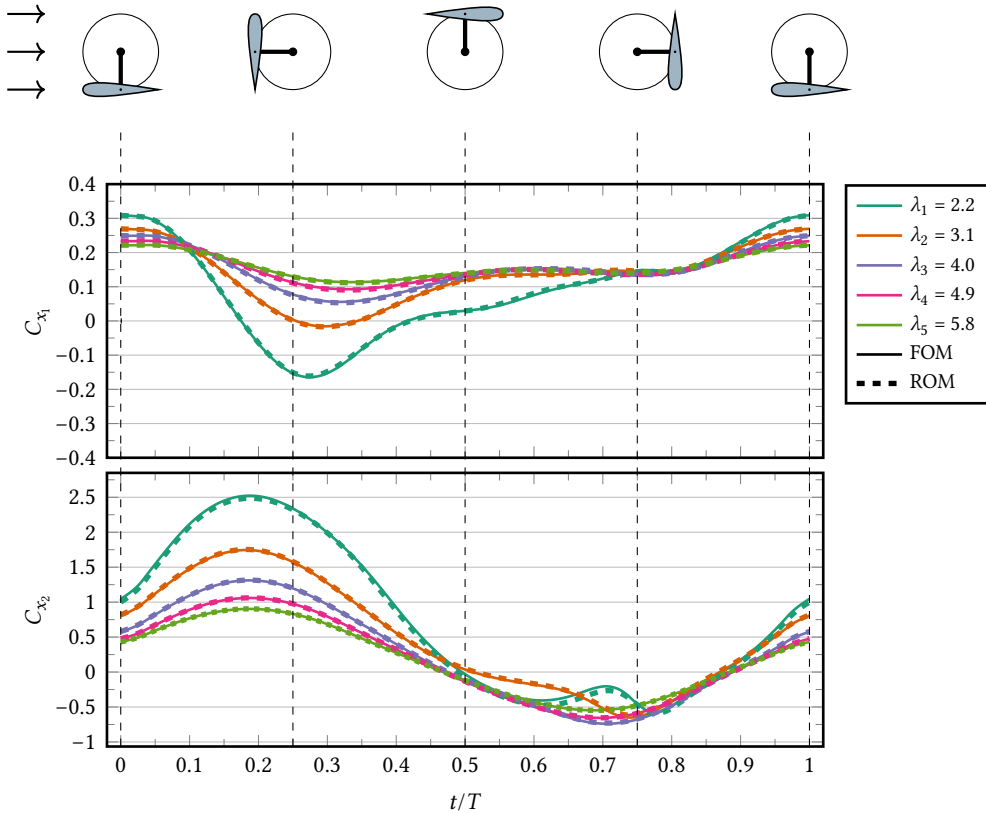


Figure 5.10: Force coefficients computed by the reduced-order model and full-order model. Computed with basis B. $\bar{R} = 2.5$ and $\text{Re} = 1000$.

Figures 5.11 and 5.12 visualize the flow development during a full cycle of the blade for tip-speed ratios $\lambda_1 = 2.2$ and $\lambda_2 = 3.1$. For both tip-speed ratios, the separation bubble begins to grow at $t/T = 0$. The flow is separated for almost the entire rotation of the blade. A vortex is shed at $t/T = 3/8$ for the blade with λ_1 , while for the blade with λ_2 , it is shed slightly later at $t/T = 4/8$. Additionally, the separation bubble for the blade with λ_2 is smaller and grows further downstream on the blade. This trend continues as λ increases beyond λ_2 . By comparing Figure 5.11 with Figure 5.10, we observe that the highest thrust is generated just before the separation bubble is shed.

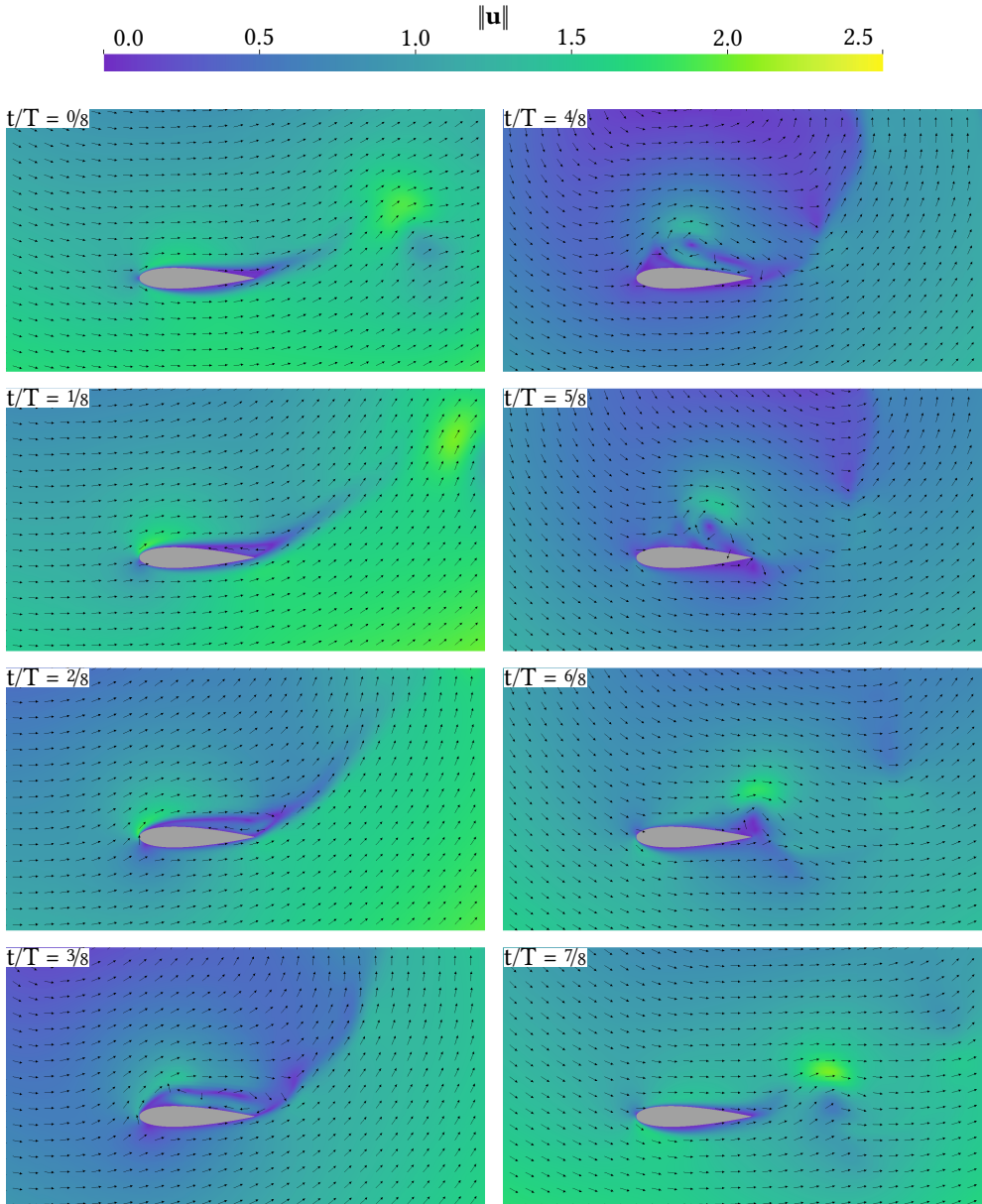


Figure 5.11: Magnitude of the velocity $\|\mathbf{u}\|$ for $\lambda_1 = 2.2$ computed by the reduced-order model at $t = 0$, $t = \frac{1}{4}T$, $t = \frac{2}{4}T$, $t = \frac{3}{4}T$ using basis B. $\tilde{R} = 2.5$ and $\text{Re} = 1000$. Visualized using VisIt [24].

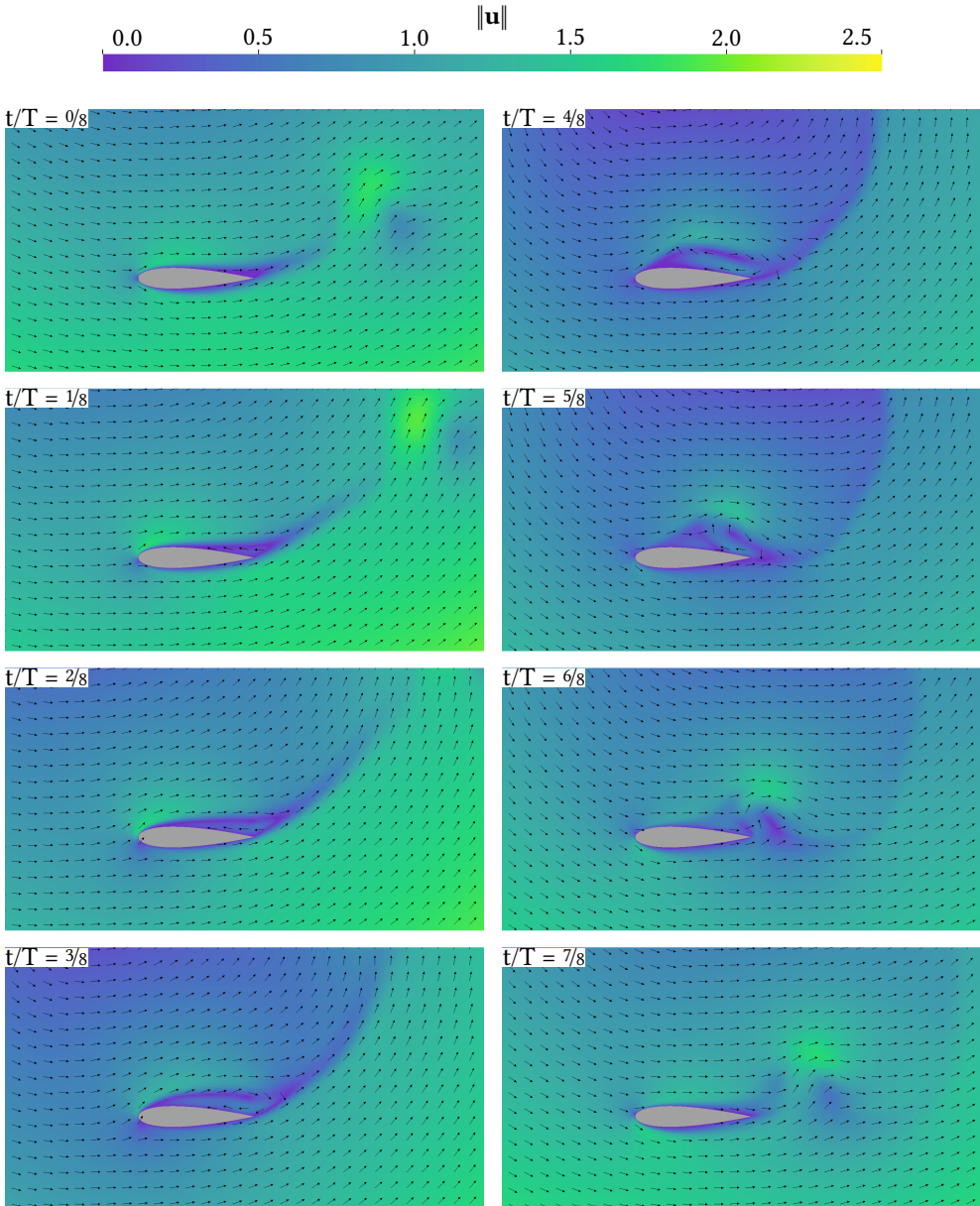


Figure 5.12: Magnitude of the velocity $\|\mathbf{u}\|$ for $\lambda_2 = 3.1$ computed by the reduced-order model at $t = 0$, $t = \frac{1}{4}T$, $t = \frac{2}{4}T$, $t = \frac{3}{4}T$ using basis B. $\tilde{R} = 2.5$ and $\text{Re} = 1000$. Visualized using VisIt [24].

5.6 Optimisation of tip-speed-ratio for energy production

We investigate the energy production of the single-bladed vertical axis wind turbine over a full operational cycle. The objective is to demonstrate that the reduced-order model can be effectively utilized to optimize the turbine's performance for chosen flow and operation conditions. We evaluate the reduced-order model at $Re = 1000$ and $\tilde{R} = 2.5$.

We evaluate the energy produced by the turbine using the energy coefficient, which is defined as

$$C_E = \frac{1}{T} \int_0^T C_P(t) dt. \quad (5.19)$$

Here, the power coefficient $C_P(t)$ is given by

$$C_P(t) = \frac{P(t)}{\frac{1}{2} \rho U_b^3 c} \quad (5.20)$$

where the power $P(t)$ is computed as $P(t) = F(t) \cdot U_b$. It is important to note that due to the forward motion of the blade, U_b is negative in the coordinate system shown in Figure 5.9. The energy coefficient is similar to the average of the produced power over one cycle.

Figure 5.13 gives the energy coefficient calculated by the reduced-order model. The model is evaluated at 81 linearly spaced points within $2 \leq \lambda \leq 6$ resulting in a

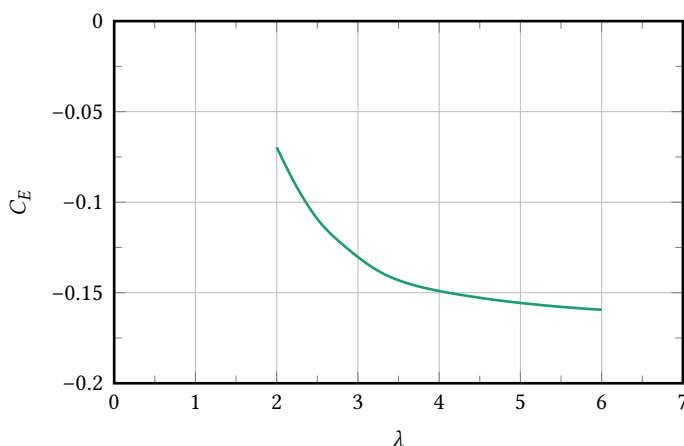


Figure 5.13: Produced energy by the blade of the vertical axis wind turbine as a function of tip-speed ratio λ . $\tilde{R} = 2.5$ and $Re = 1000$.

resolution of $\Delta\lambda = 0.05$. This accuracy is considered small enough for our purposes. The cost of the online stage is equivalent to 1.16 full-order model evaluations. As a result, the total cost of creating and evaluating the reduced-order model for all the data points is comparable to that of 11.16 full-order model evaluations.

The produced energy is negative across the entire range of tip-speed ratios studied under the chosen flow conditions, indicating that the turbine blade consumes more energy than it generates. This outcome may be influenced by the specific flow conditions, such as the selected Reynolds number and other operating conditions of the turbine. The flow past the turbine blade is separated for almost the entire rotation of the blade, giving a high drag. This can be seen in Section 5.3 and Section 5.5. The reduced-order model identifies the optimal operating point at the lowest tip-speed ratio within the studied range, $\lambda = 2.0$.

5

5.7 Conclusions

This chapter has investigated the application of a time-periodic reduced-order model to the flow past single-bladed vertical-axis wind turbines at a Reynolds number of 1000. We found that the reduced-order model can achieve high accuracy with less data during the offline stage compared to earlier work. Using 10 samples of the full-order model instead of 30, all errors were smaller than 10%. However, most of the errors were smaller than 1%.

We examined the flow characteristics of the vertical-axis wind turbine as a function of the tip-speed ratio using the reduced-order model. At the two lowest tip-speed ratios, λ_1 and λ_2 , the turbine blade generates thrust only briefly, driven by the interaction between the shed vortex and the blade. However, at higher tip-speed ratios, the blade is unable to overcome drag, and does not produce thrust. This outcome is likely due to the low Reynolds number used in the analysis, where the flow remains separated for nearly the entire blade rotation, leading to increased drag.

We have also used the reduced-order model to determine the optimal operating point of the vertical-axis wind turbine, where it generates the maximum energy per cycle. The produced energy is negative, this results from the used Reynolds number.

The work in this chapter is an initial step toward industrial application of the time-periodic reduced-order model. The current work can be extended by including the parameters angle of attack, tip-speed ratio, and non-dimensional radius at a higher Reynolds number into one model. This would allow a comprehensive analysis of a vertical-axis wind turbine and identification of its optimal parameters. Ad-

ditionally, this study did not address the interaction between the fluid and the structure of the blade, which could be beneficial for understanding potential instabilities such as flutter. The motion of the blade can easily be incorporated into this model by enforcing a motion to Equation (5.4c).

6

Conclusions

In this dissertation we have studied techniques to analyze time-periodic flows. In the introduction we have introduced two research goals. In this chapter we reflect on these goals and outline future work.

6.1 Conclusions

We have defined the first goal as:

(i) Develop an efficient and accurate model for analysis of time-periodic flows that effectively handles the costly transients inherent in these flows.

We have introduced a high-fidelity model (full-order model) specifically tailored for time-periodic flow in Chapter 2. By employing a space-time isogeometric analysis discretisation, where space and time are treated analogously, we achieved higher-order smoothness in space and time. The time-periodicity constraint was enforced as a periodic boundary condition in time, transforming the original initial value problem into a boundary value problem in both space and time.

The method ensures that the flow is exactly periodic, avoiding the need for excessively long time domains. For non-turbulent flows, time-periodic approximation does not introduce a modelling error. However, for turbulent flows, a modeling error may be induced.

To model turbulence, we utilized residual-based variational turbulence modeling. Additionally, weak boundary conditions were employed to enhance accuracy near the moving boundaries of the computational domain. We demonstrated the conservation properties of the formulation and used a conservative traction evaluation method. To address challenges related to the saddle-point nature of the under-

lying problem, we adopted pseudo-transient continuation and employed artificial compressibility, both of which contributed to reducing simulation time.

We successfully simulated flow past periodically moving objects. Numerical experiments on stationary and moving hydrofoils demonstrated good accuracy, with calculated drag and lift coefficients aligning with established results in the literature and correctly capturing the history effects of the wake.

The second goal of this thesis is stated as follows:

(ii) Develop a cost-efficient and accurate reduced-order model for the analysis of time-periodic flows.

In Chapter 3, we implemented a time-periodic reduced-order model. This projection-based reduced-order model was constructed using a time-periodic basis computed via proper orthogonal decomposition (POD) of a snapshot matrix containing high-fidelity solutions for a parameter of interest.

The reduced-order model performed well in cases of moving hydrofoils, where we varied the Strouhal number, Reynolds number, and heave motion profile. The solution fields and post-processed forces of the reduced-order model showed strong agreement with those of the full-order model, while the dimension of the solution vector was reduced from $\mathcal{O}(10^6)$ to $\mathcal{O}(10^2)$.

The reduced-order model exhibited predictable behavior, with errors converging to zero as the size of the reduced basis increased. In a case where 30 full-order model solutions were sampled to construct a POD basis, the errors in drag and lift forces were both below 0.2% with respect to the full-order model.

In Chapter 5, we took a first step towards industrial application of the time-periodic reduced-order model by applying it to the flow past single-bladed vertical-axis wind turbines at a Reynolds number of 1000. Constructing the basis with fewer samples, 10 instead of 30, still yielded accurate results. Most errors were below 1%, with none exceeding 10% of the range of the force signal. This level of accuracy demonstrates the model's suitability for a wide range of time-periodic flow computations. We demonstrated how the model can identify the optimal operating point of the vertical-axis wind turbine under specific flow conditions.

Despite the success of the reduced-order model, its complexity still scales with the size of the full-order model, preventing real-time evaluation. To address this bottleneck, we implemented a hyper-reduced model using empirical interpolation method hyper-reduction techniques.

In Chapter 4, we evaluated the hyper-reduced model on a case with steady two-dimensional flow. The model achieved errors of $\mathcal{O}(0.01\% - 10\%)$ with respect to the full-order model. The speed-up of the hyper-reduced model compared to the full-order model was $\mathcal{O}(10^5)$, with a speed-up of $\mathcal{O}(10^3)$ compared to the reduced-order model.

We were unable to evaluate the hyper-reduced model for time-periodic flow successfully.

6.2 Outlook

Looking ahead, there are several interesting directions for future research.

First, extending the model to three spatial dimensions would greatly enhance its applicability. This extension would require solving a four-dimensional boundary value problem, requiring four-dimensional meshes. To avoid the prohibitively expensive offline stages associated with such high-dimensional problems, mesh adaptivity could play an important role. Mesh adaptivity dynamically adjusts the mesh resolution, refining it in areas that demand more detailed discretization. This approach reduces computational cost and improves accuracy by focusing resources where they are most needed. In the context of isogeometric analysis, implementing mesh adaptivity would involve techniques such as Immersogeometric analysis [56, 69] or truncated splines [49, 50].

We were unable to fully evaluate the hyper-reduced model for time-periodic flows. Future research could address this limitation by exploring methods like the empirical quadrature procedure [146] or developing neural network-based reduced-order models [72, 84, 118], including those that employ autoencoders.

Currently, the hyper-reduced model was implemented using hyper-reduction in a finite element context, involving a projection of the problem onto a finite element space. Applying hyper-reduction techniques directly within isogeometric discretizations could offer significant advantages.

Whereas we have provided an initial step towards industrial application, additional verification for higher Reynolds numbers makes the more model suitable for these. Additionally, extending the model to other industrial problems, such as optimizing the performance and layout of wind farms or ship propellers, could bridge the gap between the theoretical developments in this work and practical engineering solutions.

Finally, it may not be necessary to create the time-periodic reduced-order model using data from a time-periodic full-order model. Instead, time-periodic data from standard full-order models could be projected onto the time-periodic full-order model to generate a time-periodic basis. Further research in this direction could broaden the applicability of the time-periodic reduced-order model.

Result reproduction

The results presented in this thesis can be reproduced using the delFI code, which stands for Delft Finite-element and Isogeometric-analysis. DelFI is designed to enable the easy implementation of various differential equations that describe specific physical phenomena. As a result of this thesis, DelFI now also supports projection-based reduced-order modeling.

The code relies heavily on two libraries: MFEM and libROM. MFEM is an open-source library for finite element methods and isogeometric analysis, while libROM is an open-source software library specifically designed to facilitate model order reduction.

The results in this thesis can be reproduced with the versions of delFI, MFEM and libROM specified in the table below. The code can be installed by running `deploy.sh` in the `rom-dev` branch of DelFI. The required software is stated in the beginning of this file. The input files required to reproduce the results in these thesis are stored at <https://doi.org/10.4121/47d91912-0773-4f96-bcb0-596acc46ac37>.

The results can be plotted with Visit 3.4.1 as a minimum version. Postprocessing scripts can be found at <https://github.com/JacobLotz/ppdelfi>.

| Name | Version | Branch | Git hash |
|--------|---------|--------------------|--|
| DelFI | | rom-dev | 0ea9e286ce75b74ced4e89a85c72d848c9d120d0 |
| MFEM | 4.6 | | |
| libROM | | impl-cmake-install | d61d063af1065f132a710c84cdce46b715b9c05f |

Table: Required versions of the software for result reproduction.

Curriculum Vitæ

Jacob Evert Lotz

19-01-1995 Born in Wageningen, The Netherlands.

Education

- 2007–2013 Voorbereidend Wetenschappelijk Onderwijs (VWO)
R.S.G. Pantarijn Wageningen
- 2013–2017 Bachelor of Science in Maritime Engineering
Technische Universiteit Delft
- 2017–2020 Master of Science in Maritime Engineering (*cum laude*)
Technische Universiteit Delft
Thesis: Takeoff of a hydrofoil vessel in Panship
Supervisors: Dr. ir. I. Akkerman
 F. M. Montero
- 2020–2024 PhD. Ship Hydromechanics
Technische Universiteit Delft
Thesis: Reduced-order modelling of time-periodic flows
Promotor: Prof. dr. G.D. Weymouth
Co-promotor: Dr. ir. I. Akkerman

Other Experience

- 2015–2015 Treasurer
Nederlandse Jeugdbond voor Natuurstudie
- 2016–2017 Business development
MOCS B.V

Conference Contributions

- 2024 **16th World Congress on Computational Mechanics**
Presentation
*Reduced-order modelling of exact periodic flows,
using a space-time discretisation*
- 2024 **G+smo developer days**
Presentation
*Computation and Reduced Order Modelling of Periodic Flows,
with applications to lift control of hydrofoils*
- 2023 **MFEM Workshop**
Presentation
Computation and reduced order modeling of periodic flows
- 2023 **Research School on Reduced-order Modelling and Mesh
Adaptivity, Nottingham 2023**
Poster
Plans for reduced order modelling of time-periodic flows
- 2023 **22nd Computational Fluids Conference**
Presentation
A space-time framework for periodic flows
- 2021 **23rd Numerical Towing Tank Symposium**
Presentation and extended abstract
*Space-time simulation of a heaving and pitching foil with
exact enforcement of time periodicity*
- 2021 **9th Conference on Computational Methods in
Marine Engineering**
Presentation
*Space-time simulation of a heaving hydrofoil with enforcement
of time periodicity*
- 2021 **16th U.S. National Congress on Computational Mechanics**
Presentation
*Space-time simulation of a heaving and pitching foil with
time periodicity*

List of Publications

Part of this thesis:

- **J. E. Lotz**, M. F. P. ten Eikelder & I. Akkerman (2024). “Space–time computations of exactly time-periodic flows past hydrofoils”, in *Computers & Fluids*, 277:106–286,
- **J. E. Lotz**, G. D. Weymouth & I. Akkerman (2024). “Projection-based reduced-order modelling of time-periodic problems, with application to flow past flapping hydrofoils”, *Computer Methods in Applied Mechanics and Engineering*, 429:117–161,

Not part of this thesis:

- Michel Touw, **J. E. Lotz**, & I. Akkerman (2020). “Analysis of a hydrofoil craft with a suspension system”, in *Proceedings of the 12th Symposium on High Speed Marine Vehicles*, Volume 5: HSMV 2020 69,

List of Open Source Contributions

As part of this thesis, the following contributions to open-source C++ software libraries have been made.

MFEM

MFEM is an open-source C++ library designed for the development of scalable finite element method (FEM) simulations. It provides a flexible, modular (M) framework for implementing a wide range of FEM-based numerical simulations, from basic linear problems to complex, multi-physics systems. The contributions are made to enhance the isogeometric analysis extension. The pull requests are:

- 3226: NURBS patch 2D rotation functions
- 3232: NURBS curve interpolation functions
- 3238: Fix bug in comparing two doubles in knot vector comparison
- 3404: NURBS auto knot2edge and free patch orientation
- 3419: NURBS C-mesh foil section miniapp
- 3577: Fix NURBS print functions
- 3604: NURBS discontinuity functions
- 3659: Fix make file of nurb-interp-dev
- 3669: Fix GridFunctionCoefficient::Eval
- 3803: Fix GenerateElementDofTable for parallel periodic NURBS
- 3857: Fix NURBSExtension::ConnectBoundaries3D

libROM

The libROM library is an open-source software library designed to facilitate model order reduction in computational simulations. libROM implements several popular model order reduction techniques, such as Proper Orthogonal Decomposition, Reduced Basis Methods, and data-driven approaches like Dynamic Mode Decomposition. The library is designed to handle large-scale simulations, making it suitable for high-performance computing environments. The pull requests are:

- 196: Const vector print function
- 233: Fix cmake for installation

Acknowledgements

This work would not have been possible without the support of others. Here, I would like to take the opportunity to thank my team. I start with thanking my daily supervisor and co-promotor Ido Akkerman. Thank you for your support and endless stream of new ideas through this journey. Thank you for introducing me to high-performance computing and high-fidelity numerical methods. You have opened up an entirely new world for me, one I might never have discovered by myself. Next, I would like to thank my promotor, Gabe Weymouth. Your guidance undoubtedly helped me a lot. I am very grateful for your help when it was much needed, and your effort to understand my work in a short period of time. I would also like to thank my former promotor, Tom van Terwisga, for your support and for forcing me to place my work in a wider perspective.

Marco ten Eikelder deserves gratitude for patiently introducing me to VMS methods and for his excellent co-authorship of the first chapter of this thesis. Thank you, I have learned a lot from you! My colleagues in ship hydromechanics deserve recognition for their valuable feedback on my work and our fruitful conversations on (computational) fluid mechanics and surrogate modelling. Anna Boon, Marin Lauber, Manuel Cabral, Jordi Poblador and Tzu-Yao Huang, Bernat Font, Jonah Massey, Sankalp Jena, Guillaume Ricard, Sanne van Essen, and Nico Valle Marchante I enjoyed our discussions and the many beers we shared!

I also want to thank my office mates for providing pleasant distractions from work and our many conversations over coffee. Special thanks go to Hanna Pot for her care and down to earth point of view of PhD life, Hugo Verhelst for introducing me to his warm network of European scientists and his encouraging words towards the end of his PhD, Martin van der Eijk for all the laughs we had and Filippo Riccioli for our thoughtful discussions. I thank Jesper Zwaginga for his fresh perspective on the world; you helped me put many of my thoughts into perspective. I would like to thank Peter Wellens for our debates on a wide range of topics and for introducing me to some theory on philosophy. Although the primary focus of my colleagues at the towing tank was on physical experiments, your input and ideas were always valuable or an interesting distraction. Thank you! I would like to thank the management staff, and especially our Ship Hydromechanics managing hero Tessa for providing a very smooth ride during this journey.

Special thanks goes to the participants of the JJJ-summits. Jacques and Jae, it is more than great to spend time with you! Sébastien Le Fouest and Karen Mulleners, thank you for kindly providing the data of your (physical) experiments on vertical-axis wind turbines.

Berend, you are a great friend and I am very grateful for your unwavering support throughout this PhD journey. Thank you! Arjan, I thoroughly enjoy our running lunch breaks and the meaningful conversations we share. Thank you! I would like to thank my study buddy, Michiel Bicker, for the vast amount of time we have spent together finishing all those assignments. I probably wouldn't be here without you! I also want to extend my gratitude to all my friends in the Waldorf group, with a special shout-out to Kristel, for their kind care and support. To all my birding friends, especially Daan, Jurriën, Ruben, and Pieter - thank you for taking me on birding trips, even when my mind was still full of equations and computer code.

Last, I would like to thank my family. To my parents, Judica and Bert, and my sister Anna—your support has been boundless, and I could not have accomplished this without you. Most importantly, I thank Savanne for always standing by my side. You brighten even the darkest of winter days.

Summary

This thesis explores fast simulation of time-periodic flows, characterized by behavior that repeats at regular intervals. These flows are present in both natural and engineered systems. Examples include flows past wind turbines, in the heart and arteries, and around propellers. Due to their long time domains, time-periodic flows pose challenges in both experimental and numerical studies. Many engineering tasks, like optimization, require numerous model evaluations across a wide range of inputs. We need a fast and accurate model to directly interact with the model in the design process. To contribute to this goal, we first develop a high-fidelity method specifically designed for time-periodic flows. Using this model, we then create a time-periodic reduced-order model to enhance simulation efficiency.

In the high-fidelity model, we employ the isogeometric analysis framework to achieve higher-order smoothness in both space and time. The discretization is performed using residual-based variational multiscale modelling and weak boundary conditions are adopted to enhance the accuracy near the moving boundaries of the computational domain. We enforce the time-periodic boundary condition within the isogeometric discretization spaces, which converts the two-dimensional time-dependent problem into a three-dimensional boundary value problem. The motion is known a priori and we restrict ourselves to two spatial dimensions. Application of the computational setup to heaving and pitching hydrofoils displays very accurate and exactly periodic results for lift and drag.

We use the high-fidelity model to develop a POD-Galerkin reduced-order model, which retains inherits the features of the high-fidelity model while reducing the number of variables in both space and time. We evaluate the reduced-order model with numerical experiments on moving hydrofoils. Reduced-order model solutions agree well with those of the high-fidelity model. The errors over the entire time period of the computed forces are less than 0.2%. Our time-periodic reduced-order model offers speed-ups ranging from $\mathcal{O}(10^2)$ - $\mathcal{O}(10^3)$ compared to the full-order model.

The non-linear nature of the Navier-Stokes equations creates a computational bottleneck in the reduced-order model. We explore hyper-reduction techniques to mitigate these challenges. We focus on empirical interpolation methods, which have

shown promise in reducing the complexity of non-linear operators. The model performed well for the experiment with steady flow, with force and solution errors ranging from $\mathcal{O}(0.01\% - 10\%)$, depending on the sampling method. The hyper-reduced model achieves a speed-up of $\mathcal{O}(10^5)$ compared to the full-order model, and $\mathcal{O}(10^3)$ compared to the reduced-order model. This enables real-time computations with direct interaction of the user. However, the hyper-reduced model could not provide a solution for the time-periodic flow experiment.

To show the applicability of the reduced-order model to an industrial problem, we apply the the model to a vertical axis wind turbine. Vertical-axis wind turbines offer significant advantages for urban applications over conventional wind turbines due to their lower noise levels. However, their performance is highly sensitive to various factors requiring high-fidelity simulations to optimize its performance. The model was used to determine the optimal operating point of the turbine, maximizing energy production per cycle under the given conditions. It was observed that the turbine's energy output was negative, likely due to the low Reynolds number ($\Re = 1000$) used in this study.

Future research can expand on this thesis in several ways. Extending the model to three spatial dimensions would require solving four-dimensional boundary value problems, potentially benefiting from mesh adaptivity techniques. Further exploration of hyper-reduction methods, such as empirical quadrature procedures or neural network-based models, could enhance the model's efficiency. Applying hyper-reduction directly within isogeometric discretizations may also offer significant advantages. Additionally, further verification for higher Reynolds numbers and adaptation to other industrial applications, like wind farm and ship propeller optimization, could bridge the current theoretical advances with practical use. Finally, using time-periodic data from standard models to develop time-periodic reduced-order models could expand their applicability.

Samenvatting

Dit proefschrift onderzoekt snelle simulatie van tijds-periodieke stromen. Deze stromen worden gekenmerkt door gedrag dat zich op regelmatige intervallen herhaalt en komen zowel voor in natuurlijke als in technische systemen. Voorbeelden zijn stroming langs windturbines, in het hart en de slagaders, en rondom propellers. Door hun lange tijdsdomeinen zijn tijds-periodieke stromen uitdagend in zowel experimentele als numerieke studies. Veel engineeringtaken, zoals optimalisatie, vereisen talrijke model evaluaties over een breed scala aan invoerwaarden. Met dit model moeten we direct kunnen communiceren in het ontwerpproces. Hiervoor hebben we een snel en accuraat model nodig. Om bij te dragen aan dit doel, ontwikkelen we eerst een model met hoge precisie die specifiek is ontworpen voor tijds-periodieke stromen. Met dit model creëren we vervolgens een tijds-periodiek gereduceerd-orde model om de efficiëntie van de simulatie te verbeteren.

In het precieze model passen we het isogeometrische analyse toe om zo een hogere orde van gladheid in zowel ruimte als tijd te krijgen. De discretisatie wordt uitgevoerd met behulp van “residual-based variational multiscale modelling” en zwak opgelegde randvoorwaarden om de nauwkeurigheid nabij de bewegende randen van het rekendomein te verbeteren. We leggen de tijds-periodieke randvoorwaarde op in de isogeometrische discretisatie-ruimten, waardoor het twee-dimensionale tijdsafhankelijke probleem wordt omgezet in een drie-dimensionaal randwaardeprobleem. De beweging is van tevoren bekend en we beperken ons tot twee ruimtelijke dimensies. Toepassing van het model op bewegende vleugels levert zeer nauwkeurige en exact periodieke resultaten op voor lift en weerstand.

We gebruiken het precieze model om een POD-Galerkin gereduceerd-orde model te ontwikkelen, dat de eigenschappen van het precieze model behoudt, terwijl het aantal variabelen in zowel ruimte als tijd sterk wordt verminderd. We testen het gereduceerd-orde model met numerieke experimenten op bewegende vleugel secties. De oplossingen van het gereduceerd-orde model komen goed overeen met die van het precieze model. De fouten over de gehele tijdsperiode van de berekende krachten zijn minder dan 0.2%. Ons tijds-periodiek gereduceerd-orde model biedt versnellingen in rekentijd variërend van $\mathcal{O}(10^2)$ tot $\mathcal{O}(10^3)$ vergeleken met het precieze model.

De niet-lineaire aard van de Navier-Stokes-vergelijkingen creëert een computationeel knelpunt in het gereduceerd-orde model. We verkennen het gebruik van hyper-reductietechnieken om deze knelpunten te omzeilen. We gebruiken “empirical interpolation methods”, die veelbelovend zijn in het verlagen van de complexiteit van niet-lineaire operatoren. Het model presteerde goed voor het niet tijdsafhankelijke experiment met constante stroom. Hier variëerde de kracht- en oplossingsfouten van $\mathcal{O}(0.01\% - 10\%)$. Het hyper-gereduceerde model bereikt een versnellingen in rekentijd van $\mathcal{O}(10^5)$ vergeleken met het volledige model, en $\mathcal{O}(10^3)$ vergeleken met het gereduceerd-orde model. Dit maakt realtime berekeningen en directe interactie van de ontwerper met het model mogelijk. Het hyper-gereduceerde model kon echter geen oplossing vinden voor het tijds-periodieke stroomexperiment.

Om de toepasbaarheid van het gereduceerd-orde model op een industrieel probleem aan te tonen, passen we het model toe op een windturbine met een verticale turbine as. Windturbines met een verticale turbine as bieden aanzienlijke voordelen voor stedelijke toepassingen ten opzichte van conventionele windturbines vanwege hun lagere geluidsniveaus. Hun prestaties zijn echter zeer gevoelig voor verschillende factoren, wat precieze simulaties vereist om de prestaties te optimaliseren. Het model werd gebruikt om het optimale werkpunt van de turbine te bepalen, waarbij de energieproductie per cyclus onder de gegeven omstandigheden werd gemaximaliseerd. Hierbij was de geproduceerde energie van de turbine negatief, waarschijnlijk door het lage Reynolds-getal ($\Re = 1000$) dat in deze studie werd gebruikt.

Toekomstig onderzoek kan op verschillende manieren verder bouwen op dit proefschrift. Het uitbreiden van het model naar drie ruimtelijke dimensies zou vereisen dat vier-dimensionale randwaardeproblemen worden opgelost, waarbij mogelijk profijt kan worden getrokken uit “mesh adaptivity” technieken. Verdere verkenning van hyper-reductie methoden, zoals “empirical quadrature” procedures of op neurale netwerken gebaseerde modellen, zou de efficiëntie van het model kunnen verbeteren. Toepassing van hyper-reductie direct in isogeometrische discretisaties kan ook aanzienlijke voordelen bieden. Bovendien zou verdere verificatie voor hogere Reynolds-getallen en toepassen op andere industriële toepassingen, zoals optimalisatie van windparken en scheepspropellers, de huidige theoretische vooruitgang kunnen verbinden met praktische toepassingen. Ten slotte zou het gebruik van tijds-periodieke gegevens van conventionele modellen om tijds-periodieke gereduceerd-orde modellen te ontwikkelen, hun toepasbaarheid kunnen uitbreiden.

Bibliography

- [1] I. Abbott & A. Von Doenhoff (1959). *Theory of wing sections, including a summary of airfoil data*. Dover Publications. ISBN 978048660586.
- [2] I. Akhtar, A. H. Nayfeh & C. J. Ribbens (2009). “On the stability and extension of reduced-order Galerkin models in incompressible flows: A numerical study of vortex shedding”. *Theoretical and Computational Fluid Dynamics*, **23**:213–237.
- [3] R. Anderson, J. Andrej, A. Barker, J. Bramwell, J. Camier, J. Cervený, V. Dobrev, Y. Dudouit, A. Fisher, T. Kolev, W. Pazner, M. Stowell, V. Tomov, I. Akkerman, J. Dahm, D. Medina & S. Zampini (2021). “MFEM: A modular finite element methods library”. *Computers and Mathematics with Applications*, **81**:42–74.
- [4] P. Astrid, S. Weiland, K. Willcox & T. Backx (2008). “Missing point estimation in models described by proper orthogonal decomposition”. *IEEE Transactions on Automatic Control*, **53**:2237–2251.
- [5] J. Baiges, R. Codina, I. Castañar & E. Castillo (2020). “A finite element reduced-order model based on adaptive mesh refinement and artificial neural networks”. *International Journal for Numerical Methods in Engineering*, **121**:588–601.
- [6] E. Bainomugisha, A. Carreton, T. van Cutsem, S. Mostinckx & W. de Meuter (2013). “A survey on reactive programming”. *ACM Computing Surveys*, **45**:1–34.
- [7] G. Balducci, B. Chen, M. Möller, M. Gerritsma & R. de Breuker (2022). “Review and perspectives in quantum computing for partial differential equations in structural mechanics”. *Frontiers in Mechanical Engineering*, **8**:1–26.
- [8] F. Ballarin, A. Manzoni, A. Quarteroni & G. Rozza (2015). “Supremizer stabilization of POD-Galerkin approximation of parametrized steady incompressible Navier-Stokes equations”. *International Journal for Numerical Methods in Engineering*, **102**:1136–1161.
- [9] M. Barrault, Y. Maday, N. Nguyen & A. Patera (2004). “An ‘empirical interpolation’ method: application to efficient reduced-basis discretisation of partial differential equations.”. *Comptes Rendus Mathématique*, **339**:667–672.
- [10] R. Barthelmie & S. Pryor (2014). “Potential contribution of wind energy to climate change mitigation”. *Nature Climate Change*, **4**:684–688.
- [11] Y. Bazilevs & I. Akkerman (2010). “Large eddy simulation of turbulent Taylor–Couette flow using isogeometric analysis and the residual-based variational multiscale method”. *Journal of Computational Physics*, **229**(9):3402–3414.
- [12] Y. Bazilevs, V. Calo, J. Cottrell, T. Hughes, A. Reali & G. Scovazzi (2007). “Variational multi-scale residual-based turbulence modeling for large eddy simulation of incompressible flows”. *Computer Methods in Applied Mechanics and Engineering*, **197**(1-4):173–201.

- [13] Y. Bazilevs, C. Michler, V. Calo & T. Hughes (2007). “Weak Dirichlet boundary conditions for wall-bounded turbulent flows”. *Computer Methods in Applied Mechanics and Engineering*, **196**(49-52):4853–4862.
- [14] M. Behr, D. Hastreiter, S. Mittal & T. Tezduyar (1995). “Incompressible flow past a circular cylinder: dependence of the computed flow field on the location of the lateral boundaries”. *Computer Methods in Applied Mechanics and Engineering*, **123**(1-4):309–316.
- [15] P. Benner, S. Gugercin & K. Willcox (2015). “A survey of projection-based model reduction methods for parametric dynamical systems”. *SIAM Review*, **57**:483–531.
- [16] A. Benveniste & G. Berry (1991). “The synchronous approach to reactive and real-time systems”. *Proceedings of the IEEE*, **79**:1270–1282.
- [17] A. Brooks & T. Hughes (1982). “Streamline upwind/Petrov-Galerkin formulations for convection dominated flows with particular emphasis on the incompressible Navier-Stokes equations”. *Computer Methods in Applied Mechanics and Engineering*, **21**(1):199–259.
- [18] S. Brunton, J. Proctor & N. Kutz (2016). “Discovering governing equations from data by sparse identification of nonlinear dynamical systems”. *Proceedings of the National Academy of Sciences of the United States of America*, **113**:3932–3937.
- [19] S. Buoso, A. Manzoni, H. Alkadhhi & V. Kurtcuoglu (2022). “Stabilized reduced-order models for unsteady incompressible flows in three-dimensional parametrized domains”. *Computers and Fluids*, **246**:105 604.
- [20] S. Cai, Z. Mao, Z. Wang, M. Yin & G. E. Karniadakis (2021). “Physics-informed neural networks (PINNs) for fluid mechanics: a review”. *Acta Mechanica Sinica*, **37**:1–62.
- [21] A. Caiazzo, T. Iliescu, V. John & S. Schyschlowa (2014). “A numerical investigation of velocity-pressure reduced order models for incompressible flows”. *Journal of Computational Physics*, **259**:598–616.
- [22] K. Carlberg, C. Farhat, J. Cortial & D. Amsallem (2013). “The GNAT method for nonlinear model reduction: Effective implementation and application to computational fluid dynamics and turbulent flows”. *Journal of Computational Physics*, **242**:623–647.
- [23] S. Chaturantabut & D. Sorensen (2010). “Nonlinear model reduction via discrete empirical interpolation”. *SIAM Journal on Scientific Computing*, **32**(5):2737–2764.
- [24] H. Childs, E. Brugger, B. Whitlock, J. Meredith, S. Ahern, D. Pugmire, K. Biagas, M. Miller, C. Harrison, G. H. Weber, H. Krishnan, T. Fogal, A. Sanderson, C. Garth, E. W. Bethel, D. Camp, O. Rübel, M. Durant, J. M. Favre & P. Navrátil (2012). *VisIt: An End-User Tool For Visualizing and Analyzing Very Large Data*. Chapman and Hall/CRC. ISBN 9780429105357.
- [25] Y. Choi, W. Arrighi, D. Copeland, R. Anderson & G. Oxberry (2019). “libROM”. [Computer Software] <https://doi.org/10.11578/dc.20190408.3>.
- [26] A. Chorin (1968). “Numerical solution of the Navier-Stokes Equations”. *Mathematics of Computation*, **22**(104):745–762.
- [27] A. Chorin (1997). “A numerical method for solving incompressible viscous flow problems”. *Journal of Computational Physics*, **135**(2):118–125.

- [28] R. Codina (2002). “Stabilized finite element approximation of transient incompressible flows using orthogonal subscales”. *Computer Methods in Applied Mechanics and Engineering*, **191**(39-40):4295–4321.
- [29] R. Codina, R. Reyes & J. Baiges (2021). “A posteriori error estimates in a finite element VMS-based reduced order model for the incompressible Navier-Stokes equations”. *Mechanics Research Communications*, **112**:103–599.
- [30] T. Coffey, C. Kelley & D. Keyes (2003). “Pseudotransient continuation and differential-algebraic equations”. *SIAM Journal on Scientific Computing*, **25**(2):553–569.
- [31] J. Cottrell, T. Hughes & Y. Bazilevs (2009). *Isogeometric analysis: toward integration of CAD and FEA*. John Wiley & Sons. ISBN 9780470748732.
- [32] S. Cuomo, V. Di Cola, F. Giampaolo, G. Rozza, M. Raissi & F. Piccialli (2022). “Scientific Machine Learning Through Physics-Informed Neural Networks: Where we are and What’s Next”. *Journal of Scientific Computing*, **92**:1727–1738.
- [33] D. Didane, M. Behery, M. Al-Ghriyah & B. Manshoor (2024). “Recent Progress in Design and Performance Analysis of Vertical-Axis Wind Turbines—A Comprehensive Review”. *Processes*, **12**:1–33.
- [34] M. Drela (1989). “XFOIL: An analysis and design system for low reynolds number airfoils”. In *L. reynolds number aerodynamics*, ed., *Mueller, Thomas J.*, 1–12. Springer Berlin Heidelberg, Berlin, Heidelberg. ISBN 9783540518846.
- [35] Z. Drmac & S. Gugercin (2016). “A new selection operator for the discrete empirical interpolation method-improved a priori error bound and extensions”. *SIAM Journal on Scientific Computing*, **38**(2):A631–A648.
- [36] Editorial Board (2021). “The rise of data-driven modelling”. *Nature Reviews Physics*, **3**:383.
- [37] M. ten Eikelder & I. Akkerman (2018). “Correct energy evolution of stabilized formulations: The relation between VMS, SUPG and GLS via dynamic orthogonal small-scales and isogeometric analysis. I: The convective-diffusive context”. *Computer Methods in Applied Mechanics and Engineering*, **331**:259–280.
- [38] M. ten Eikelder & I. Akkerman (2018). “Correct energy evolution of stabilized formulations: The relation between VMS, SUPG and GLS via dynamic orthogonal small-scales and isogeometric analysis. II: The incompressible Navier-Stokes equations”. *Computer Methods in Applied Mechanics and Engineering*, **340**:1135–1159.
- [39] M. ten Eikelder & I. Akkerman (2019). “Variation entropy: a continuous local generalization of the TVD property using entropy principles”. *Computer Methods in Applied Mechanics and Engineering*, **355**:261–283.
- [40] M. ten Eikelder, Y. Bazilevs & I. Akkerman (2020). “A theoretical framework for discontinuity capturing: Joining variational multiscale analysis and variation entropy theory”. *Computer Methods in Applied Mechanics and Engineering*, **359**:112–664.
- [41] J. Evans & T. Hughes (2013). “Isogeometric divergence-conforming B-splines for the unsteady Navier-Stokes equations”. *Journal of Computational Physics*, **241**:141–167.

- [42] J. Evans, D. Kamensky & Y. Bazilevs (2020). “Variational multiscale modeling with discretely divergence-free subscales”. *Computers & Mathematics with Applications*, **80**(11):2517–2537.
- [43] R. Everson & L. Sirovich (1995). “Karhunen–Loève procedure for gappy data”. *Journal of the Optical Society of America*, **12**:1657.
- [44] R. Falgout & U. Yang (2002). “hypre: A Library of High Performance Preconditioners”. In P. M. A. Sloot, A. G. Hoekstra, C. J. K. Tan & J. J. Dongarra, eds., *Computational Science — ICCS 2002*, 632–641. Springer Berlin Heidelberg, Berlin, Heidelberg. ISBN 9783540477891.
- [45] C. Farhat, S. Grimberg, A. Manzoni & A. Quarteroni (2021). *Computational bottlenecks for PROMs: precomputation and hyperreduction*, 181–244. De Gruyter, Berlin, Boston. ISBN 9783110671490.
- [46] E. Fonn, H. van Brummelen, T. Kvamsdal & A. Rasheed (2019). “Fast divergence-conforming reduced basis methods for steady Navier–Stokes flow”. *Computer Methods in Applied Mechanics and Engineering*, **346**:486–512.
- [47] I. Fried (1969). “Finite-element analysis of time-dependent phenomena”. *AIAA Journal*, **7**(6):1170–1173.
- [48] P. German, M. Tano, J. Ragusa & C. Fiorina (2020). “Comparison of Reduced-Basis techniques for the model order reduction of parametric incompressible fluid flows”. *Progress in Nuclear Energy*, **130**:103 551.
- [49] C. Giannelli, B. Jüttler, S. Kleiss, A. Mantzaflaris, B. Simeon & J. Špeh (2016). “THB-splines: An effective mathematical technology for adaptive refinement in geometric design and isogeometric analysis”. *Computer Methods in Applied Mechanics and Engineering*, **299**:337–365.
- [50] C. Giannelli, B. Jüttler & H. Speleers (2012). “THB-splines: The truncated basis for hierarchical splines”. *Computer Aided Geometric Design*, **29**(7):485–498.
- [51] A. Gopinath & A. Jameson (2005). “Time spectral method for periodic unsteady computations over two- and three- dimensional bodies”. In *43rd AIAA Aerospace Sciences Meeting and Exhibit - Meeting Papers*, 10 683–10 696. American Institute of Aeronautics and Astronautics Inc. ISBN 9781624100642.
- [52] S. Grimberg, C. Farhat & N. Youkilis (2020). “On the stability of projection-based model order reduction for convection-dominated laminar and turbulent flows”. *Journal of Computational Physics*, **419**:109 681.
- [53] V. Gupta & S. Bhatu (1991). “Solution of cyclic profiles in catalytic reactor operation with periodic flow reversal”. *Computers in Chemical Engineering*, **15**:229–237.
- [54] K. Hall, J. Thomas & W. Clark (2002). “Computation of unsteady nonlinear flows in cascades using a harmonic balance technique”. *AIAA Journal*, **40**:879–886.
- [55] S. Hijazi, G. Stabile, A. Mola & G. Rozza (2020). “Data-driven POD–Galerkin reduced order model for turbulent flows”. *Journal of Computational Physics*, **416**:109 513.
- [56] M. Hsu, D. Kamensky, F. Xu, J. Kiendl, C. Wang, M. Wu, J. Mineroff, A. Reali, Y. Bazilevs & M. Sacks (2015). “Dynamic and fluid–structure interaction simulations of bioprosthetic heart valves using parametric design with T-splines and Fung-type material models”. *Computational Mechanics*, **55**:1211–1225.

- [57] T. Hughes (1995). “Multiscale phenomena: Green’s functions, the Dirichlet-to-Neumann formulation, subgrid scale models, bubbles and the origins of stabilized methods”. *Computer Methods in Applied Mechanics and Engineering*, **127**(1-4):387–401.
- [58] T. Hughes, J. Cottrell & Y. Bazilevs (2005). “Isogeometric analysis: CAD, finite elements, NURBS, exact geometry and mesh refinement”. *Computer Methods in Applied Mechanics and Engineering*, **194**(39-41):4135–4195.
- [59] T. Hughes, G. Engel, L. Mazzei & M. Larson (2000). “The continuous Galerkin method is locally conservative”. *Journal of Computational Physics*, **163**(2):467–488.
- [60] T. Hughes, G. Feijóo, L. Mazzei & J. Quincy (1998). “The variational multiscale method—a paradigm for computational mechanics”. *Computer Methods in Applied Mechanics and Engineering*, **166**(1-2):3–24.
- [61] T. Hughes, L. Franca & M. Balestra (1986). “A new finite element formulation for computational fluid dynamics: V. Circumventing the babuška-brezzi condition: a stable Petrov-Galerkin formulation of the stokes problem accommodating equal-order interpolations”. *Computer Methods in Applied Mechanics and Engineering*, **59**(1):85–99.
- [62] T. Hughes, L. Franca & G. Hulbert (1989). “A new finite element formulation for computational fluid dynamics: VIII. The Galerkin/least-squares method for advective-diffusive equations”. *Computer Methods in Applied Mechanics and Engineering*, **73**(2):173–189.
- [63] T. Hughes & J. Stewart (1996). “A space-time formulation for multiscale phenomena”. *Journal of Computational and Applied Mathematics*, **74**(1-2):217–229.
- [64] T. Iliescu & Z. Wang (2014). “Variational multiscale proper orthogonal decomposition: Navier-stokes equations”. *Numerical Methods for Partial Differential Equations*, **30**:641–663.
- [65] A. Ivagnes, G. Stabile, A. Mola, T. Iliescu & G. Rozza (2023). “Pressure data-driven variational multiscale reduced order models”. *Journal of Computational Physics*, **476**:111 904.
- [66] L. Jiang, L. T. Biegler & V. G. Fox (2003). “Simulation and optimization of pressure-swing adsorption systems for air separation”. *AIChE Journal*, **49**:1140–1157.
- [67] A. Johnson & T. Tezduyar (1994). “Mesh update strategies in parallel finite element computations of flow problems with moving boundaries and interfaces”. *Computer methods in applied mechanics and engineering*, **119**:73–94.
- [68] M. Jordan & T. Mitchell (2015). “Machine learning: Trends, perspectives, and prospects”. *Science*, **349**:255–260.
- [69] D. Kamensky, M. Hsu, D. Schillinger, J. Evans, A. Aggarwal, Y. Bazilevs, M. Sacks & T. Hughes (2015). “An immersogeometric variational framework for fluid-structure interaction: Application to bioprosthetic heart valves”. *Computer Methods in Applied Mechanics and Engineering*, **284**:1005–1053.
- [70] C. Kelley & D. Keyes (1998). “Convergence analysis of pseudo-transient continuation”. *SIAM Journal on Numerical Analysis*, **35**(2):508–523.
- [71] M. Khalid & I. Akhtar (2012). “Characteristics of flow past a symmetric airfoil at low Reynolds number: a nonlinear perspective”. In *Proceedings of IMECE2012*, 167–175.

- [72] Y. Kim, Y. Choi, D. Widemann & T. Zohdi (2022). “A fast and accurate physics-informed neural network reduced order model with shallow masked autoencoder”. *Journal of Computational Physics*, **451**:110–118.
- [73] T. Kinsey & G. Dumas (2008). “Parametric study of an oscillating airfoil in a power-extraction regime”. *AIAA Journal*, **46**(6):1318–1330.
- [74] B. Kramer, B. Peherstorfer & K. Willcox (2024). “Learning Nonlinear Reduced Models from Data with Operator Inference”. *Annual Review of Fluid Mechanics*, **56**(Volume 56, 2024):521–548.
- [75] A. Krishnapriyan, A. Gholami, S. Zhe, R. Kirby & M. W. Mahoney (2021). “Characterizing possible failure modes in physics-informed neural networks”. In *35th Conference on Neural Information Processing Systems (NeurIPS 2021)*. ISBN 9781713845393.
- [76] T. Kuraishi, K. Takizawa & T. Tezduyar (2019). “Space-time isogeometric flow analysis with built-in Reynolds-equation limit”. *Mathematical Models and Methods in Applied Sciences*, **29**:871–904.
- [77] D. Kurtulus (2015). “On the unsteady behavior of the flow around NACA 0012 airfoil with steady external conditions at $Re=1000$ ”. *International Journal of Micro Air Vehicles*, **7**(3):301–326.
- [78] T. Kvamsdal & K. Okstad (1998). “Error estimator for variational consistent surface forces in Navier-Stokes simulations”. In *Proceedings for Computational Mechanics, New trends and applications, CIMNE, Barcelona, Spain*, 1–11. ISBN 9788489925151.
- [79] A. Laghari, H. Shah, R. Laghari, K. Kumar, A. Waqan & A. Jumani (2018). “A Review on Quantum Computing Trends & Future Perspectives”. *EAI Endorsed Transactions on Cloud Systems*, 173979.
- [80] P. Langley (1981). “Data-Driven Discovery of Physical Laws”. *Cognitive Science*, **5**:31–54.
- [81] J. Lauzon, S. Cheung, Y. Shin, Y. Choi, D. Copeland & K. Huynh (2024). “S-OPT: A Points Selection Algorithm for Hyper-Reduction in Reduced Order Models”. *SIAM Journal on Scientific Computing*, **46**:B474–B501.
- [82] S. Le Fouest & K. Mulleners (2022). “The dynamic stall dilemma for vertical-axis wind turbines”. *Renewable Energy*, **198**:505–520.
- [83] S. Le Fouest & K. Mulleners (2024). “Optimal blade pitch control for enhanced vertical-axis wind turbine performance”. *Nature Communications*, **15**:1–13.
- [84] K. Lee & K. Carlberg (2020). “Model reduction of dynamical systems on nonlinear manifolds using deep convolutional autoencoders”. *Journal of Computational Physics*, **404**:108–118.
- [85] Linkin Park (2024). “From Zero”. *Warner Records Inc. & Machine Shop Records Vinyl*.
- [86] Y. Liu, K. Li, J. Zhang, H. Wang & L. Liu (2012). “Numerical bifurcation analysis of static stall of airfoil and dynamic stall under unsteady perturbation”. *Communications in Nonlinear Science and Numerical Simulation*, **17**(8):3427–3434.
- [87] S. Lorenzi, A. Cammi, L. Luzzi & G. Rozza (2016). “POD-Galerkin method for finite volume approximation of Navier–Stokes and RANS equations”. *Computer Methods in Applied Mechanics and Engineering*, **311**:151–179.

- [88] J. Lotz, M. ten Eikelder & I. Akkerman (2024). “Space–time computations of exactly time-periodic flows past hydrofoils”. *Computers & Fluids*, **277**:106 286.
- [89] J. Lotz, G. Weymouth & I. Akkerman (2024). “Projection-based reduced-order modelling of time-periodic problems, with application to flow past flapping hydrofoils”. *Computer Methods in Applied Mechanics and Engineering*, **429**:117 161.
- [90] J. Lumley (1967). “The structure of inhomogeneous turbulent flows”. *Atmospheric Turbulence and Radio Wave Propagation*.
- [91] A. Løvgren, Y. & E. Rønquist (2006). “A reduced basis element method for the steady stokes problem”. *Mathematical Modelling and Numerical Analysis*, **40**:529–552.
- [92] V. Marx (2013). “The big challenges of big data”. *Nature*, **498**:255–260.
- [93] A. Masud & T. Hughes (1997). “A space-time Galerkin/least-squares finite element formulation of the Navier-Stokes equations for moving domain problems”. *Computer Methods in Applied Mechanics and Engineering*, **146**(1-2):91–126.
- [94] H. Melbø & T. Kvamsdal (2002). “Goal oriented error estimators for Stokes equations based on variationally consistent postprocessing”. *Computer methods in applied mechanics and engineering*, **192**:613–633.
- [95] G. Mendonça, F. Afonso & F. Lau (2019). “Model order reduction in aerodynamics: Review and applications”. *Proceedings of the Institution of Mechanical Engineers, Part G: Journal of Aerospace Engineering*, **233**:5816–5836.
- [96] V. Michelassi, J. G. Wissink & W. Rodi (2003). “Direct numerical simulation, large eddy simulation and unsteady Reynolds-averaged Navier-Stokes simulations of periodic unsteady flow in a low-pressure turbine cascade: A comparison”. *Proceedings of the Institution of Mechanical Engineers, Part A: Journal of Power and Energy*, **217**(4):403–412.
- [97] S. Mittal & T. Tezduyar (1992). “A finite element study of incompressible flows past oscillating cylinders and aerofoils”. *International Journal for Numerical Methods in Fluids*, **15**:1073–1118.
- [98] S. Mittal & T. Tezduyar (1992). “Notes on the stabilized space-time finite-element formulation of unsteady incompressible flows”. *Computer Physics Communications*, **73**(1-3):93–112.
- [99] S. Mittal & T. Tezduyar (1994). “Massively parallel finite element computation incompressible flows involving fluid-body interactions”. *Computer Methods in Applied Mechanics and Engineering*, **112**:253–282.
- [100] M. Montardini, M. Negri, G. Sangalli & M. Tani (2020). “Space–time least–squares isogeometric method and efficient solver for parabolic problems”. *Mathematics of Computation*, **89**(323):1193–1227.
- [101] C. Mou, B. Koc, O. San, L. G. Rebholz & T. Iliescu (2021). “Data-driven variational multiscale reduced order models”. *Computer Methods in Applied Mechanics and Engineering*, **373**:113 470.
- [102] N. Nguyen & J. Peraire (2008). “An efficient reduced-order modeling approach for non-linear parametrized partial differential equations”. *International Journal for Numerical Methods in Engineering*, **76**:27–55.

- [103] B. Noack, P. Papas & P. Monkewitz (2005). “The need for a pressure-term representation in empirical Galerkin models of incompressible shear flows”. *Journal of Fluid Mechanics*, **523**:339–365.
- [104] J. Oden (1969). “A general theory of finite elements. I. Topological considerations”. *International Journal for Numerical Methods in Engineering*, **1**(2):205–221.
- [105] J. Oden (1969). “A general theory of finite elements. II. Applications”. *International Journal for Numerical Methods in Engineering*, **1**(3):247–259.
- [106] Y. Otoguro, K. Takizawa & T. Tezduyar (2017). “Space–time VMS computational flow analysis with isogeometric discretization and a general-purpose NURBS mesh generation method”. *Computers and Fluids*, **158**:189–200.
- [107] H. Paudel, M. Syamlal, S. Crawford, Y.-L. Lee, R. Shugayev, P. Lu, P. Ohodnicki, D. Molloy & Y. Duan (2022). “Quantum Computing and Simulations for Energy Applications: Review and Perspective”. *ACS Engineering Au*, **2**:151–196.
- [108] B. Peherstorfer, K. Willcox & M. Gunzburger (2018). “Survey of multifidelity methods in uncertainty propagation, inference, and optimization”. *SIAM Review*, **60**:550–591.
- [109] F. Platte, D. Kuzmin, C. Fredebeul & S. Turek (2005). “Novel simulation approaches for cyclic steady-state fixed-bed processes exhibiting sharp fronts and shocks”. In D. H. Mache, J. Szabados & M. G. de Bruin, eds., *Trends and Applications in Constructive Approximation*, 207–223. Birkhäuser Basel. ISBN 9783764373566.
- [110] F. Porté-Agel, M. Bastankhah & S. Shamsoddin (2020). “Wind-Turbine and Wind-Farm Flows: A Review”. *Boundary-Layer Meteorology*, **174**:1–59.
- [111] A. Quarteroni, A. Manzoni & F. Negri (2015). *Reduced Basis Methods for Partial Differential Equations: An Introduction*. Springer International Publishing. ISBN 9783319154312.
- [112] M. Raissi (2018). “Deep Hidden Physics Models: Deep Learning of Nonlinear Partial Differential Equations”. *Journal of Machine Learning Research*, **19**:1–24.
- [113] M. Raissi, P. Perdikaris & G. Karniadakis (2019). “Physics-informed neural networks: A deep learning framework for solving forward and inverse problems involving nonlinear partial differential equations”. *Journal of Computational Physics*, **378**:686–707.
- [114] T. Rebollo, E. Ávila, M. Marmol, F. Ballarin & G. Rozza (2017). “On a certified smagorinsky reduced basis turbulence model”. *SIAM Journal on Numerical Analysis*, **55**:3047–3067.
- [115] R. Reyes & R. Codina (2020). “Projection-based reduced order models for flow problems: A variational multiscale approach”. *Computer Methods in Applied Mechanics and Engineering*, **363**:112 844.
- [116] O. Reynolds (1895). “On the dynamical theory of incompressible viscous fluids and the determination of the criterion”. *Philosophical Transactions of the Royal Society of London*, **186**:123–164.
- [117] T. Richter (2021). “An averaging scheme for the efficient approximation of time-periodic flow problems”. *Computers and Fluids*, **214**.

- [118] F. Romor, G. Stabile & G. Rozza (2023). “Non-linear Manifold Reduced-Order Models with Convolutional Autoencoders and Reduced Over-Collocation Method”. *Journal of Scientific Computing*, **94**:1–39.
- [119] D. Roose, K. Lust, A. Champneys & A. Spence (1995). “A Newton-Picard shooting method for Computing periodic solutions of large-scale dynamical systems”. *Chaos, Solitons & Fractals*, **5**:1913–1925.
- [120] G. Rozza, D. Phuong Huynh & A. Manzoni (2013). “Reduced basis approximation and a posteriori error estimation for Stokes flows in parametrized geometries: Roles of the inf-sup stability constants”. *Numerische Mathematik*, **125**:115–152.
- [121] C. Saadé, S. Lejeunes, D. Eyheramendy & R. Saad (2021). “Space-time isogeometric analysis for linear and non-linear elastodynamics”. *Computers and Structures*, **254**:106 594.
- [122] S. Sachar, P. Doerffer, P. Flaszynski, J. Kotus, K. Doerffer & J. Grzelak (2023). “Correlation Between the Generated Noise and Effectiveness for a Vertical Axis Savonius Type Rotor”. In *AIAA SciTech Forum and Exposition, 2023*. American Institute of Aeronautics and Astronautics Inc, AIAA. ISBN 9781624106996.
- [123] A. Salinger & G. Eigenberger (1996). “The direct calculation of period states of the reversible flow reactor - I. Methodology and propane combustion results”. *Chemical Engineering Science*, **51**:4903–4913.
- [124] O. San, S. Pawar & A. Rasheed (2022). “Variational multiscale reinforcement learning for discovering reduced order closure models of nonlinear spatiotemporal transport systems”. *Scientific Reports*, **12**:1–12.
- [125] F. Shakib & T. Hughes (1991). “A new finite element formulation for computational fluid dynamics: IX. Fourier analysis of space-time Galerkin/least-squares algorithms”. *Computer Methods in Applied Mechanics and Engineering*, **87**(1):35–58.
- [126] J. Smagorinsky (1963). “General circulation experiments with the primitive equations, 1: The basic experiment”. *Monthly Weather Review*, **91**:99–164.
- [127] G. Stabile, F. Ballarin, G. Zuccarino & G. Rozza (2019). “A reduced order variational multiscale approach for turbulent flows”. *Advances in Computational Mathematics*, **45**:2349–2368.
- [128] G. Stabile & G. Rozza (2018). “Finite volume POD-Galerkin stabilised reduced order methods for the parametrised incompressible Navier–Stokes equations”. *Computers and Fluids*, **173**:273–284.
- [129] S. Stoter, M. ten Eikelder, F. de Prenter, I. Akkerman, E. van Brummelen, C. Verhoosel & D. Schillinger (2021). “Nitsche’s method as a variational multiscale formulation and a resulting boundary layer fine-scale model”. *Computer Methods in Applied Mechanics and Engineering*, **382**:113 878.
- [130] K. Takizawa, B. Henicke, A. Puntel, T. Spielman & T. Tezduyar (2012). “Space-time computational techniques for the aerodynamics of flapping wings”. *Journal of Applied Mechanics*, **79**:1–10.
- [131] K. Takizawa & T. Tezduyar (2011). “Multiscale space-time fluid-structure interaction techniques”. *Computational Mechanics*, **48**(3):247–267.

- [132] K. Takizawa & T. Tezduyar (2012). “Space-time fluid-structure interaction methods”. *Mathematical Models and Methods in Applied Sciences*, **22**:1–49.
- [133] K. Takizawa & T. Tezduyar (2014). “Space-time computation techniques with continuous representation in time (ST-C)”. *Computational Mechanics*, **53**(1):91–99.
- [134] A. Tello, R. Codina & J. Baiges (2020). “Fluid structure interaction by means of variational multiscale reduced order models”. *International Journal for Numerical Methods in Engineering*, **121**:2601–2625.
- [135] R. Témam (1969). “Sur l’approximation de la solution des équations de Navier-Stokes par la méthode des pas fractionnaires (I)”. *Archive for Rational Mechanics and Analysis*, **32**(2):135–153.
- [136] T. Tezduyar, S. Aliabadi, M. Behr, A. Johnson & S. Mittal (1993). “Parallel finite-element computation of 3D flows”. *Computer*, **26**:27–36.
- [137] T. Tezduyar, S. Aliabadi, M. Behr & S. Mittal (1994). “Massively parallel finite element simulation of compressible and incompressible flows”. *Computer Methods in Applied Mechanics and Engineering*, **119**:157–177.
- [138] T. Tezduyar, M. Behr & J. Liou (1992). “A new strategy for finite element computations involving moving boundaries and interfaces-The deforming-spatial-domain / space-time procedure: I. The concept and the preliminary numerical tests”. *Computer Methods in Applied Mechanics and Engineering*, **94**:339–351.
- [139] T. Tezduyar, M. Behr, S. Mittal & J. Liou (1992). “A new strategy for finite element computations involving moving boundaries and interfaces-The deforming-spatial-domain / space-time procedure: II, Computation of free-surface flows, two-liquid flows, and flows with drifting cylinders”. *Computer Methods in Applied Mechanics and Engineering*, **94**:353–371.
- [140] T. Tezduyar, S. Mittal, S. Ray & R. Shih (1992). “Incompressible flow computations with stabilized bilinear and linear equal-order-interpolation velocity-pressure elements”. *Computer Methods in Applied Mechanics and Engineering*, **95**:221–242.
- [141] T. Tezduyar & K. Takizawa (2019). “Space-time computations in practical engineering applications: a summary of the 25-year history”. *Computational Mechanics*, **63**(4):747–753.
- [142] T. Theodorsen (1949). “General Theory of Aerodynamic Instability and the Mechanism of Flutter”. *Tech. rep.*, Langley Memorial Aeronautical Laboratory.
- [143] Z. Wang, I. Akhtar, J. Borggaard & T. Iliescu (2012). “Proper orthogonal decomposition closure models for turbulent flows: A numerical comparison”. *Computer Methods in Applied Mechanics and Engineering*, **237-240**:10–26.
- [144] D. Wolpert & W. Macready (1997). “No Free Lunch Theorems for Optimization”. *IEEE Transactions on Evolutionary Computation*, **1**:67.
- [145] X. Xie, C. Webster & T. Iliescu (2020). “Closure learning for nonlinear model reduction using deep residual neural network”. *Fluids*, **5**.
- [146] M. Yano & A. Patera (2019). “An LP empirical quadrature procedure for reduced basis treatment of parametrized nonlinear PDEs”. *Computer Methods in Applied Mechanics and Engineering*, **344**:1104–1123.

-
- [147] J. Yu, C. Yan & M. Guo (2019). “Non-intrusive reduced-order modeling for fluid problems: A brief review”. *Proceedings of the Institution of Mechanical Engineers, Part G: Journal of Aerospace Engineering*, **233**:5896–5912.

